IJBBE International Journal of Biophotonics & Biomedical Engineering Vol. 4, No. 2, Fall - Winter, 2024

Research Article

# Characterization of the Breast Cancer Cell Lines Using Fluorescence Spectroscopy

**N. Taheri [a], M. ghezelbash [b], R. ramezani [c] and B. sajad [a]**

*a Department of Atomic and Molecular Physics, Faculty of Physics, Alzahra University, Tehran, Iran*
*b Department of Electronics, Faculty of Electrical and Computer Engineering, Malek Ashtar University of Technology*
*c Department of Family Therapy, Women Research Center, Alzahra University, Tehran, Iran*

***Corresponding Author Email: bsajad@alzahra.ac.ir**

**DOI:10.71498/ijbbe.2024.1190511**

**ABSTRACT**

Received: Nov. 17, 2024, Revised: Dec. 27, 2024, Accepted: Dec. 29, 2024, Available Online: Feb. 17, 2025

*Breast cancer is a widespread disease that affects individuals worldwide. The challenges lie in achieving timely diagnosis, accuracy, sensitivity, and reliable results from traditional diagnostic methods. Additionally, delayed diagnosis often leads to the metastasis of cancerous cells to the axillary lymph nodes, complicating treatment and frequently necessitating complete organ removal. Despite its limitations, fluorescence spectroscopy offers practical and applicable solutions. The Laser-Induced Fluorescence Spectroscopy (LIFS) technique is noteworthy for its high accuracy, sensitivity, and rapid capabilities in characterizing and detecting various cancerous areas and cultured cell samples.*
*Moreover, it boasts a low risk, cost-effectiveness, and minimal side effects. This research aims to analyze the various cancer cell lines (e.g., MCF10 cells), highlighting their distinct biological differences compared to human breast cells (MCF10 cells), referred to as the control. Due to the high accuracy and sensitivity of the proposed solution, this diagnostic tool can enhance breast cancer detection. The technique is ready for pre/post-clinical use as a non-invasive diagnostic tool, offering significant benefits in early diagnosis and patient evaluation before invasive procedures. Metabolic alterations in cancer cell lines result in substantial differences in the concentrations of key fluorophores, such as NADH and Flavins, compared to normal cells. Variations in fluorescence emission provide a foundation for the characterization and diagnosis of breast cancer through a fluorescence-guided approach. Cancer cells show intense spectral peaks, while normal cells have a continuous fluorescence range. These differences can aid in diagnostic applications, particularly in fluorescence spectroscopy.*

**KEYWORD**

*Fluorescence, Spectroscopy, Breast Cancer, Diagnosis, Fluorophores*

## I. INTRODUCTION

For breast cancer (BC) diagnosis, the main challenge is identifying critical factors for accurate and timely detection. High accuracy and sensitivity in early diagnosis are crucial, as they markedly diminish the risk of metastasis and the necessity for radical treatments. Consequently, this approach safeguards the patient's quality of life and averts the loss of body organs [1-3].

Traditional breast cancer diagnostic methods, such as X-ray mammography, MRI, and PET/CT, are widely used due to their ability to provide detailed anatomical images [4]. However, these techniques have notable limitations. While relatively cost-effective, X-ray mammography often lacks sensitivity and specificity, particularly in dense breast tissues. MRI provides high-resolution images but is expensive and time-consuming. PET/CT, although sensitive, involves high operational costs and exposure to ionizing radiation.

Laser-Induced Fluorescence Spectroscopy (LIFS) offers a non-invasive, cost-effective alternative with superior sensitivity and specificity [2, 4]. LIFS can detect biochemical changes at the cellular level, providing real-time results without expensive infrastructure or exposure to harmful radiation. Therefore, fluorescence spectroscopy can be a highly advantageous method for early and accurate breast cancer diagnosis, especially in resource-limited settings [4, 5].

In Laser-induced fluorescence spectroscopy (LIFS), the cell lines excite with a laser to emit fluorescence. The radiated light is then analyzed to detect biochemical changes at the cellular level. LIFS is particularly effective for detecting breast cancer at an early stage, as it can detect metabolic changes in vitro using cell lines [5-7].

Our previous study hypothesized that fluorescence-based approaches concerning photodynamic assessments hold significant potential for accurate discrimination and characterization of cancerous and normal breast cells. Using 5-aminolevulinic acid (5-ALA) as a probe to characterize biomarkers metabolic changes and provide valuable insights into functional and morphological alterations associated with breast cancer progression [2]. This study employs a dual approach by utilizing normal human (MCF10) and cancerous (MCF-7) breast cell lines under controlled laboratory conditions to enhance breast cancer diagnostic accuracy based on auto-fluorescence. This methodology facilitates a comprehensive analysis of cellular behaviors and responses, advancing breast cancer diagnostics [8, 9].

## II. Materials and Methods

### A. *Cell Lines*

The MCF-7 cell line was established in 1973 at the Michigan Cancer Foundation (the Barbara Ann Karmanos Cancer Institute). It was derived from the pleural effusion of a woman with metastatic breast cancer, a valuable model for studying hormone-responsive breast cancers [10]. The MCF10 cell line series was first described in 1990 by Soule and colleagues [10]. These cell lines were derived from normal human mammary epithelial cells obtained from a woman with fibrocystic breast disease. The MCF10 cell lines are precious for their ability to form three-dimensional structures that resemble normal breast tissue, making them an excellent model for studying breast cancer development and progression [10].

In the sample preparation phase, various cell densities were cultured in 1.5 mL of phosphate-buffered saline (PBS) under 5% CO2, 37°C, and 95% humidity. This approach facilitated the examination of different cell concentrations [11]. PBS was selected as the medium to avoid potential fluorescence interference from standard cell culture media and bovine serum, thereby minimizing background fluorescence and enhancing the accuracy of fluorescence spectroscopy measurements.

### B. *Experimental Setup*

Fig. 1 shows the schematic optical array for cell line fluorescence characterizations. It employed a diode laser (CNI, PSU III LED) with a power density of 65 W/cm² over an area of less than 0.11 mm². It operated at a fixed wavelength of 405 nm. This laser was configured to excite key fluorophores within the cells (such as NADH, Flavin, etc.). This approach could lead to the development of an efficient and user-friendly system for discriminating samples based on their spectral features.

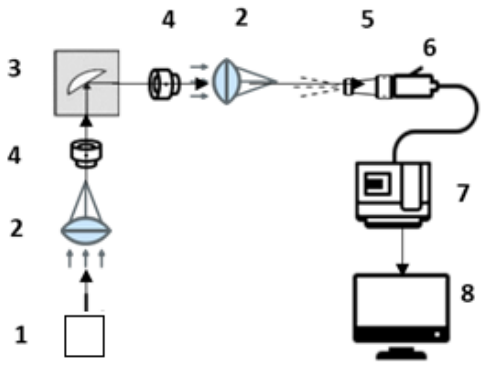


Fig. **1.** Schematic setup for cell lines fluorescence characterizations: (1) laser, (2) optical elements (lens, polarizer), (3) cell lines, (4) optical Objectives, (5) collective spectrophotometer, etc., (6) optical fiber cable, (7) spectrophotometer, (8) monitor.

This setup offers high efficiency and a longer lifetime than traditional lamp sources, with the laser capable of generating an output power ranging from 1 to 200 mW.

Despite the superior quality and stability of the laser beam, a set of filters, including two bandpass filters and lenses with 50 mm focal lengths, were used to direct the collimated beam to the center of the quartz cuvette at the center of the holder. The optical cable used for the UVS-2500 spectrometer is equipped with 905 SMA fiber connectors, facilitating connectivity with other equipment. The optical array also utilizes a lens with a 50 mm focal length.

We employed the UVS-250 miniature optical spectrometer from Poishtadikarane Fiztech (https://phystec.ir/en/), operating within the 190-850 nm spectral range, to detect fluorescence radiation from cell lines. This spectrometer features a 3648-pixel detector and employs visible and ultraviolet light sources. The device is compatible with optical fiber probes, enabling it to be used in various applications such as absorption, transmission, radiation, reflection, fluorescence, and phosphorescence measurements. The integrated diffraction grating enhances the clarity of the target spectrum.

Each experiment determining the optimal cell count was rigorously conducted twenty times to ensure the accuracy and reliability of our findings. Initial trials commenced with 50,000 cells, progressing to 500,000, 520,000, 1,055,000, 2,110,000, and 4,220,000 cells for the healthy cell line. We cultured 50,000 and 500,000 cells for cancer cells using the cell culture method and subsequently analyzed both types via non-invasive fluorescence induction.

## III. Discussion

### A. *key fluorophore*

In medical diagnostics, the measurement of quantum yield, polarization, and excited state lifetime is of considerable value. Quantum yield is a key parameter, defined as the ratio of photons emitted by a fluorophore to those absorbed. Polarization measurements provide insights into the dynamics of fluorophores, particularly their movement during the excited state lifetime, which is the period between light absorption and emission [4, 5].

Breast cells' intrinsic fluorescence emission spectrum spans the characteristic range of 400-800 nm [12, 13].

Cells contain molecules that fluoresce under specific UV/Vis wavelengths. This intrinsic fluorescence, from endogenous fluorophores, differs from signals from external markers. Cellular auto-fluorescence mainly comes from mitochondria and lysosomes. Key endogenous fluorophores include aromatic amino acids, lipopigments, pyridinic coenzymes (NADPH), and flavins. In cell lines, the extracellular matrix, especially collagen and elastin, often contributes more to autofluorescence due to their high quantum yields [2].

Physiological and pathological processes induce changes in the quantity and distribution of endogenous fluorophores and alter the chemical-physical properties of their microenvironment. Consequently, analytical techniques leveraging intrinsic fluorescence can provide valuable insights into cells' and Cellular morphological and physiological states. This technique offers real-time analysis without the need for sample fixation or staining. Recent advancements in spectroscopic and imaging methods have expanded their

applications in basic research and clinical diagnostics [14].

The metabolic alterations in cancerous cells result in distinct concentrations of key fluorophores compared to healthy tissues. This variation in fluorescence emission forms the foundation for characterizing and diagnosing breast cancer masses through fluorescence-guided strategies [15].

## IV. RESULTS

### A. *Characterization of Cell lines*

#### *Characterization of Fluorescence Emission Spectrum in Healthy Breast Cells (MCF10)*

Multiple normal and cancerous breast cell samples were cultured in the biomedical laboratory at Alzahra University. The fluorescence emission spectra of these cell lines were analyzed using laser-induced fluorescence spectroscopy (LIFS) in the photonics laboratory. The obtained data showed a high degree of consistency with previous findings. This experiment was conducted twenty times over six months on different days. Fig. 2 illustrates normal breast cells' fluorescence emission intensity versus wavelength (nm). The spectrum, spanning approximately 420 nm to 700 nm, exhibits prominent peaks at 429 nm, 470 nm, 595 nm, 624 nm, 632 nm, and 674 nm, indicating significant fluorescence emission at these wavelengths [12, 13].

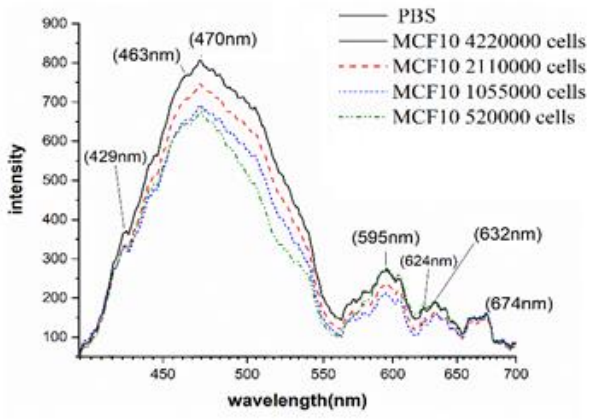


Fig. **2**. Fluorescence emission spectrum of normal human breast cells

As can be seen, the fluorescence spectrum of the phosphate-buffered saline (PBS) used as a cell substrate exhibited no emission. The experiment was conducted under optimal configuration, with specific exposure times (450 and 500 ms). Notably, the optimal cell line concentration was determined before characterization. All samples were diluted in 1 ml of PBS. The primary fluorescence emission range, from 410 to 700 nm, was observed with significant intensity without markers [12, 13].

The well-known intrinsic cellular fluorescence emission range spans from 410 to 540 nm (covering flavins, NADH, NADPH, and elastin) and from 570 to 700 nm (covering vitamins and lipids). Within these ranges, prominent fluorophores have been observed. Specifically, at 463 nm, Ceroid, a member of the lipid family, is detected. A distinct peak at 470 nm corresponds to NADPH, while at 595 nm, a type of lipid known as Phospholipid is observed. A different kind of this lipid is also seen at 540 nm [2, 5, 13].

### B. *Characterization of Fluorescence Emission Spectrum in Normal Breast Cells (MCF7)*

Fig. 3 presents the fluorescence emission spectrum of breast cancer cells, spanning from 450 to 700 nm. Notably, there is a significant decrease in intensity within the interval typically associated with normal breast cells [16].

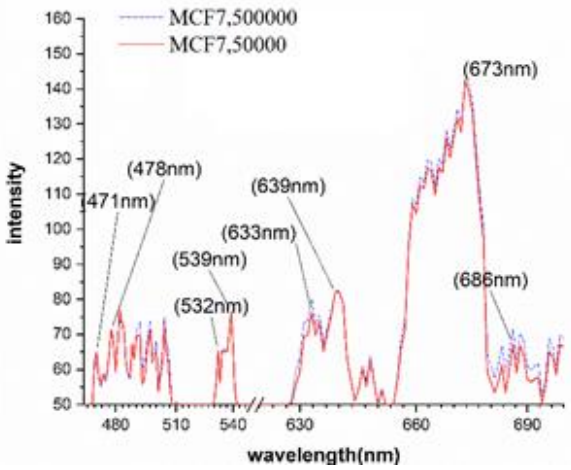


Fig. **3.** The intrinsic fluorescence emission spectrum of MCF7 cancer cells

The optimal cell numbers were identified after conducting multiple experiments with cell counts of 50,000 and 500,000. The optimal counts were determined to be 50,000 and 500,000, with these two samples serving as reference points for comparison and detailed analysis. As observed in the above spectrum, the spectral range of the cancerous cell line, between 600 to 700 nm, exhibits higher intensity. In contrast, the range of 450 nm to 580 nm, which corresponds to the spectral range of normal breast cells, shows significantly weaker fluorescence.

Additionally, the 630 to 700 nm range, near the IR region and characteristic of the breast cancer cell line, displays evident changes in porphyrin metabolism [12, 16].

The most prominent distinction in the spectral characterization of cancerous versus healthy cells is the emergence of sharp, intense peaks. Each lipid and protein is distinctly separated, highlighting a significant deviation in cellular composition.

The comparison of fluorescence emission spectra between normal (MCF10) and cancerous (MCF7) breast cell lines provides valuable insights into the changes in fluorophores. The fluorescence emission of normal cells begins at a wavelength of 410 nm, whereas for cancerous cells, it starts at 465 nm. The primary fluorescence range of healthy cells is more intense and continuous, in contrast to the more compressed and discrete spectrum observed in cancerous cells.

## V. Conclusion

The characteristic wavelength range for healthy cells spans from 410 nm to 550 nm, with a secondary range from 570 nm to 700 nm. The continuous spectrum from 400 nm to 700 nm, which includes numerous fluorophores, behaves smoothly in healthy cells. The key segment of this spectrum, from 420 nm to 550 nm, exhibits high fluorescence intensity in healthy cells. The well-known intrinsic fluorescence emission range of cells extends from 420 nm to 540 nm (covering flavins, NADH, NADPH, and elastin) and from 570 nm to 700 nm (covering vitamins and lipids), where notable fluorophores are observed.

At the 425 nm peak, pyridoxic acid from the vitamin B complex group is detected, which shifts to 471 nm in cancerous cells, indicating a wavelength shift of approximately 50 nm. In healthy cells, clear peaks are observed at 470 nm for NADPH, 595 nm for a type of lipid known as Phospholipid, and 540 nm for another kind of the same lipid. These peaks exhibit significantly lower intensity in cancerous cells, with a wavelength shift of 21 nm.

## References

**[1]** Institute, N.C., cancer.gov, National Cancer Institute, http://www.cancer.gov/publications/ /patient/patient-education/understanding-breast-changes, 2024.

**[2]** M. Ghezelbash, B. Sajad, and S. Hojatizadeh, "Fluorescence-Enhanced Assessments for Human Breast Cancer Cell Characterizations," Photonics, vol.11, pp. 746, 2024.

**[3]** WHO, https://www.cancer.gov/about-cancer/understanding/what-is-cancer. 2024.

**[4]** He Z. et al. "A review on methods for diagnosis of breast cancer cells and tissues," Cell Prolif, vol. 53, pp. e12822, 2020.

**[5]** Dramićanin T. and M.D. Dramićanin. *Using Fluorescence Spectroscopy to Diagnose Breast Cancer*. 2016.

**[6]** Bernard Valeur M.N.B.-S. *Molecular Fluorescence: Principles and Applications*, 2nd Edition. 2012.

**[7]** Adhikari S., et al. "Effect of Invitro Zinc (II) supplementation on Normal and Cancer Cell lines," International Journal for Research in Applied Science & Engineering Technology (IJRASET), Vol. 3 ,pp. 2321-9653, 2015.

**[8]** Holliday D.L. and V. Speirs, "Choosing the right cell line for breast cancer research," Breast Cancer Research, vol. 13, pp. 215, 2011.

**[9]** Welsh J. *Chapter 40 - Animal Models for Studying Prevention and Treatment of Breast Cancer, in Animal Models for the Study of*

*Human Disease*, P.M. Conn, Editor. Academic Press: Boston, 2013,

**[10]** Lee A.V. S. Oesterreich, and N.E. Davidson, "MCF-7 cells--changing the course of breast cancer research and care for 45 years," J Natl Cancer Inst,vol. 107, pp. 1-4, 2015.

**[11]** Segeritz C.-P. and L. Vallier, *Chapter 9 - Cell Culture: Growing Cells as Model Systems In Vitro, in Basic Science Methods for Clinical Researchers, M. Jalali, F.Y.L. Saldanha, and M. Jalali, Editors.* 2017, Academic Press: Boston.

**[12]** Croce A.C. and G. Bottiroli, "Autofluorescence spectroscopy and imaging: a tool for biomedical research and diagnosis," Eur J Histochem, vol. 58, pp. 2461, 2014.

**[13]** Tatjana D. and M. Dramicanin, *Using Fluorescence Spectroscopy to Diagnose Breast Cancer. Chapter metrics overview*, 2016.

**[14]** Monici M. "Cell and tissue autofluorescence research and diagnostic applications, in Biotechnology Annual Review," Elsevier. vol. 11, pp. 227-256, 2005.

**[15]** Martínez-Reyes I. and N.S. Chandel, "Cancer metabolism: looking forward," Nature Reviews Cancer, vol. 21, pp. 669-680, 2021.

**[16]** Yang Y.L., et al. "Characteristic autofluor-rescence for cancer diagnosis and its origin," Lasers Surg Med, vol. 7, pp. 528-532, 1987.

IJBB International Journal of Biophotonics & Biomedical Engineering Vol. 4, No. 2, Fall - Winter, 2024

Research Article

# An Advanced Method to Voxelize a Tissue Using CT Scan Images and Medical Imaging

**S. A. Mousavi Shirazi** [a]

*a Department of Physics, South Tehran Branch, Islamic AZAD University, Tehran, Iran.*

***Corresponding Author Email: alireza.mousavishirazi@gmail.com**

**DOI: 10.71498/ijbbe.2024.1188107**

**ABSTRACT**

Received: Oct. 24, 2024, Revised: Jan. 7, 2025, Accepted: Jan. 26, 2025, Available Online: Feb. 17, 2025

*This study focused on medical imaging for X-ray radiotherapy. To conduct the research, liver tissue was outlined using CT images of the abdominal area. The precise geometry of the segmented liver tissue was then simulated and created with specialized medical imaging software. Initially, the Hounsfield Unit for each tissue type in the body was determined, followed by defining the constituent materials, which were then input into MATLAB code. Next, based on its radiodensity, the abdominal tissue was uniformly filled with the appropriate material. Subsequently, the liver tissue was outlined and segmented within the abdominal tissue, and the precise geometry of the segmented liver tissue was created as input data. This approach can be applied to any patient using their individual CT scan images.*

**KEYWORD**

*CT, Liver, Medical Imaging, Tissue, Voxelization.*

## I. INTRODUCTION

The initiation of advanced tomographic and computer imaging methods in the late 1980s marked the beginning of a novel era for VOXEL phantoms [1].

In radiotherapy, there is a need to minimize the dose delivered to healthy tissues. Simultaneously, accurately measuring and evaluating the absorbed dose is of primary importance [2, 3]. X-ray photon-based cancer therapy is a commonly used treatment method in medical radiation. This study aimed to develop medical imaging techniques that can be utilized in dosimetry to examine the behavior of beams in tissues. To validate the effectiveness of the developed imaging, a dosimetric approach was applied to real tissue using DICOM images from computed tomography (CT) scans [4, 5].

The current technologies still have many critical limitations. The voxelization process itself demands a substantial amount of computational power, which limits the use of current technologies. Some tissues lack reference values, such as the skin, gallbladder wall, major blood vessels, bronchi, and adipose

tissue. Modeling very thin structures, like the oral mucosa skin, and bone endosteum, crucial for radiation protection, is practically impossible. Using extremely small VOXELs for such thin structures needs an enormous amount of computer memory, and the computation process is very slow [6, 7].

A significant advancement came with the advancement of CT and magnetic resonance imaging (MRI), which are capable of producing highly accurate digital 3D images of internal organs. In the VOXEL model, diagnostic data is converted into a volumetric pixel format, enabling the recreation of the human body in digital 3D form. To achieve this, raw data from CT or MRI scans must be obtained, and the body's components need to be segmented and separated from other tissues [8]. Each component's density and composition must be determined, and this information must be incorporated into a unified 3D structure [9, 10]. Additionally, the majority of scans of a single subject capture merely a body's small section, while a series of full scans is required to obtain meaningful data. Managing this data can be challenging [11]. During a Monte Carlo simulation, it is impossible to deform or move the phantom internal organs, which necessitates precise modeling of organs in simulations (such as for imaging of moving organs, 4D radiotherapy, and radiation therapy). This represents a significant restriction [12].

## II. Materials and Methods

The CT scan images of the abdominal tissue of a 45-year-old man were obtained by 80 keV photons from the single direction at the Cartesian coordinates, which were viewed from the XZ direction, showing the liver ventral view.

In this research, 85 DICOM images were selected from the YZ axes in the Cartesian coordinates to allow for the observation of the front view of the tissue.

A large lattice is defined in such a way that it can be subdivided into highly small lattices using specialized software. Their resolution can be adjusted as needed. Their resolution was set to 1mm3. Every volume made by this program plays the role of one VOXEL. Every VOXEL is completely homogenous and filled up using the related matter (abdominal tissue matters) which has self-density. Then, these VOXELs cover all the abdominal tissue. While the abdominal tissue contains liver tissue, contouring the liver tissue and separation of its slices are very difficult.

The related figures have been illustrated as follows [13, 14].

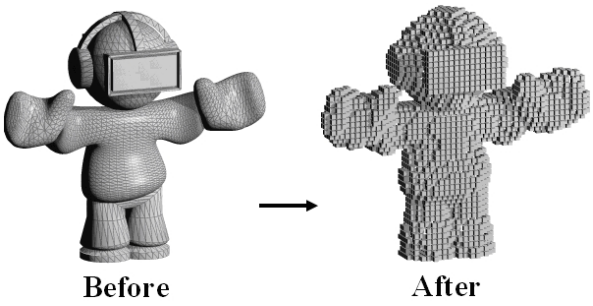


Fig. **1** The image of a manikin before and after voxelization

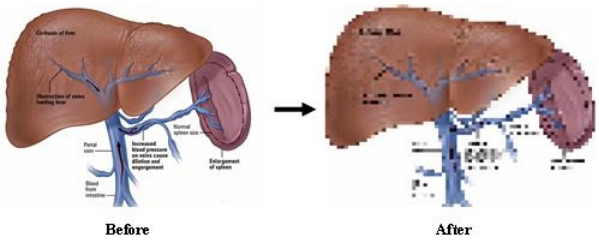


Fig. **2** The image of the liver before and after voxelization

Some of the requirements in the VOXEL model are as follows:
1- Requiring the individual organ topology, 2- Requiring the individual organ masses, 3- knowing the values of tissues.

In this investigation, the contoured shape of liver tissue has been considered. Following voxelization and filling the abdominal tissue using appropriate compounds, the liver tissue

underwent contouring and segmenting within the abdominal area.

This contouring process involves filling the remaining materials in other tissues and sections of the abdomen with air.

The VOXEL phantom can be typically described as a rectangular array of VOXELs containing only the body region along with some surrounding air [15].

Since the rectangular array is treated as one entity, it is challenging or nearly impossible with most software to define an organ near its region unless it is inserted and voxelized within that area. The surrounding air regions can be reduced to represent the VOXEL region instead of using a rectangular array, but those regions cannot be eliminated. The VOXEL phantom limitations also pose considerable challenges in proton beam treatment simulations, in which the beam nozzle and other equipment should be modeled near the body region [16, 17, 18].

The scanned images (slices) are then processed into new images using specific MATLAB programming.

This program generates numerous volumes as lattices, with each lattice being repeated to construct the complete geometry of the tissue. Each material, such as air, water, soft, bone, etc., has its radiodensities. Then, these VOXELs cover all the abdominal tissue.

The type of each material is determined using the Hounsfield Unit (HU) scale of DICOM CT slices. Each pixel in the slices corresponds to one voxel, establishing a correlation between the HU and each voxel. Therefore, the existing voxels in the abdominal tissue are identified using MATLAB software, which analyzes the grayness level of the CT slice along with its associated HU. Each tissue in the abdominal area is described based on the HU considering the following equation [19, 20].

$$HU = \frac{\mu_X - \mu_{water}}{\mu_{water} - \mu_{air}} \times 1000 \quad (1)$$

Where:

$\mu_{water}$: water linear attenuation coefficient.

$\mu_X$: linear attenuation coefficient for a material X.

$\mu_{air}$: air linear attenuation coefficient.

The HU values related to some other body tissues are calculated for the MATLAB programming based on their HU calculations and through their μX, and they are added to the prior-defined materials.

There are the radiodensities of materials existing in the liver tissue defined based on HU for each cell. As every VOXEL has a self-CT number, each radiodensity is accurately associated with that of the cell. However, every VOXEL will have its related radiodensity [21].

The HU values and μ for some body tissues can be shown for MATLAB programming according to Tables 1 and 2, respectively.

TABLE. **1** THE HU VALUES FOR DIFFERENT BODY TISSUES APPLIED FOR MATLAB PROGRAMMING [22]

| Tissue | HU values |
|---|---|
| Air | -1000 |
| Fat | -100 |
| Breast | -150 |
| Lung | -880 |
| Muscle | 100 |
| Liquid | -2 |
| Soft | 1 |
| Water | 0 |
| Aluminum | 2640 |
| Bone | 400 |

TABLE. **2** LINEAR ATTENUATION COEFFICIENT VALUES ($CM^{-1}$) RELATED TO SELECT TISSUES AT VARIOUS X-RAY PHOTON ENERGIES [23]

| Tissue (material) | 40 keV | 60 keV | 80 keV | 100 keV |
|---|---|---|---|---|
| Fat | 0.228 | 0.188 | 0.171 | 0.160 |
| Water | 0.268 | 0.206 | 0.184 | 0.171 |
| Bone | 1.28 | 0.604 | 0.428 | 0.356 |
| Aluminum | 1.535 | 0.750 | 0.545 | 0.460 |
| Titanium | 10.05 | 3.48 | 1.840 | 1.235 |

To accurately identify the initial slice of the DICOM CT scan where the liver tissue begins, a reference point must be established using DICOM images from three perspectives in

Cartesian coordinates (XY, YZ, and XZ). Assuming the cancerous tumor in the liver tissue for tumor contouring, the DICOM CT slices are analyzed starting from the point where the tumor becomes visible at the end of its depth.

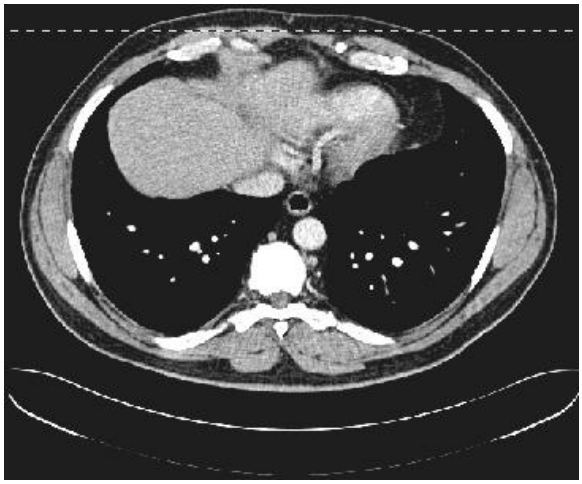

Fig. **3** Slice No. 36 of 237 CT slices from XZ direction through holding slice No. 18 in XY direction

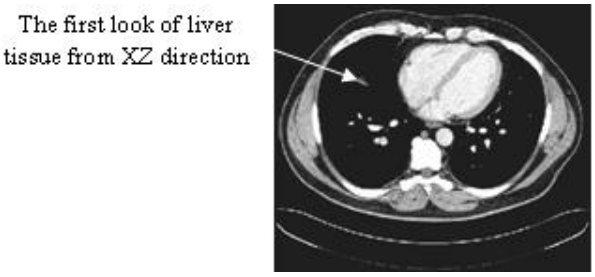


Fig. **4** Slice No. 13 of 237 CT slices in the XZ direction.

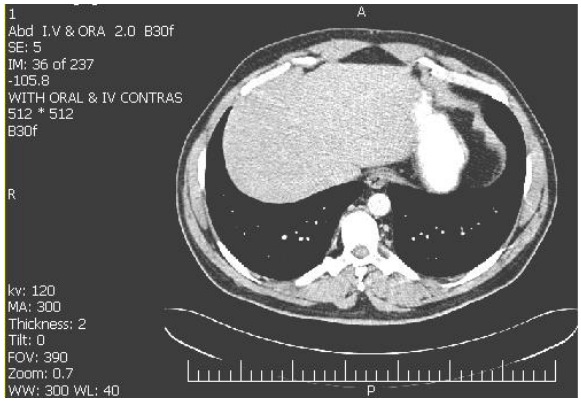


Fig. **5** The image of abdominal tissue's slice by CT scanning from an X-Z view

This specific program plays a significant role in converting the images scanned by CT scanning equipment into the inputting data of MCNPX code in a way that all the liver geometry is defined from CT imaging to the inputting data of MCNPX code. It means the liver geometry is finally described from CT imaging into inputting data of MCNPX code; thereby simulation of a real liver tissue is done.

Finally, for the sake of dose calculation, at this time, the materials existing in the liver tissue are described as input for the MCNPX Code, the MCNPX programming is run, and the precise absorbed doses are finally achieved. In that case, every part of the abdominal tissue is automatically colored by the MCNPX code based on the material number.

## III. Results and Discussion

Some abdominal region plots, converted using MATLAB, were consecutively shown in two steps (Figure 6).

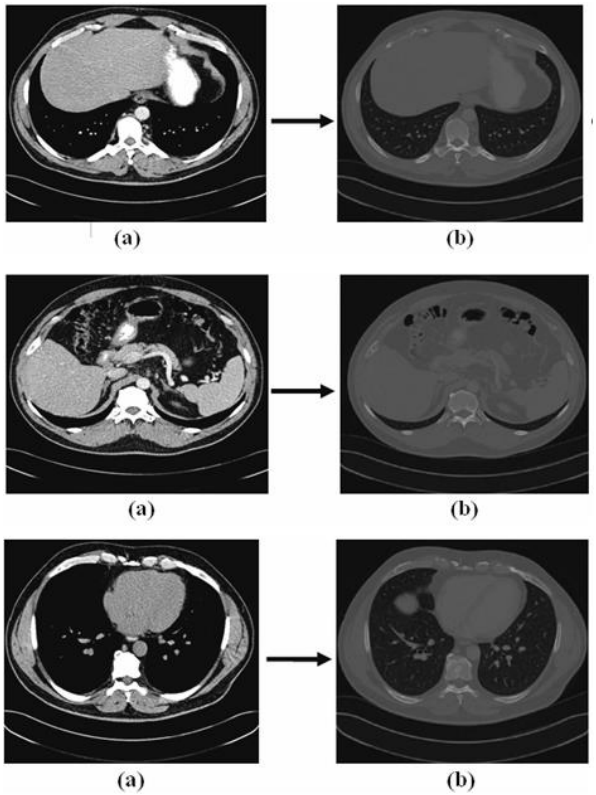


Fig. **6**(a) Image of abdominal tissue slice by CT scanning (b) Image of abdominal tissue converted using MATLAB from CT image

The total absorbed dose amount in the liver tissue is illustrated in Fig 7:

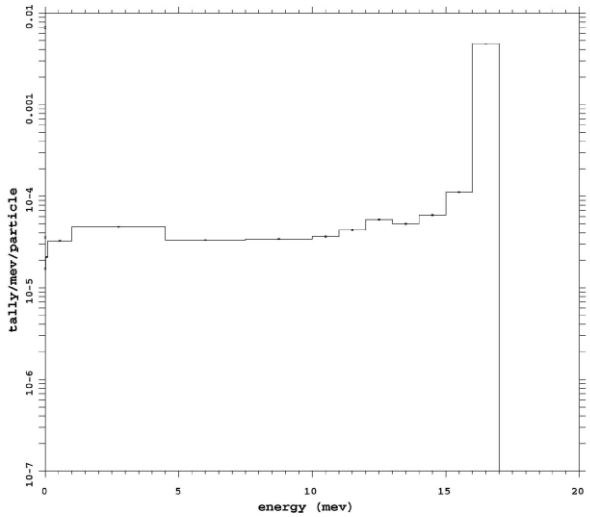


Fig. **7** The overall absorbed dose in the segmented liver tissue using liver voxelization (plotted using MCNPX code)

In another section, abdominal tissue DICOM images were used. Using MATLAB and these DICOM images, the abdominal tissue-surrounded liver tissue was isolated followed by irradiation using photon-X, comparable to the liver phantom.

## IV. Conclusions

It was concluded the method presented in this research can be applied for radiation dosimetry for patients undergoing various radiotherapy courses, such as Boron Neutron Capture Therapy (BNCT). Additionally, it can be widely implemented for different types, forms, and sizes of tissues. This imaging method can also be used for dosimetric purposes and to analyze the behavior of radiation beams within liver tissue components. DICOM images are adaptable for any body tissue, making it easier to consider a cancerous mass or tumor in the liver tissue and break down its constituent elements. When applying DICOM images from CT scans in dosimetry, this approach is applicable for each case using their own CT scan images to calculate the allowable equivalent and absorbed doses, after the procedures outlined.

By applying this method, the precise absorbed dose can be calculated in the whole of a tissue and its constituent elements in radiotherapy as accurately as possible.

Therefore, the advantage of this method is that it can be personalized for each patient using their own CT scans to determine the acceptable absorbed dose, and all the procedures described in this study can be applied. Additionally, this method could be extended to other radiotherapies, such as proton or photon treatments.

## References

**[1]** Kramer R, Cassola V.F, Khoury H.J, Vieira J.W, de Melo Lima V.J, and Brown K.R, "FASH and MASH: female and male adult human phantoms based on polygon mesh surfaces: II. Dosimetric calculations," Physics in medicine & biology. vol. 55, pp.163, 2009.

**[2]** Reginatto M. "What can we learn about the spectrum of high-energy stray neutron fields from Bonner sphere measurements," Radiation Measurements. vol. 44, pp. 692-699, 2009.

**[3]** Morris S, Roques T, Ahmad S, and Loo S, *Practical radiotherapy planning.* CRC Press, 2023.

**[4]** Shirazi S.A and Shafeie Lilehkouhi M.S. "The assessment of radioisotopes and radiomedicines in the MNSR reactor of Isfahan and obtaining the burnup by applying the obtained information," Asia-Pacific Power and Energy Engineering Conference, vol. , pp. 1-4, 2012.

**[5]** Mousavi Shirazi S.A and Rastayesh S. "The comparative investigation and calculation of thermo-neutronic parameters on two gens II and III nuclear reactors with same powers," fuel. Vol. 100, pp. 60, 2011.

**[6]** Zankl M, Becker J, Fill U, Petoussi-Henss N, and Eckerman K.F. "GSF male and female adult voxel models representing ICRP Reference Man–the present status," The Monte Carlo Method: Versatility Unbounded in a Dynamic Computing World. vol. 1721, pp. 1-13, 2005.

**[7]** Eckerman KF, Update on ORNL RBE Work. ISCORS Meeting. 2011 Oak Ridge, USA.

**[8]** Ji S and Zhao W. "Displacement voxelization to resolve mesh-image mismatch: application in deriving dense white matter fiber strains,"

Computer methods and programs in biomedicine. vol. 213, pp.106528, 2022.

**[9]** Griffin KT, Cuthbert TA, Dewji SA, and Lee C. "Stylized versus voxel phantoms: a juxtaposition of organ depth distributions," Physics in Medicine & Biology. vol. 65, pp. 065007, 2020.

**[10]** Zaidi H and Xu XG. "Computational anthropomorphic models of the human anatomy: the path to realistic Monte Carlo modeling in radiological sciences," Annu. Rev. Biomed. Eng. vol. 9, pp. 471-500, 2007.

**[11]** Yan S and Fang Q. "Hybrid mesh and voxel based Monte Carlo algorithm for accurate and efficient photon transport modeling in complex bio-tissues," Biomedical Optics Express. vol. 11, pp. 6262-6270, 2020.

**[12]** Rajon D.A, Jokisch D.W, Patton P.W, Shah A.P, and Bolch W.E. "Voxel size effects in three‐dimensional nuclear magnetic resonance microscopy performed for trabecular bone dosimetry," Medical physics. vol. 27, pp. 2624-2635, 2000.

**[13]** Fisher Jr H.L and Snyder W.S, "Distribution of dose in the body from a source of gamma rays distributed uniformly in an organ," InProceedings of the First International Congress of Radiation Protection. vol. 1968 , pp. 1473-1486, 1968.

**[14]** Kramer R, Khoury H.J, Vieira J.W, Loureiro E.C, Lima V.J, and Lima F.R, "Hoff G. All about FAX: a Female Adult voXel phantom for Monte Carlo calculation in radiation protection dosimetry," Physics in Medicine & Biology. vol. 49, pp. 5203, 2004.

**[15]** IAEA-TECDOC-1223. Current status of neutron therapy. Austria (Vienna): International Atomic Energy Agency; 2001 May.

**[16]** Lee C, Lodwick D, Hasenauer D, Williams J.L, Lee C, and Bolch W.E. "Hybrid computational phantoms of the male and female newborn patient: NURBS-based whole-body models," Physics in Medicine & Biology. vol. 52, pp. 3309, 2007.

**[17]** Xu X.G, Taranenko V, Zhang J, and Shi C. "A boundary-representation method for designing whole-body radiation dosimetry models: pregnant females at the ends of three gestational periods—RPI-P3,-P6 and-P9," Physics in Medicine & Biology. vol. 52, pp. 7023, 2007.

**[18]** Zhang J, Na Y.H, Caracappa P.F, and Xu X.G. "RPI-AM and RPI-AF, a pair of mesh-based, size-adjustable adult male and female computational phantoms using ICRP-89 parameters and their calculations for organ doses from monoenergetic photon beams," Physics in Medicine & Biology. vol. 54, pp. 5885, 2009.

**[19]** Wambaugh J and Shah I. "A model for micro-dosimetry in virtual liver tissues," The 10th International Conference on Systems Biology Stanford, 2009.

**[20]** Stenvall A, Larsson E, and Strand S.E, "Jönsson BA. A small-scale anatomical dosimetry model of the liver," Physics in Medicine & Biology.vol. 59, pp. 3353, 2014.

**[21]** Yoon H, Lee S.K, Kim J.Y, and Joo M.W. "Quantitative Bone SPECT/CT of Central Cartilaginous Bone Tumors: Relationship between SUVmax and Radiodensity in Hounsfield Unit," Cancers. vol. 16, pp.1968, 2024.

**[22]** Hounsfield G.N. "Computed medical imaging," Science. vol. 210, pp. 22-28, 1980.

**[23]** Reeves T.E Mah P, and McDavid W.D. "Deriving Hounsfield units using grey levels in cone beam CT: a clinical application," Dentomaxillofacial radiology. vol. 41, pp.500-508, 2012.

IJBBE International Journal of Biophotonics & Biomedical Engineering Vol. 4, No. 2, Fall - Winter, 2024

Research Article

# Investigating the Effect of Soluble and Insoluble Medicinal Substances on Cell Wall Orientation

**N. Ebrahimpour [a], M. Sadegh Zakerhamidi [b], A. Ranjkesh[c]**

*a Department of Chemical Industry, National University of Skills (NUS), Tehran, Iran*
*b Faculty of Physics, University of Tabriz, Iran*
*cCondensed Matter Department, J.Stefan Institute, Jmova 39, Ljubljana, Slovenia*

***Corresponding Author Email: neda.ebrahimpour@gmail.com**

**DOI: 10.71498/ijbbe.2024.1190467**

**ABSTRACT**

Received: Nov. 14, 2024, Revised: Jan. 3, 2025, Accepted: Jan. 26, 2025, Available Online: Feb. 18, 2025

*Considering that the cell wall is the first defense and control barrier of medicinal substances into the cell, any dielectric behavior of this divider can lead to harm to the cell or the absorption of substances from the environment; hence, examining the dielectric and physicochemical behavior of the anisotropic cell wall is imperative. The present study employs 1102 (a mixture of liquid crystals) as an anisotropic environment, similar to the cell wall. In insoluble nanoparticles, Lithium disilicate ($Li_2Si_2O_5$) is employed as a non-reactive material, while materials containing active agents are used as soluble materials like Retinol ($C_{20}H_{30}O$). At various dopant concentrations, the dielectric characteristics and optical anisotropies of the liquid crystal and dopant mixture were observed, and the resulting data was analyzed and studied results indicate that the shape of the insoluble dopant influences the molecular order of the liquid crystal bulk, while for soluble substances, the percentage of dopant is more significant than the shape of dopants in the ordering of anisotropic media.*

**KEYWORDS**

*Cell Wall, Liquid Crystal, Nanoparticle, Dielectric Constant, Refractive Index.*

## I. INTRODUCTION

It is believed that cells are the smallest building blocks of life. Every cell has a cytoplasm and a cell wall. The cell wall, which is regarded as the cell border, is a coating that envelops the cytoplasm or the contents [1]. The cell wall performs the following functions: bulk transport: exocytosis and endocytosis, markers and signaling, metabolic activities, mechanical structure, defines and encloses the cell, selective permeability, dynamic transport, and so on [2],[3]. As is well known, the cell wall is a dynamic, complex structure made up of a bilayer of phospholipids. The hydrophilic groups cover the inner and outer surfaces of the phospholipids, whereas the hydrophobic ends of the lipids create an intermediate layer. The foundation of membranes is made up of lipid bilayers, and cholesterol may control how fluid the membrane is. Numerous proteins are essential for the operations of the cell membrane, including signal transduction and ion transport [4],[5]. Charged ions and electrons are unable to pass across the wall in large quantities. They may pass across membranes from membrane-spanning protein semiconductors and specialized ion channels, respectively [6]. The anisotropic behavior of living cell walls has been confirmed by several

studies and researches [7]-[9]. Thus, by applying special environmental qualifications, it is achievable to impact the anisotropic properties of the cellular system and induce desired behaviors in it [8]. Properties such as the dielectric properties and physicochemical behavior of cell walls can be improved by taking advantage of this anisotropic property [9]-[11]. There is a large body of published literature demonstrating that the presence of nano-dopants in the environment interacting with the cell walls can affect the above properties [12]-[14]. The extent of these changes depends largely on the shape of the dopants in the environment and their concentration [15].

Substances that flow like liquids but yet have some of the crystals' ordered structure are known as liquid crystals [16],[17]. Molecules in liquid crystals typically exhibit elongation and directionality. Between the crystalline (solid) and isotropic (liquid) phases, there is a unique phase of matter known as the liquid crystal state [18]. Since liquid crystals are anisotropic materials, the system's average alignment with the direction affects its physical characteristics. A high alignment indicates a highly anisotropic material. Likewise, the material is nearly isotropic if the alignment is modest [19].

Nematic liquid crystal materials are characterized by long-range orientation order but lack translational order. A form of optical anisotropy called birefringence is also present in most NLCs (Nematic Liquid Crystals). Birefringence is seen in liquid-crystalline phases because of the parallel order of molecules that exhibit anisotropy in polarizability. The amplitude and sign of the birefringence are determined by the composition and organization of the liquid-crystalline phase and the polarizability properties of the constituent molecules [20],[21]. As previously mentioned, liquid crystals and cell walls share many of the same characteristics, like orientational organization, three-dimensional designs, and anisotropic properties, making them an ideal choice to study the anisotropic behavior of cell walls in the presence of nano dopants [22],[23],[25]. It is also possible to use nanoscale pharmaceutical substances as dopants and study the effect of their presence in different concentrations and morphologies on the anisotropic properties of cell wall [24],[27].

## II. Experimental

### A. *Materials*

The present study employs 1102 (a mixture of liquid crystal) as an anisotropic environment, similar to the cell wall. LC (Liquid Crystal) 1102 ($T_{NI}$ = $80.5^0$ C), is essentially a mixed cyanobiphenyl liquid crystal that is used in both industrial and research applications. The manufacturing company has a patent on the materials that make up Liquid Crystal 1102.

Insoluble nanoparticle, lithium disilicate ($Li_2Si_2O_5$) crystals of 50-60 nm are employed as non-reactive material, while materials containing active agents are used as soluble materials like Retinol ($C_{20}H_{30}O$) (CAS No.68-28-8). Mixtures of the liquid crystal composition and the dopants with different weight ratios (0.1%, 0.3%, and 0.7% w/w%) were prepared. The nano dopants were added to the NLC in the isotropic phase of 1102, and the mixture was sonicated for six hours to complete the doping process and their dielectric constants and refractive indices were measured in a specific temperature range.

### B. *Liquid crystal cell preparation*

To create the LC cells, the NP-NLC (Nano Particles- Liquid Crystal) solutions were sandwiched between two 1.2 $cm^2$ optical glass plates that had transparent electrodes composed of indium tin oxide (ITO) layers. By applying a polyvinyl alcohol surface treatment and rubbing, the sample cells were arranged in a parallel fashion or homogenous orientation. We treated the LC cells' surfaces with lecithin to enable homeotropic alignment. The distance between the electrode surfaces, which was 1µm, was fixed using a Mylar sheet which set the thickness of the liquid crystalline samples. Lastly, epoxy resin glue was employed as a sealing material to attach the plates.

### C. *Refractive index measurement*

Abbe's refractometer (*Bellingham Stanley Abbe 60ED*) has been used to measure the refractive index with an accuracy of 0.00001. Abbe's refractor ocular has a polarizer sheet installed to block the unusual rays. This eliminates the boundary line's contrast. Water was circulated in a water bath temperature controller to regulate the temperature of Abbe's refractometer. A thermometer with an accuracy of ±0.01 °C was placed close to the sample to measure the temperature. The extraordinary refractive index, $n_e$, is too high to be measured with the available refractometer, but the ordinary refractive index, $n_o$, can be directly measured in the nematic phase. As a result, $n_e$ at every temperature was calculated using $< n >= \frac{1}{3}(n_e + 2n_o)$ . The extrapolated average refractive index, or <*n*>, in this case, is the result of extending the isotropic phase's ($n_{iso}$) refractive index into the range of the nematic phase. Birefringence ($\Delta n = n_e - n_o$) of the nematic phase for the examined LCs was computed using these data.

The order parameter S for the pure liquid crystal sample and the NP-NLC samples (0.1%, 0.3% and 0.7% w/w%) can be computed using the obtained values for the refractive indices and Vuks assumption:

$$S\left(\frac{\Delta\alpha}{\alpha}\right) = \frac{(n_e^2 - n_o^2)}{\langle n^2 \rangle - 1} \quad (1)$$

Where $\Delta\alpha = \alpha_e - \alpha_o$ is anisotropy of polarizability and $\alpha$ demonstrates mean molecular polarizability. We exploit $\frac{(n_{e,o}^2 - 1)}{(\langle n^2 \rangle + 2)} = \frac{4\pi}{3} N\alpha_{e,o}$ for estimating respective molecular polarizabilities ($\alpha_e$, $\alpha_o$) and *N* is the number of molecules per unit volume and $<n^2>$ is defined as $< n^2 >= \frac{1}{3}({n_e}^2 + 2{n_o}^2)$.

Plotting the linear portion of $ln\frac{3({n_e}^2 - {n_o}^2)}{{n_e}^2 + 2{n_o}^2 - 3}$ versus ln $(1 - {}^{T}/_{T_c})$ allows for the determination of $\frac{\Delta\alpha}{\alpha}$, This can be extended to *T=0K*. The scaling factor $\Delta\alpha/\alpha$ is determined by the intercept at *T= 0K*, where a completely ordered structure exists (*S=1*). Order parameter *S* values at various temperatures can be obtained by assuming that $\Delta\alpha/\alpha$ stays constant across all temperatures and entering this value into Eq. (1).

### D. *Dielectric measurement*

The dielectric measurements have been performed by an LCR meter having an accuracy of 0.0005. Instek LCR 819, which is combined with a cell temperature controller, the temperature was stabilized with the accuracy of 0.01 °C. For dielectric measurements, a sandwiched capacitance sample with an aligner layer of polymer was utilized. Parallel and perpendicular directions were used to measure the dielectric. At various temperatures, the capacitance values of the sample were ascertained in both its filled and empty forms. Once the impacts of the conductive, ITO layer, and alignment polymer layer are eliminated using Eqs. (2), (3) the change in capacitance will yield the value of the real part of permittivity.

$$\varepsilon_{\parallel} = {}^{C_{\perp}}/_{C_0} \quad (2)$$

$$\varepsilon_{\perp} = {}^{C_{\parallel}}/_{C_0} \quad (3)$$

where $\boldsymbol{C}_{\perp}$ and $\boldsymbol{C}_{\parallel}$ are the oriented LC capacitances perpendicular to and parallel to the cell surface, respectively. $\boldsymbol{C_o}$ is the associated empty cell's capacitance and $\boldsymbol{\varepsilon}_{\parallel}$ and $\boldsymbol{\varepsilon}_{\perp}$ are parallel and perpendicular dielectric constants to the long molecular axis.10 kHz frequencies were used to measure the capacitances.

At various temperatures, the capacitance values of the samples were ascertained in both their filled and empty states. The value of the real part of the constant will be obtained by measuring the change in capacitance after the effects of the conductive, ITO and alignment polymer layers have been eliminated, using Eqs. (2), (3).

## III. RESULTS AND DISCUSSIONS

### A. *Refractive index studies*

The temperature ranges in which the live cell is stable were used to study the birefringence property and order parameter behavior of pure and doped liquid crystal with soluble and insoluble nano additives at varying concentrations. It is essential to highlight that this study employs a unique nematic liquid crystal for optimal simulation. Unlike typical liquid crystals, this particular substance exhibits an increase in its order parameter as the system's temperature rises within the measured range. This behavior is similar to the response of cell walls in the body's aqueous environment at physiological temperatures. The molecular order changes with temperature, which accounts for the temperature dependency of the birefringence.

The temperature-dependent birefringence of NP-NLC composite systems (0.1%, 0.3%, and 0.7% w/w%) and pure LC systems is displayed in Fig.1. Temperature monitoring of the ordinary and extraordinary refractive indexes ($n_o$, $n_e$) of pure and doped liquid crystal 1102 with different concentrations (0.1%, 0.3%, and 0.7% w/w%) of Retinol ($C_{20}H_{30}O$) and $Li_2Si_2O_5$ nanoparticles as soluble and insoluble dopants, in a specific temperature range (310<T<323K) reveals that the extraordinary refractive index in all samples increased significantly with increasing temperature, whereas the coefficient of ordinary refractive index in the same conditions decreased more gently. However, a comparison of data from the pure and doped states of the tested nematic liquid crystal for both of dopants, reveals that the presence of nanoparticles has reduced the ordinary and extraordinary refractive indices and this reduction trend is directly related to an increase in dopant concentration, particularly at higher dopant concentrations.

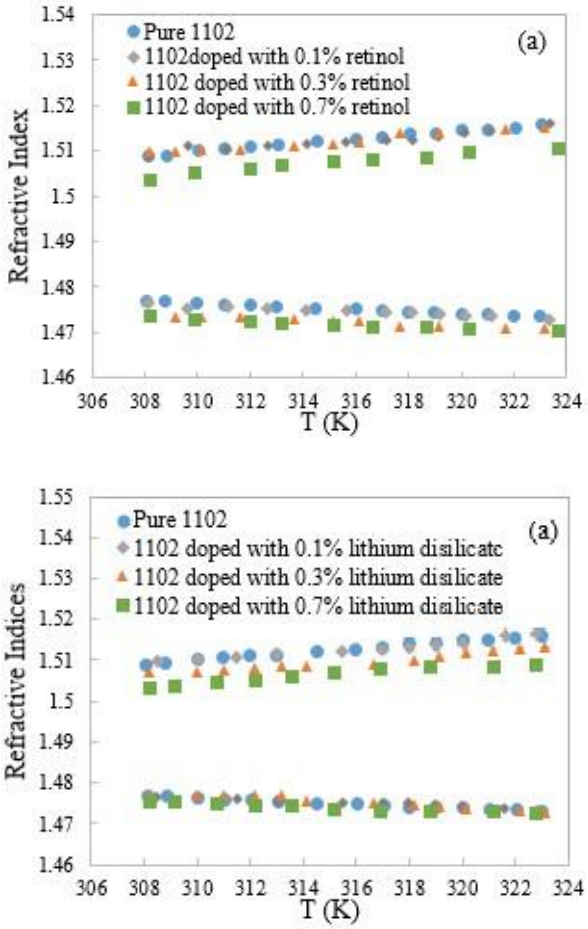


Fig. 1 Temperature monitoring of refractive indices of pure and doped 1102 with (0.1, 0.3, and 0.7% w/w%) retinol (a) and lithium disilicate (b)

The birefringence ($\Delta n$) values of the pure 1102 LC and composite systems (1102-Retinol), indicate an increasing tendency as the temperature increases in the tested temperature range Fig.2.

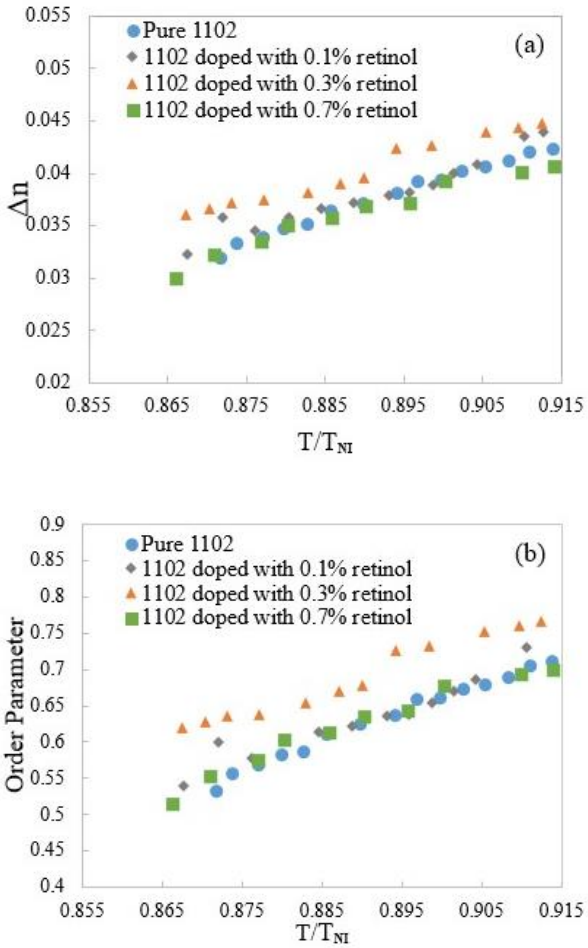


Fig. **2** Temperature monitoring of birefringence (a) and order parameter (b) of pure and doped 1102 with (0.1, 0.3, and 0.7% w/w%) retinol.

Comparing the graphs of changes in the birefringence index and the order parameter of the pure and doped liquid crystal with the mentioned concentrations for Retinol dopants shows that the behavior of these factors in the 1102-retinol mixtures (0.1%, 0.3% and 0.7% w/w%) in the measured temperature range indicate that the presence of Retinol nanoparticles has caused an increase in these values, increases behavior varies depending on the concentration of dopant used. It is evident that, in comparison to the pure state of 1102 LC, the birefringence coefficient and the order parameter of the composition were not significantly affected by the 0.1% Retinol dopant present.

But when the concentration is raised to 0.3%, these parameters noticeably increase. This could be because the compound's intrastructural order is increased as a result of the interaction between the dopant and liquid crystal molecules of 1102, which forms hydrogen bonds between them. As the monitoring continues, a decrease in the order parameter and the birefringence factor can be seen by increasing the dopant concentration to 0.7%. This could be the consequence of an increase in the dopant-dopant intermolecular interactions, which in turn causes a decrease in the order of orientation of the liquid crystal molecules.

In summary, at low concentrations, dopant-dopant interactions are less intense due to fewer particles in the liquid crystal matrix. When the concentration is raised to 0.3%, dopant-dopant interactions increase and hydrogen bonds are formed. At 0.7%, dopant-dopant interactions increase, resulting in aggregation phenomena resembling surfactants. This suggests that retinol's presence in the liquid crystal system resembles surfactant behavior at the Critical Micelle Concentration (CMC) [26].

This alteration demonstrates that the anisotropic liquid crystal structure's internal molecular order is influenced by the presence of dissolved nanoparticles, with the dopant concentration being the primary determinant of this effect.

Put differently, the number of nanoparticles influences the kind of interactions that control the mixture, which alters the molecules' orientation order and results in disruption.

In insoluble doped NLC samples, $Li_2Si_2O_5$ doped NLC samples had a significantly lower order parameter and birefringence index than pure liquid crystal samples Fig. 3.

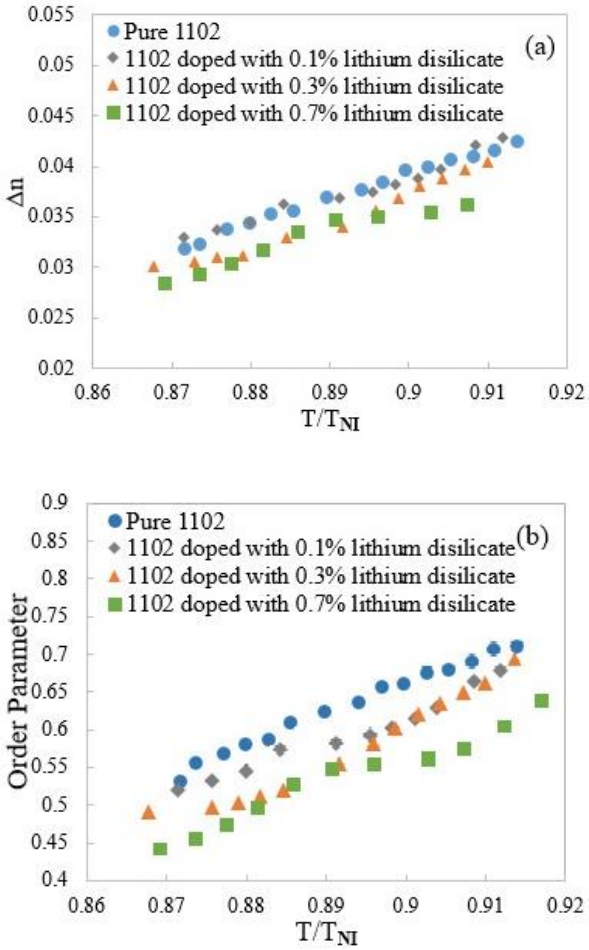


Figure. **3** Temperature monitoring of birefringence (a) and order parameter (b) of pure and doped 1102 with (0.1, 0.3, and 0.7% w/w%) lithium disilicate.

However, the rise in dopant concentration had a relatively low effect on this drop; we did not observe a proportional decrease in the order parameter and birefringence index as the dopant concentration grew to 0.1% w/w%. However, as the concentration and number of dopant particles in the mixtures increase, the effect of steric hindrance of lithium disilicate molecules becomes more apparent, resulting in a decrease in the interaction between the liquid crystal molecules with each other, a disruption in the liquid crystal's internal structural order, and a decrease in the order parameter of NLC doped with 0.3% and 0.7% w/w% lithium silicate compounds.

### B. *dielectric properties studies*

Initially, prepared mixtures were placed inside the made cells to test the dielectric constant of the NPs–NLC composites at various concentrations of the Retinol and $Li_2Si_2O_5$ nanoparticles. Next, using Eq. (2) and (3), the dielectric constant of the NPs–LC composites was determined. The dielectric constants' parallel ($\varepsilon_{\parallel}$) and perpendicular ($\varepsilon_{\perp}$) components vary with temperature as seen in Figs. 4 and 5. In the temperature range of the experiment, as the temperature rises, the value of ($\varepsilon_{\parallel}$) falls for the mostly parallel ordering for all samples, as seen in Figs. 4 and 5. But in this temperature range, the ($\varepsilon_{\perp}$) parameter remains nearly constant. ($\varepsilon_{\parallel}$) displays a greater value than ($\varepsilon_{\perp}$) because we employed a positive dielectric anisotropy of the NLC at this point. The dielectric constant of the NPs–NLC composites varies by the presence of NPs at different percentages, as seen by the behavior of the parallel and perpendicular dielectric constant in Figs. 4 and 5.

The data indicates that the incorporation of retinol as a dopant has resulted in an enhancement of both the parallel $\varepsilon_{\parallel}$ and vertical $\varepsilon_{\perp}$ dielectric coefficients in the liquid crystal-retinol mixture. Furthermore, as the concentration of retinol increases, there is a corresponding rise in the positive displacement of these values.

Notably, the liquid crystal 1102 combined with 0.7% w/w% retinol exhibits the most significant increase in the parallel dielectric coefficient. This effect can be attributed to the multiple bonds present in the molecular structure of retinol, which facilitate the electron transfer process when subjected to an electric field. In this case, even while the system order parameter decreases, the aggregation phenomenon at high retinol concentrations leads to the aggregation of polar components, the formation of a bigger dipole, and easier electron transmission in the system.

The investigation into the dielectric properties of 1102 liquid crystal infused with lithium silicate nanoparticles at specified concentrations (0.1%, 0.3%, and 0.7% w/w) reveals that the incorporation of these nanoparticles has led to a decrease in the numerical values of both the parallel and perpendicular ($\varepsilon_{\parallel}$ , $\varepsilon_{\perp}$) dielectric coefficients of the liquid crystal composition.

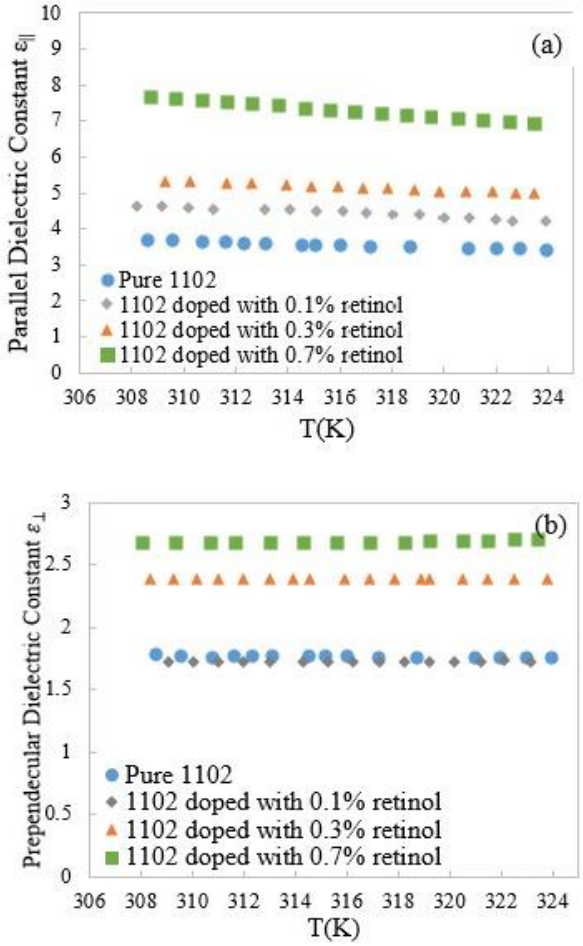


Fig. **4** Temperature monitoring of parallel $\varepsilon_{\parallel}$ (a) and perpendicular $\varepsilon_{\perp}$ (b) dielectric constants of pure and doped 1102 with (0.1, 0.3, and 0.7% w/w%) retinol.

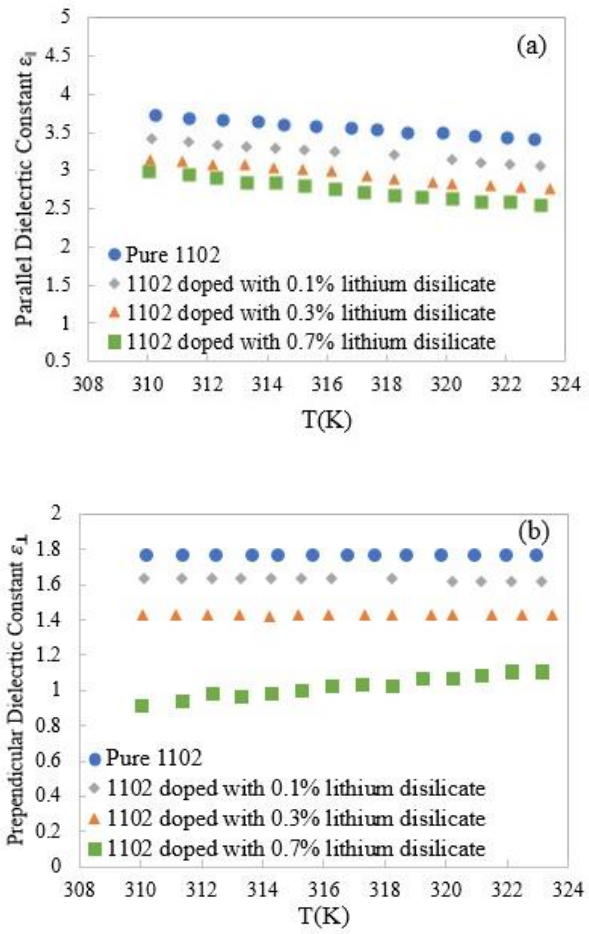


Fig. **5** Temperature monitoring of parallel $\varepsilon_{\parallel}$ (a) and perpendicular $\varepsilon_{\perp}$ (b) dielectric constants of pure and doped 1102 with (0.1, 0.3, and 0.7% w/w%) lithium disilicate.

This reduction is observed to correlate positively with the increasing concentration of the dopant. It is important to note that the orientation of molecules within the liquid crystal matrix and the polarity of molecules are critical factors influencing the dielectric behavior.

Any perturbation in these parameters is likely to result in diminished dielectric coefficients. Consequently, the observed decline in the dielectric coefficients of the lithium disilicate-doped liquid crystal can be attributed to the disruption of intramolecular order and the alteration of intermolecular interactions among the liquid crystal molecules (NLC-NLC), which aligns with theoretical expectations.

It should be noted that, in NP-NLC systems, there are three types of interactions that take place: (I) NLC-to-NLC interaction, (II) NLC-NP interaction, and (III) NPs-NP interaction. Only interactions between NLC molecules occurred in pure NLC [18], [19].

## IV. Conclusion

This study examined how the shape and concentration of nano dopants influence the photonic and dielectric characteristics of nematic liquid crystals (NLC) which function as simulators for cell walls. Our findings indicate that the incorporation of soluble Retinol into the NLC significantly enhances the order parameter of the NLC-dopants mixture at specific concentrations, leading to an increase in both the parallel ($\varepsilon_{\parallel}$) and perpendicular ($\varepsilon_{\perp}$) dielectric coefficients. The extent of this enhancement is directly related to the concentration of the soluble NPs. Conversely, the introduction of insoluble Lithium Disilicate NPs results in a reduction of the order parameter and dielectric constants of the NLC-NPs mixture, attributed to the geometric configuration of the NPs.

The findings of this study indicate that the dielectric characteristics of the environment used to simulate cell walls can be altered by fine-tuning the concentration and morphology of nanoparticles. Furthermore, given the analogous anisotropic behavior observed in both liquid crystals and cell walls, it can be inferred that the properties of the cell wall may be modulated and predicted by the integration of specific nanoparticles, which differ in their concentration and structural form.

## References

**[1]** Kieran J.D. Lee, Susan E. Marcus, and J. Paul Knox, “Cell Wall Biology: Perspectives from Cell Wall Imaging,” Molecular Plant, Vol. 4, pp. 212-219, 2011.

**[2]** Yang NJ and Hinner MJ. “Getting across the cell membrane: an overview for small molecules, peptides, and proteins,” Methods Mol Biol. Vol. 1266, pp. 29-53, 2015.

**[3]** Zachowski A. “Phospholipids in animal eukaryotic membranes: transverse asymmetry and movement,” Biochem J. Vol. 294, pp.1–14, 1993.

**[4]** Kansy M, Senner F, and Gubernator K. “Physicochemical high throughput screening: parallel artificial membrane permeation assay in the description of passive absorption processes,” J Med Chem. Vol. 4, pp. 1007–1010, 1998.

**[5]** Johannes L and Römer W. Shiga toxins “from cell biology to biomedical applications,” Nat Rev Microbiol. Vol. 8, pp.105–116, 2010.

**[6]** Baskin Tobias I. "Anisotropic expansion of the plant cell wall," Annu. Rev. Cell Dev. Biol. Vol, 21, pp. 203-222, 2005.

**[7]** Landrein, Benoît, and Olivier Hamant. "How mechanical stress controls microtubule behavior and morphogenesis in plants: history, experiments and revisited theories," The Plant Journal, Vol. 75, pp. 324-338, 2013.

**[8]** M.C. Jarvis and M.C. McCann, "Macromolecular biophysics of the plant cell wall: concepts and methodology," Plant Physiology and Biochemistry, Vol. 38, pp. 1-13, 2000.

**[9]** Voxeur A. and Herman H. "Cell wall integrity signaling in plants: To grow or not to grow that's the question,” Glycobiology, Vol. 26, pp. 950-960, 2016.

**[10]** Liu, Ke, Zhimao Yang, and Hitoshi Takagi. "Anisotropic thermal conductivity of unidirectional natural abaca fiber composites as a function of lumen and cell wall structure," Composite structures, Vol. 108, pp. 987-991.

**[11]** Gkolemis K., E. Giannoutsou, ID S. Adamakis, B. Galatis, and P. Apostolakos. "Cell wall anisotropy plays a key role in Zea mays stomatal complex movement: the possible role of the cell wall matrix," Plant Molecular Biology, Vol. 113, pp. 331-351, 2023.

**[12]** Sendra Marta, P. M. Yeste, Ignacio Moreno-Garrido, José Manuel Gatica, and Julián Blasco, "CeO2 NPs, toxic or protective to phytoplankton? Charge of nanoparticles and cell wall as factors which cause changes in cell complexity," Science of The Total Environment, Vol. 590, pp. 304-315, 2017.

**[13]** Milewska-Hendel A. Katarzyna S. Weronika G. and Ewa Kurczyńska, "Gold nanoparticles-induced modifications in cell wall composition in barley roots," Cells, Vol. 10, pp. 1965, 2021.

**[14]** Cui Jianghu, Yadong Li, Qian Jin, and Fangbai Li. "Silica nanoparticles inhibit arsenic uptake into rice suspension cells via improving pectin synthesis and the mechanical force of the cell wall," Environmental Science: Nano Vol. 7, pp. 162-171, 2020.

**[15]** Das Debabrata, and Giasuddin Ahmed. "Silver nanoparticles damage yeast cell wall," J. Biotechnol, Vol. 3, pp. 36-39, 2012.

**[16]** Stephen, Michael J. and Joseph P. Straley. "Physics of liquid crystals," Reviews of Modern Physics, Vol. 46, pp. 617, 1974.

**[17]** R. Kian, M.S. Zakerhamidi, A. Ranjkesh, A.N. Shamkhali, B. Taheri, S.K. Varshney, and T.H. Yoon, "Investigation of the spectroscopic features along with the media polarity effect in some symmetrical disc-shaped liquid crystals," J. Mol. Liq, Vol. 309, pp. 13226, 2020.

**[18]** A. Ranjkesh, N. Ebrihimpour, M. S. Zakerhamidi, and S. M. Seyedahmadian. "Temperature-dependent dielectric property of a nematic liquid crystal doped with two differently–shaped tungsten oxide (W18O49) nanostructures," Journal of Molecular Liquids Vol. 348, pp. 118024, 2022.

**[19]** M. S. Zakerhamidi , S. Shoarinejad, and S. Mohammad pour. "$Fe_3O_4$ nanoparticle effect on dielectric and ordering behavior of nematic liquid crystal host," Journal of Molecular Liquids, Vol. 191, pp. 16-19, 2014.

**[20]** Sadigh M. Khadem, M. S. Zakerhamidi, and A. Ranjkesh, "Enhanced electro-optical nonlinear responses of doped nematic liquid crystals: Towards optoelectronic devices," Optics and Lasers in Engineering, Vol. 159, pp. 107229, 2022.

**[21]** Osipov Mikhail A. and Maxim V. Gorkunov, "Nematic liquid crystals doped with nanoparticles: Phase behavior and dielectric properties," In Liquid Crystals with Nano and Microparticles, vol. 2, pp. 135-175. 2017.

**[22]** Tyagi Yogeshvar, "Liquid crystals: An approach to different state of matter," The Pharma Innovation, Vol. 7, Part H, pp. 540, 2018.

**[23]** Burrows N. D., Ariane M. Vartanian, Nardine S. Abadeer, Elissa M. Grzincic, Lisa M. Jacob, Wayne Lin, Ji Li, Jordan M. Dennison, Joshua G. Hinman, and Catherine J. Murphy. "Anisotropic nanoparticles and anisotropic surface chemistry," The journal of physical chemistry letters, Vol. 7, pp. 632-641, 2016.

**[24]** O. Denisova and Y. Abramishvili, "Liquid crystal cell as a model of a biological system: biosensor," E3S Web Conf, International Scientific Conference Ecological and Biological Well-Being of Flora and Fauna. Vol. 420, pp. 09005, 2023.

**[25]** Yves Bouligand, "Liquid crystals and biological morphogenesis: Ancient and new questions," Comptes Rendus Chimie, Vol. 11, pp. 281-296, 2008.

**[26]** H. Tajalli, A. Ghanadzadeh Gilani, M.S. Zakerhamidi, M. Moghadam, "Effects of surfactants on the molecular aggregation of rhodamine dyes in aqueous solutions," Spectrochimica Acta Part A: Molecular and Biomolecular Spectroscopy, Vol. 72, pp. 697-702, 2009.

**[27]** Nechipurenko Yu , Ryabokon, VF , Semenov Sergei , and Evdokimov YM. "Thermodynamic models describing the formation of "bridges" between, molecules of nucleic acids in liquid crystals, " Biofizika. Vol. 48. pp. 635-643, 2003.

**THIS PAGE IS INTENTIONALLY LEFT BLANK.**

IJBBE International Journal of Biophotonics & Biomedical Engineering Vol. 4, No. 2, Fall - Winter, 2024

Research Article

# Design of Metal- Insulator- Metal Plasmonic Waveguide Biosensor for Disease Diagnosis

**M. Sharifi[a], M. Purasl[a], and H. Tajalli[a]**

*a Biophotonic Research Centre, Tabriz Branch Islamic Azad University, Tabriz, Iran*

***Corresponding Author Email: m_sharifi66@yahoo.com**

**DOI: 10.71498/ijbbe.2024.1191244**

**ABSTRACT**

Received: Nov. 22, 2024, Revised: Feb. 25, 2025, Accepted: Feb. 26, 2025, Available Online: Mar. 18, 2025

*A plasmonic metal-insulator-metal (MIM) biosensor exploits the optical properties of surface plasmon resonances (SPRs) to achieve high sensitivity and specificity in biomolecule detection. The MIM structure in this study features a narrow waveguide as the insulator layer, flanked by elliptical arrays of solid metallic ovals surrounded by thin air layers. These arrays generate localized surface plasmon polaritons (LSPPs), which enhance light-matter interaction. The system operates through dual plasmonic resonances, specifically Fano resonances, resulting in a distinct transmission spectrum. Fano resonances, arising from the interference between narrow and broad resonances, produce sharp asymmetric transmission profiles that are highly sensitive to refractive index changes in surrounding biomolecules. Numerical simulations using the finite element method (FEM) confirm the sensor's ability to detect minor refractive index shifts, making it highly responsive to small biological variations. The simulation results indicate that the proposed design achieves a sensitivity of approximately 20–50 picometers for a refractive index change as small as $\Delta n=10^{-6}$. This MIM biosensor shows significant potential in applications such as point-of-care diagnostics and environmental monitoring. It can detect a wide range of biomolecules, including proteins, DNA, and pathogens, with high precision, enabling early disease detection and real-time monitoring of environmental contaminants. The enhanced sensitivity provided by Fano resonances positions this technology as a promising tool for personalized medicine, public health, and safety applications.*

**KEYWORDS**

*Biosensor, Fano Resonance, FEM, MIM waveguide.*

## I. INTRODUCTION

Surface plasmon polaritons (SPPs) are electromagnetic waves that propagate along the interface between a metal and a dielectric, arising from the coupling of surface plasmons within the metal and electromagnetic waves in the dielectric (1). This interaction leads to highly confined electromagnetic fields near the surface, which can be harnessed for various applications. Extensive research on SPP-based structures has demonstrated their potential in a wide range of fields, including biosensing (2), chemical sensing (3), metamaterials (4), plasmonic nanostructures (5), and optical communication (6). Their popularity is attributed to several key advantages: the ability to miniaturize devices, rapid response times, high sensitivity to changes in the surrounding refractive index (RI), and improved light-matter interaction (7). When new sensing

materials are introduced to an SPP-based system, the effective RI shifts, causing a corresponding wavelength shift, which allows for the calculation of sensor sensitivity.

Numerous SPP-based sensors have been proposed, offering enhanced detection capabilities and reliability (8-10). Recently, Metal-Insulator-Metal (MIM) plasmonic sensors based on SPPs have gained significant attention. MIM waveguides are particularly noteworthy due to their ability to confine light at subwavelength scales, enabling nanoscale optical information transmission with high field intensities and low fabrication costs (11, 12). These properties make MIM structures ideal for applications where compact size and enhanced light interaction are crucial, such as in biosensing and optical communication.

One area of increasing interest in MIM optical biosensors is the excitation of Fano resonances (13). Fano resonances, a quantum mechanical phenomenon resulting from the interference between a discrete quantum state and a continuum of states, have unique optical properties that can be harnessed for advanced device functionalities (14). The resulting sharp asymmetric line shapes in the absorption or transmission spectra are highly sensitive to changes in the surrounding environment. Small perturbations in the medium can lead to significant shifts in the resonance position, width, and amplitude. This high sensitivity makes Fano resonances ideal for a variety of sensing applications, particularly in detecting minute changes in biological or chemical environments (15). The incorporation of Fano resonances in MIM waveguides offers exciting opportunities for the development of advanced optical devices, particularly in fields requiring precision sensing and environmental monitoring.

In this study, we propose a novel non-through Metal-Insulator-Metal (MIM) waveguide structure designed to excite Fano resonances. The configuration consists of a bus waveguide flanked by two chain resonators, each containing eight ring-shaped cavities. This arrangement enables strong light-matter interactions and the excitation of Fano resonances within the system. To thoroughly investigate the underlying mechanisms of Fano resonance formation, we employed the finite element method (FEM) method for numerical analysis. Additionally, we explored the sensitivity of the Fano resonance to changes in the refractive index (RI) of the surrounding medium, providing insight into its potential application for high-sensitivity biosensing and environmental monitoring. The results demonstrate that the proposed MIM waveguide can be an effective platform for developing advanced optical sensors based on the detection of RI-induced shifts in Fano resonance characteristics. Several plasmonic biosensors based on surface plasmon resonance (SPR) and localized surface plasmon resonance (LSPR) have been developed in recent years, achieving sensitivities typically ranging from 100 nm/RIU to 1000 nm/RIU depending on the design and materials used (17,18) For instance, prism-based SPR sensors offer high sensitivity but often require bulky optical setups, limiting their use in point-of-care applications (19). Similarly, nanoparticle-based LSPR sensors provide nanoscale detection but may suffer from lower specificity due to broad resonance profiles (20). In contrast, the proposed MIM waveguide biosensor leverages Fano resonances to produce sharp, asymmetric transmission peaks, achieving a sensitivity on the order of tens of picometers for a refractive index change as small as $\Delta n=10^{-6}$. This represents a significant improvement in detecting subtle biomolecular changes compared to conventional SPR and LSPR sensors while maintaining a compact design suitable for integration into miniaturized diagnostic platforms.

## II. DESIGN AND NUMERICAL METHOD

Figure 1 presents a two-dimensional schematic of the proposed coupling system, which comprises a Metal-Insulator-Metal (MIM) waveguide flanked by two chain resonators, each containing eight elliptical rings, all sandwiched around a central waveguide. In the figure, the blue regions represent silver (Ag), while the gray areas correspond to air, which

serves as the insulating medium. The width of the MIM waveguide is set to $w_1$=70 nm, ensuring efficient light confinement and propagation. The coupling distance between the MIM waveguide and the ring resonators is g =10 nm, which optimizes energy transfer between the waveguide and resonators, allowing for the excitation of Fano resonances.

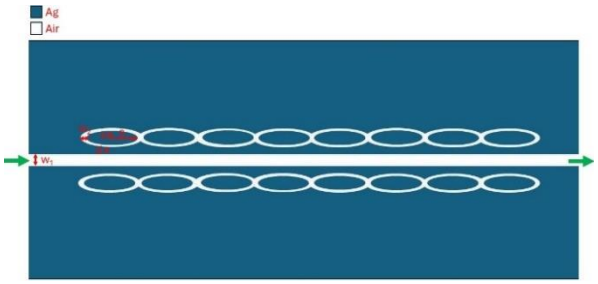


Fig. **1**: Schematic of the proposed coupling system featuring a Metal-Insulator-Metal (MIM) waveguide flanked by two chains of resonators, each consisting of eight elliptical rings surrounding a central waveguide.

For the elliptical ring resonators, the air shell surrounding each ellipse has a thickness of $w_2$=35nm, providing additional confinement of the localized surface plasmon polaritons (LSPPs). Each ellipse has a semi-major axis of a=100 nm and a semi-minor axis of b=50 nm, creating a tailored geometry that further enhances light-matter interactions. The refractive index of the medium filling the waveguide is n=1.35, chosen to mimic biological or chemical sensing environments. These parameters were carefully selected to maximize the sensitivity of the system to changes in the refractive index, facilitating the study of Fano resonance behavior in the proposed design.

In the computational analysis, silver (Ag) was selected as the metal material due to its favorable plasmonic properties. The relative permittivity of Ag is modeled using the Debye–Drude dispersion model, which accurately captures the frequency-dependent behavior of metals at optical frequencies. The permittivity of Ag is given by the following equation (2):

$$\varepsilon(\omega) = \varepsilon_\infty + \frac{\varepsilon_g - \varepsilon_\infty}{1 + i\omega\tau} + \frac{\sigma}{i\omega\varepsilon_0} \quad (1)$$

In Equation (1), $\varepsilon_\infty = 3.8344$ represents the permittivity at infinite frequency, while $\varepsilon_s = -9530.5$ is the static permittivity, indicating the low-frequency response of the metal. The term $\tau = 7.35 \times 10^{-15}\, s$ refers to the relaxation time, which accounts for electron scattering effects in the material, and $\sigma = 1.1486 \times 10^7 S/m$ is the electrical conductivity of silver. This model provides a comprehensive description of Ag's optical properties across a broad range of frequencies. Given the MIM waveguide structure, only the fundamental transverse magnetic mode ($TM_0$) is supported and transmitted. As this mode is characterized by a magnetic field perpendicular to the propagation direction and the electric field confined near the metal-dielectric interface, it plays a crucial role in enabling surface plasmon polariton (SPP) excitation. Therefore, the analysis of the TM transmission mode is essential for understanding the behavior of light propagation within the MIM waveguide and optimizing the system's sensitivity to refractive index variations.

In our simulation, we numerically analyzed the spectral response of the designed MIM structure using the two-dimensional model based on FEM within the COMSOL Multiphysics platform. The lateral dimensions of the structure were set to 1.2 × 2 μm to balance both the physical relevance of the model and computational efficiency. To achieve accurate results without excessive time costs, we focused exclusively on a 2D model. This approach allows us to capture the essential behavior of the system while optimizing the trade-off between computational accuracy and resource consumption.

To ensure precise and reliable simulations, we employed perfectly matched layer (PML) boundary conditions, which minimize reflections at the edges of the computational domain, effectively simulating an open system. A user-controlled mesh grid was implemented to optimize the balance between calculation speed and accuracy, specifically refining the mesh in areas of critical interest, such as the waveguide and resonator regions. This targeted meshing ensures that the key features of the

MIM structure are accurately resolved while maintaining computational efficiency.

The light source, generating a TM-polarized wave, was introduced at the left side of the waveguide (indicated by the green arrow) by placing an active port at the input of the simulation domain. TM polarization is essential for the excitation of surface plasmon polaritons (SPPs), which are then confined and transmitted through the MIM waveguide. To measure the transmission response, a detector was positioned at the right side of the waveguide by placing an output port. The transmission spectrum was subsequently analyzed by tracking the light propagation from the input to the output port, providing insights into the resonant behavior of the system. This setup allows us to evaluate how effectively the structure supports the excitation and transmission of SPPs and their impact on the resulting spectral properties. While the proposed MIM waveguide biosensor demonstrates promising performance in simulations, its practical implementation involves several fabrication challenges that warrant consideration. The precise construction of the elliptical ring resonators, with dimensions such as a semi-major axis of 100 nm and a semi-minor axis of 50 nm, requires advanced nanofabrication techniques, such as electron-beam lithography or focused ion beam milling, to ensure geometric accuracy. Additionally, achieving a uniform coupling distance of g=10 nm between the waveguide and resonators demands high precision to maintain consistent energy transfer and resonance characteristics. The integration of silver (Ag) as the plasmonic material may also pose challenges due to its susceptibility to oxidation, potentially necessitating protective coatings or alternative materials like gold (Au) in real-world applications. Addressing these fabrication hurdles through optimized processes and material selection will be critical to translating this design from a simulation to a functional device.

## III. RESULTS AND DISCUSSION

As shown in Figure 2, the transmission spectrum displays two prominent asymmetrical peaks at wavelengths λ=1110 nm and λ=1464 nm, which are recognized as Fano resonances. These sharp, asymmetric peaks result from the interference between a narrow discrete resonance and a broader spectral continuum, a hallmark of Fano resonance. To explore how variations in the refractive index (RI) affect the transmission properties of the proposed MIM waveguide structure, simulations were performed by replacing the air inside the waveguide with a biomaterial medium having a refractive index of n=1.35. Figure 2 compares the transmission spectra for air (represented by the red solid line) and for the biomaterial (represented by the blue solid line).

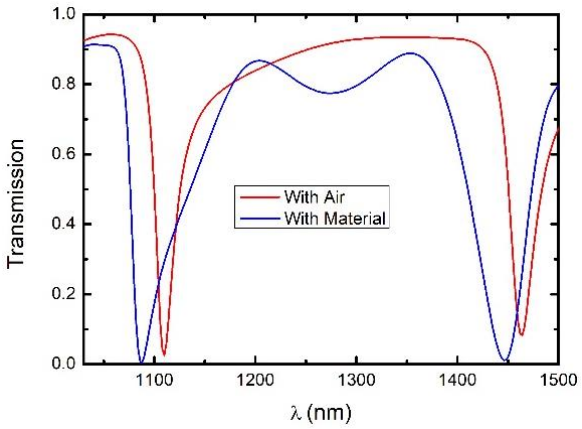


Fig. **2**: Transmission spectra of the proposed MIM waveguide structure: red line for air-filled and blue line for biomaterial-filled. The shift in resonance wavelengths due to refractive index changes demonstrates the system's sensitivity and highlights the distinct Fano resonance peaks.

The results reveal a significant wavelength shift in the Fano resonance peaks as the refractive index increases from 1.0 (air) to 1.35 (biomaterial). This shift underscores the system's high sensitivity to changes in the RI, as even a small change in the refractive index leads to a substantial displacement in the transmission spectrum. The sensitivity observed is on the order of tens of picometers for a $\Delta n=10^{-6}$ change in refractive index, indicating that the MIM waveguide can detect extremely small variations in the biomaterial's RI. This exceptional sensitivity positions the

MIM waveguide system as a powerful tool for biosensing applications, where detecting subtle changes in RI—caused by the presence of biomolecules—is critical for early and precise detection. Such capabilities are crucial for developing advanced biosensors aimed at real-time, accurate monitoring of biological interactions or disease markers. To assess the biosensor's specificity for disease diagnosis, its response to biologically relevant analytes was further explored. The refractive index of n=1.35 used in the simulations mimics the typical RI range of biological media, such as aqueous solutions containing proteins (e.g., bovine serum albumin, RI ≈ 1.33–1.36) or DNA strands (RI ≈ 1.34–1.37) (21). The observed wavelength shifts in the Fano resonance peaks (e.g., from λ=1110 nm to higher wavelengths with Δn=0.35) suggest that the sensor can effectively distinguish between subtle RI variations caused by the binding of specific biomolecules. For instance, the detection of pathogens, such as viruses with RI differences on the order of $10^{-3}$ to $10^{-6}$ due to surface protein interactions, could be achieved with high precision. This specificity arises from the sharp Fano resonance profiles, which minimize overlap between adjacent resonance peaks and enhance the sensor's ability to resolve distinct biomolecular signatures. These findings indicate that the proposed MIM biosensor could be tailored for targeted detection of disease markers, such as cancer-related proteins or viral DNA, supporting its potential in personalized diagnostics.

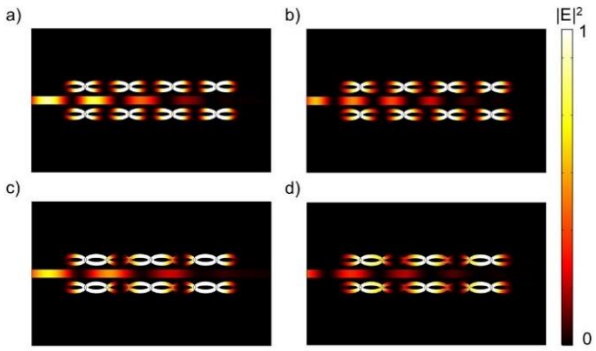


Fig. **3**: Qualitative illustration of the normalized electric field intensity distribution for the first resonance at λ=1110nm, shown for (a) air and (b) biomaterial. Similarly, the electric field distribution for the second resonance at λ=1464nm is presented in (c) and (d), for air and biomaterial, respectively.

Figure 3 qualitatively illustrates the normalized electric field intensity distribution for each of the resonances, highlighting the critical role played by the elliptical resonators in generating Fano resonances. These elliptical resonators enhance the interaction between the localized surface plasmon polaritons (LSPPs) and the incident light, which is essential for the excitation of the Fano resonances.

In Figures 3(a) and 3(b), the field distribution for the first resonance at λ=1110 nm is shown for both air and biomaterial, respectively. The field intensity is concentrated around the elliptical resonators, demonstrating their role in confining and localizing the electromagnetic energy, which leads to the asymmetric Fano resonance profile. Similarly, Figures 3(c) and 3(d) depict the electric field distribution for the second resonance at λ=1464 nm. Here too, the elliptical resonators act as key elements in modulating the light-matter interaction. The intensity distribution in these figures reveals the wavelength-dependent behavior of the system. The shift in field localization between air and biomaterial further demonstrates the system's sensitivity to refractive index changes, with the resonance characteristics adjusting in response to the surrounding medium.

## IV. Conclusion

In conclusion, we have demonstrated that two distinct asymmetric Fano resonances can be generated in the transmission spectra of a plasmonic system consisting of a Metal-Insulator-Metal (MIM) waveguide integrated with dual chains of elliptical ring resonators. These resonators, positioned symmetrically on either side of the waveguide, play a crucial role in inducing Fano resonances through the coherent coupling and interference between continuous (broadband) and discrete (narrowband) modes within the system. This interference results in the characteristic sharp, asymmetric spectral profiles associated with Fano resonances, which are highly sensitive to changes in the surrounding refractive index (RI). The simulation results confirm that the proposed biosensor design can achieve a sensitivity on the order of tens of picometers for

a refractive index change as small as $\Delta n=10^{-6}$. This level of sensitivity positions the sensor as a promising candidate for detecting biomolecules or other analytes in fields such as medical diagnostics, environmental monitoring, and chemical analysis. The combination of the MIM waveguide and elliptical ring resonators offers a highly effective platform for plasmonic sensing, capable of providing real-time, accurate detection of molecular interactions with excellent precision. Addressing fabrication challenges and optimizing biomolecular specificity will further enhance the practical utility of this biosensor for real-world applications. Future work will focus on experimental validation of the proposed design to confirm its simulated performance and address any unforeseen practical challenges.

## REFERENCES

[1] Zhang J, Zhang L, and Xu W. "Surface plasmon polaritons: physics and applications," Journal of Physics D: Applied Physics. vol.45, pp.113001, 2012.

[2] Sharifi M, PASHAEI AH, Tajalli H, and Bahrampour A. "Design of surface plasmon resonance biosensor with one dimensional photonic crystal for detection of cancer," 2016.

[3] Martínez J, Ródenas A, Aguiló M, Fernandez T, Solis J, and Díaz F. "Mid-infrared surface plasmon polariton chemical sensing on fiber-coupled ITO coated glass," Optics Letters. vol. 41, pp. 2493-2496, 2016.

[4] Gric T and Rafailov E. "Propagation of surface plasmon polaritons at the interface of metal-free metamaterial with anisotropic semiconductor inclusions," Optik. vol. 254, pp.168678, 2022.

[5] Bai Y, Li Y, Ikram M, Ren Y, Xu Y, Wang Y, et al. "Circular dichroism induced by the coupling between surface plasmon polaritons and localized surface plasmon resonances in a double-layer complementary nanostructure," The Journal of Physical Chemistry C. vol. 126, pp. 10159-10166, 2022.

[6] Zhang HC, Zhang LP, He PH, Xu J, Qian C, Garcia-Vidal FJ, et al. "A plasmonic route for the integrated wireless communication of subdiffraction-limited signals," Light: Science & Applications. vol. 9, pp.113, 2020.

[7] Schröder B. Probing Light-Matter Interactions in Plasmonic Nanotips: Dissertation, Göttingen, Georg-August Universität, 2020.

[8] Joseph S, Sarkar S, and Joseph J. "Grating-coupled surface plasmon-polariton sensing at a flat metal–analyte interface in a hybrid-configuration. ACS Applied Materials & Interfaces," vol.12, pp. 46519-46529, 2020.

[9] Kumari S, Verma YK, and Tripathi SM. "Plasmonic Ring Resonator Sensor with High Figure of Merit and Sensitivity Using Degenerate N-Doped Silicon for SPP Excitation," Plasmonics. pp.1-9, 2024.

[10] Aminah NS, Lertvanithphol T, Sathukarn A, Horprathum M, Alatas H, Fauzia V, et al. Fabrication of Au coated sinusoidal grating substrates as SPP-SERS sensor chip for trace-level detection of explosive. Optical Materials. 2024;149:114952.

[11] Chen H, Yan S, Cao Y, Jiang W, Yan X, Wang C, et al. "Nanoscale temperature sensors based on MIM waveguide coupling and ring-embedded nanostructures," Frontiers in Physics.vol.12, pp.1456177, 2024.

[12] Lu H, Wang G, and Liu X. "Manipulation of light in MIM plasmonic waveguide systems," Chinese Science Bulletin. vol. 58, pp. 3607-3616, 2013.

[13] Chen J, Li J, Liu X, Rohimah S, and Tian H, "Qi D. Fano resonance in a MIM waveguide with double symmetric rectangular stubs and its sensing characteristics," Optics communications.vol. 482, pp. 126563, 2021.

[14] Sharifi M, Rezaei B, Pashaei Adl H, and Zakerhamidi MS. "Tunable Fano resonance in coupled topological one-dimensional photonic crystal heterostructure and defective photonic crystal," Journal of Applied Physics. Vol. 133, 2023.

[15] Adhikari R, Chauhan D, Mola GT, and Dwivedi RP. "A review of the current state-of-the-art in Fano resonance-based plasmonic metal-insulator-metal waveguides for sensing applications," Opto-Electronics Review. vol. 29, 2021.

[16] Gai H, Wang J, and Tian Q. "Modified Debye model parameters of metals applicable for broadband calculations," Applied optics.vol. 46, pp. 2229-2233, 2007.

[17] Sekhwama M, Mpofu K, Sivarasu S, and Mthunzi-Kufa P. "Enhancing limit of detection in surface plasmon resonance biosensors: A sensitivity analysis for optimal performance," InOptical Interactions with Tissue and Cells XXXV, Vol. 12840, pp. 79-85, 2024.

[18] Cynthia S, Ahmed R, Islam S, Ali K, and Hossain M. "Graphene based hyperbolic metamaterial for tunable mid-infrared biosensing. RSC advances," vol.11, pp. 7938-7945, 2021.

[19] Puiu M and Bala C. "SPR and SPR imaging: recent trends in developing nanodevices for detection and real-time monitoring of biomolecular events," Sensors. vol. 16, pp. 870, 2016.

[20] Smith NS, Abhari S, Smith LS, Altman KM, Yakkanti MR, and Malkani AL. "Results of Primary Total Knee Arthroplasty in Patients on Chronic Psychotropic Medications," The Journal of Arthroplasty. vol. 39, pp. S161-S166, 2024.

**THIS PAGE IS INTENTIONALLY LEFT BLANK.**

.

IJBBE International Journal of Biophotonics & Biomedical Engineering Vol. 4, No. 2, Fall - Winter, 2024

Research Article

# On Translation of Sonar Stimulation to Proper Visual Representation Using a Photometrically Precise Method of Audible Waves Transformation

**S. M. M. Mousavi [a], and S. Mohajer Mazandarani [a & *]**

*a Biophotonics Laboratory, Department of Physics, Kharazmi University, Karaj, Iran*

***Corresponding Author Email: mohajer@khu.ac.ir**

**DOI: 10.71498/ijbbe.2024.1190972**

**ABSTRACT**

Received: Nov. 19, 2024, Revised: Feb. 11, 2025, Accepted: Feb. 26, 2025, Available Online: Mar. 18, 2025

*This research aims to assign time spectrum and color frame visual representations to acoustic data of audible range. The method of color generation is to assign visible spectrum frequency $\nu$, to the audible frequency $f$ resulted from a transformation, defined as the main mapping function $T(f)$. The viability of $T(f)$ is ensured by satisfying four main criteria imposed by human sonar and visual perception. Afterward, a second function is proposed to represent color expressed by the output of $T(f)$ inside sRGB color space. This second function is defined as the rendering function and is obtained by the development of a matrix transformation acting on normalized human tristimulus values to yield sRGB values. Finally, the result is extended to properly translate a sound clip into color frames, changing in response to changes inside the sound clip. Such an algorithm for processing sound enables a person the deduct sounds from different sources through color vision with reasonable quality of details. The main application of such translation of sounds is to aid the Auditory Impaired. The other applications of such a method include simulating a certain type of Synesthesia and determining the cause of seismic waves by the color resulting from its visualization by this method.*

**KEYWORD**

*Auditory Impaired, Audible Sound, Transformation, Visible Spectrum, Visualization*

## I. INTRODUCTION

The plot of normal hearing threshold versus frequency, which also includes thresholds of discomfort and pain, is shown in Fig. **1**. A person with a hearing threshold higher than the blue curve specified in Fig. **1** on any audible frequency domain, is diagnosed with the condition of Hearing Loss [1], [2].

Regardless of the cause of the condition, Hearing Loss has been categorized into seven subclasses, called types, which are classified by the average degree to which a person is incapable of hearing sound of low volumes over all frequencies [2]. Earlier classifications stated that Hearing Loss may be mild, moderate, severe, or profound [1], while current thresholds are presented in Table **1**. Hearing Loss can affect one or both ears and leads to difficulty in hearing conventional speech or soft sounds [2].

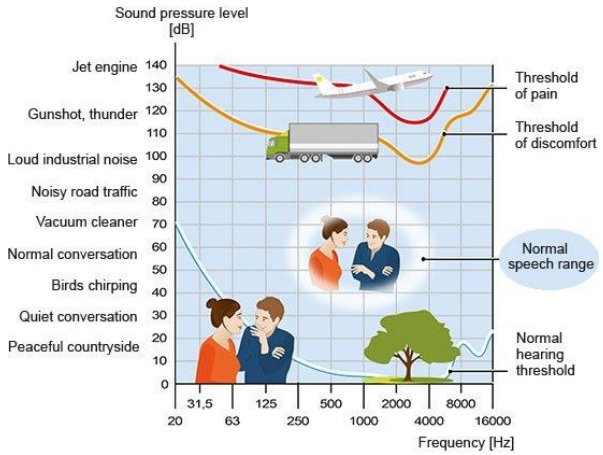


Fig. **1** Average person's thresholds of hearing, discomfort, and pain, are shown by blue, orange, and red curves respectively; the volume and frequency range of some common phenomena is also shown [1], [3]

TABLE **1** THRESHOLD AND NOTICEABILITY OF EACH TYPE OF HEARING LOSS (CLASSIFIED BY SEVERITY); THE THRESHOLDS ARE AVERAGE HEARING THRESHOLDS OF ONLY 0.5, 1, 2, AND 4 KHZ [2], [4], [5]

| Type/Category (by Severity) | Threshold Range (dB) | Noticeability (Effect on Daily Life) |
|---|---|---|
| Unilateral | <20 in the better ear<br>>35 in the worst ear | Unnoticeable, Difficulty only when the sound source is close to the worst ear |
| Mild | 20 – 34.9 | Nearly Unnoticeable |
| Moderate | 35 – 49.9 | Difficulty in Quiet Conversations |
| Moderately Severe | 50 – 64.9 | Difficulty in Medium Conversations |
| Severe | 65 – 79.9 | In Need of Hearing Aid |
| Profound | 80 – 94.9 | Hearing Only Loud Indicatory Sounds |
| Complete/Total/Full | >95 | Unable to Handle Everyday Life |

The last three types of Table **1** are named Severe, Profound, and Complete Types, which together are referred to as Disabling Hearing Loss [1] or Severe-to-Profound-Hearing-Loss [6], [7] or simply STPHL [7]; and in this research, people diagnosed with STPHL will be referred to as the Auditory Impaired.

### A. *Importance*

Since hearing is one of the most crucial senses of humans, as it imparts tremendous survival advantages and is of great help in indicating the happenstance of something without the need for it to be in any focus [8], therefore, as also specified in Table **1**, the Auditory Impaired are unable to handle aspects of daily life in which hearing is crucial [9]. Therefore challenges arise for the Auditory Impaired in everyday activities including crossing the streets, learning to read and communicate [10]—if the condition of Hearing Loss existed before learning starts—responding to auditory stimulation outside of focused attention—that is responding to others when they are called upon or feeling the presence of indicatory sounds. Also, unaddressed Hearing Loss and especially STPHL can lead to reduced quality of life (QoL), isolation, dependence, lack of energy, frustration, and even depression [11], [12], [13], [14]. All these challenges may arise for the Auditory Impaired if they are not provided with proper treatment or aid (be the aid of a human, a hearing aid device, etc.) [7]. People with profound Hearing Loss, which implies the existence of very little or no hearing, often use sign language to communicate [10], which therefore implies there is no widespread or useful aid designed for them, to be able to communicate in a manner that could also be conventional for people

capable of proper hearing [1], [15]. This will be discussed in detail in I.B.

STPHL also, is gradually becoming a more common phenomenon in society [6]. Multiple studies on the prevalence and YLD[1] of Hearing Loss have confirmed that both measures are increasing. Reference [16] shows in a clinical database of 32,781 cases, 6.7% of the local clinical population[2] and 0.7% of the general population of the UK, were identified with STPHL by the year 2012; the estimations are certainly higher due to unsafe listening practices [1], [7]. Also, among those older than 60 years, over 25% are affected by STPHL [9], [17]. Reference [7], also, shows by collecting a database containing over 15 million audiograms obtained from regions covering more than 99% of the Swedish population, that 0.28% of the Swedish population are diagnosed by STPHL by the year 2022. The study also declares the global prevalence of STPHL is currently increasing; though another study [18] on a nationwide population-based database from Korean National Health Insurance Service on the South Korean population shows a decreasing percentage in the prevalence of Hearing Loss from 2006 to 2015 after the peak of 0.25 million cases—amounting to 0.5% of South Korean population—in 2010. The most recent study [17] on global Hearing Loss, which investigates the prevalence and YLD rates from the year 1990 until 2019, shows global prevalence and YLD rates are both increasing, with the total number of people identified with STPHL having a 79.1% increase from 225.3 million in 1990 to 403.3 million in 2019. The study also forecasts the number of people diagnosed with Hearing Loss to be 2.45 billion by 2050, amounting to 1 in 10 people alive in 2050 [1]. One of the main causes of this recent growth is unpracticed listening, and preference for buying higher power, and louder audio-playing devices such as party boxes and car audio systems; These cases and other causes shall be discussed in detail in another paper.

### B. *Related Works*

First, it shall be stated that STPHL can be divided into purely sensorineural Hearing Loss (SNHL), where the origin of the Hearing Loss can be found in the cochlea or the vestibulocochlear nerve, and mixed Hearing Loss (MHL), which is a combination of SNHL and conductive Hearing Loss caused by damage to the outer and/or middle ear [11]. Because there are more than 300 congenital syndromes related to hearing loss [6], the differential diagnosis for hearing loss is very broad; therefore various methods are used by professionals for the treatment of Hearing Loss. We first discuss conventional methods.

*1) Conventional Medical Treatments*

The two major causes of conductive Hearing Loss are Otosclerosis, being abnormal bone remodeling in the middle ear [19] and Cholesteatoma, an abnormal collection of skin cells inside the middle ear, which creates benign tumors [20]. These two conditions and other causes of conductive Hearing Loss are usually treated by Surgery, which although widely available, is often hardly affordable[3] [6], [21], [22], [23]. The option is widely available for different types of purely conductive Hearing Loss and it can restore normal hearing in a satisfying number of cases [11], but still, there are limitations as to the cost and effectivity of the procedure—e.g. when the Hearing Loss is not purely result from structural damage and is also partly due to sensorineural causes [11].

For the cases dealing with SNHL, there is a type of implant called a cochlear implant which allows the reception of an 8-channel digital sound, which is hard to understand by an average person [24], and the person will need rehabilitation procedure after the surgery [14], [25], to be trained to recognize everyday sounds

[1] Years Lived with Disability

[2] Clinical Population of a certain medical condition refers to the population of all the people identified by all types of the condition under investigation, in this case the condition is hearing loss of all types.

[3] In some countries, the fees are paid mainly by insurance companies, but in some other countries, the terms of insurance policies imply that the fees will only be paid by the company if some specific conditions are met, an example would be the constraints on hospitals, only in those the payment will be done by the insurance company [21].

and speech. Even after rehabilitation, deduction of mood based on the tone of voice would still be far more difficult than normal hearing for cases who previously had normal hearing [24]—So much so that even a device was patented [26] to address the issue by assigning one static predetermined color to predefined moods the person who is speaking might have. In addition, cochlear implants are shown to be most effective on infants [6], [27] for they are not used to normal hearing and their brains will adapt to that limited version of hearing. These facts decrease the benefit-to-cost ratio of the surgery for adult patients due to the low quality compared to high fees [23].

*2) Conservative Treatments*

There also had been attempts to aid the Auditory Impaired, by the use of Assistive Listening Devices and amplification [6]. Depending on type, some devices have variable amplification ratios, meaning the amount of amplification can be adjusted using a potentiometer, other types have a fixed amplification ratio for every frequency, which is set by examinations of a medical professional for each individual's unique amplification needs [14]. However, for STPHL cases, the threshold is usually so high that amplifying sound to the threshold level would cause pain or further damage to the structure of the ear [28]. Therefore, aside from the expensiveness of some models [6], such hearing aids cannot resolve the issue [5], [11], [13], [28]. This leads us to investigate two other ways, Sign Language and Visualization.

*3) Various Sign Languages*

Sign language of different kinds [15], [29], although at best only enabling verbal communication between the members of the Auditory Impaired and not a replacement for the sense of hearing, is usually of great help to the Auditory Impaired. Sign Language had long been one of the crucial tools to help educate the Auditory Impaired [29], although its different structure from the verbal language has made a significant difference in the learning of people with and without hearing [10], [15]. This difference also manifests in the communication between people with and without hearing, as the sign language used between the two differs significantly from the one used between the members of the auditory-impaired [30].

Because many people with hearing do not know sign language of any kind, normally a sign language translator will crucially be needed in case of communication between people with hearing and the Auditory Impaired [31]. However, manual translation often lags behind spoken communication. The efforts on non-manual translation have also been proved to be difficult as they are made out of two distinct problems, the first is the pattern recognition of the initial language, and the second is matching the order and grammar to the destination language [10].

*4) Visualizations*

Methods other than the ones discussed just above have also been proposed. Initial attempts [32] had mainly focused on building an intuition on what sound is through other senses presenting an impression of sound through feeling and seeing sound vibrations. Some more advanced methods, from which the Auditory Impaired would benefit in building further intuition on what sound is and how it propagates, were also invented; one method [33] is to monochromatically[4] visualize sound pressure at each point inside a given space (commonly known as a sound field). However, this invention was mainly intended to provide information on the acoustic properties of various materials built in various geometries [34] and it can convey neither linguistic nor indicatory information that is carried by the sound which is in fact, the most important to be retrieved by the Auditory Impaired.

Other Visualizers, which also do not aim to be hearing aids, made to visualize sounds (e.g. music) for concerts [35], [36], and are widely used for entertainment and their visual output does correspond to the input sound being

[4] Monochromatic, in color theory and physics, is referred to light of one static color, represented only by one single electromagnetic wave of one single frequency.

played. However, their algorithms do not exhibit a clear deducible connection with the input sound and input could not be inferred by viewing the output alone. This is because the visualizations usually implement random algorithms in their designs [35], [36].

Another method, which comes with no random algorithms implemented and aims for visualization of musical sound [37], although not claiming to be a hearing aid, works by assigning an EM wave frequency to each musical note; in other words, an EM wave frequency is assigned to each key on the piano. Such a method and the device made based on such method [38], comes with three issues. The first is that the output may extend beyond the visible spectrum and could not be seen or detected by normal human vision in everyday conditions [39]. The second is that even the difference in harmonics [5] different musical instruments produce, (which is the main distinction between them if viewed inside sound space) will not be translated into the output light, resulting in loss of information through the transformation by this method. The third is that everyday sounds cannot be translated by such a method unless only the parts of input sound matching the frequency of musical notes are used from the whole sample.

The succeeding method which was explicitly intended for the Auditory impaired, was mainly focused on exchanging the information sound carries rather than giving insight. This method [26] which previously discussed briefly in I.B.1), was to analyze the fluctuation inside the input sound and to visualize the mood of the speaker, who is reading a paragraph or conversating, by assigning one static, predetermined color of predetermined amplitude to each different mood (e.g. anger, tenderness, joy, etc.).

### C. *Objective*

Issues and complications discussed in I.B makes it apparent that, regarding the ways one perceives and processes visual stimulation (all that is perceived by sight e.g. chromatic vision, pattern recognition, and motion detection) and the ways one perceives sonar stimulation (all that is perceived by hearing such as tone recognition, motion detection[6] and the notion of sound texture[7], taking sonar stimulation to be a live recording or previously recorded sound clip in each moment[8]) and their primary properties, there exists an ideal translation that not only exhibits an optimal amount of computation but also maximally represents the input sound inside its output. We are in search of this ideal translation. However, such translation is not apparent to us; therefore, to pinpoint it, we shall consider the most possible basic sound under the action of such ideal translation, that is the translation of a sound clip, exhibiting only three sonar quantities; namely, the amplitude, the frequency and playing duration, all of which can be assigned to the whole sound clip. Calling the action of the unknown ideal translation on this basic sound clip, transformation of the input sound, reveals to us that, if we are to transform the input sound clip properly, we must map each of said quantities to a quantity with the same dimension. This principle comes from the logic of transformation we call consistency of the transformation. Therefore, consistency implies that sonar quantities of the input sound clip shall be mapped to the ideal visual representation's quantities as in Table **2**.

TABLE **2** THE CLOSEST MATCHING QUANTITIES OF COLOR VISION, TO THAT OF SOUND PERCEPTION

| Sound Quantity | Reminiscent Light Quantity |
|---|---|
| The Frequency $f$ of the sound clip | Visible EM wave[9] frequency $\nu$ (perceived as a monochromatic color) |
| Amplitude of $f$ | Light Intensity (Light Amplitude) |

[5] Hereafter, harmonic, is used in its musical sense, not the physical one, which is defined as a note produced on a musical instrument as an overtone.

[6] more primitive than of the motion detection experienced by sight

[7] the perceived sound texture is only the result of continuous tone detection through time, in other words, sound texture is nothing but how the amplitude of a sequence of tones are changing with respect to time.

[8] As the stimulation of a sound clip with sufficient quality, when played on a device which also shall come with sufficient playing quality, could replicate the sonar stimulation generated by the original sound, which was picked up by the microphone to generate the sound clip itself.

[9] Electro-Magnetic wave

Duration of $f$ Duration of the color being Displayed

As it is apparent from the mapping, the color perception of the eye is sufficient for mapping the entirety of the investigated sound clip[10]. Other aspects of vision, such as spatial pattern recognition, and three-dimensional depth perception, would not be needed.

Now, for the output to represent the input as closely as possible, we shall consider equal input and output durations, also considering the output intensity to be that of the sound clip amplitude only scaled inside the intensity levels of the screen. Now, there remains the task to properly mapping audible frequencies to the visible portion of EM waves.

## II. The Method

### A. *Constructing The Main Mapping Function*

To find the specific transformation T, which acts on sound frequency $f$ and outputs visible EM wave frequency $\nu$, we shall first investigate the necessary criteria, a general transformation between these two spaces shall have, in order for it to be considered a proper mapping function, which could serve as a useful aid for the auditory impaired. We will see afterwards, that, by consideration of these four crucial criteria, there remains one and only one specific transformation, with specific values for all its necessary parameters. We begin by stating every criterion in detail.

*1) Inversibility*

T shall act upon every sound frequency such that it would correspond to one and only one definite visible EM wave frequency, for one to be able to deduce the sound frequency played, by the color of the light resulting from the output of T; this can be stated mathematically as:

$$\forall\ T(f)=\nu:\exists\ T^{-1}(\nu)=f \tag{1}$$

*2) Conservation of Perception*

Every considerable transformation between any input space and an output space other than the input space will add some amount of distortion to the perceived change inside the input space when the input space is viewed through the output space. For the viable transformation, no such distortion shall be present and only the perceived change inside the input space shall be represented inside the output space; in other words, the representation of the input space must remain unchanged during transformation. This narrative implies the perception shall remain conserved during the act of transformation. Therefore, viable is the transformation, which conserves the perception.

To obtain the form of the viable transformation for every possible input and output space, the perceived difference of the input frequency space shall be proportional to the perceived difference in the output frequency space; as for our case, we know from acoustics [40] that the ear is sensitive to the change in the frequency concerning the base frequency—a relative change that is—despite the eye which we know from photometry [41], is sensitive to the change in color regardless of the base color[11]; therefore relative change in the input frequency space, will be proportional to the absolute change in the output frequency space, mathematically stated as:

$$\begin{aligned}&\forall\ T(f)=\nu:\frac{df}{f}\propto d\nu\\&\rightarrow T(f)=k\ln\left(1+\frac{f-f_i}{f_0}\right)+c\end{aligned} \tag{2}$$

Where in Eq. (2), $f_i$ would be the starting input frequency, $f_0$ is a frequency constant that by convenience is chosen to be the peak frequency of human hearing and $k$ and $c$ are constants

[10] Motion detection by the sound, which manifests as changing of amplitude through respective recording channels, can also be mapped to the motion of a color gradient inside the output display, but because the exact algorithm as to the gradient properties shall be implemented inside the source code of the computing unit, the transformation of one channel of the input audio is discussed and the procedure will be the same for all other channels.

[11] The color is perceived as the activation of the three cone cells in photopic vision, and the change in the frequency of the visible EM wave results in a precise amount of change of the perceived color regardless of the base color.

defined by physical boundary conditions and other mathematical constraints.

*3) Completeness of The Transformation*

For one to recognize all possible input frequencies, all perceivable input frequencies shall be mapped onto all perceivable output frequencies; that is the domain and range of the transformation function shall be all audible frequencies and the visible spectrum respectively; mathematically stated as:

$$\begin{aligned} &\forall\ T(f)=\nu: \\ &20\text{Hz} \le f \le 20\text{kHz} \\ &\wedge\ 450\text{THz} \le T(f) \le 710\text{THz} \end{aligned} \tag{3}$$

Here shall be stated that because neither the visible spectrum nor audible range has a definite dividing line, the visibility of different radiation on the IR and UV range close to the vague ends of visible spectrum depends on the amplitude and the sensitivity of the individual [39] (same is true for the audibility of the ends of hearing range [42]), the standard, agreed upon visible ranges [43] and audible [44] to average person, in normal conditions, are used, respectively.

*4) Ascending Output and Peak Mapping*

The two other constraints required for convergence of the transformation in future updates are that the lowest, highest and most perceivable frequencies in the input space shall be mapped to their respective counterparts in the output space; these requirements impose two mathematical constraints on the transformation, which are stated as:

$$\forall\ T(f)=\nu: \frac{dT(f)}{df} > 0 \tag{4}$$

$$\forall\ T(f)=\nu: T(f=3.2\text{kHz}) = 540\text{THz} \tag{5}$$

Imposing all these criteria together, the general transformation function will be reduced to one specific form with all the parameters determined; which after some computation, simplifies to:

$$T(f) = (130.43\text{THz})x + 450.00\text{THz} \tag{6}$$

Where in Eq. (6), $x$ is defined to be:

$$x \equiv \ln\left(1+\frac{f-20\text{Hz}}{3.2\text{kHz}}\right) \tag{7}$$

Equations (6) and (7) make up the entirety of the proper transformation from a sound frequency $f$ to an EM wave with a frequency $\nu$ within the visible portion of the EM radiation, which represents a light of monochromatic color, most closely representing the input audio frequency inside the color vision.

### B. *Constructing The Rendering Function*

Although the transformation expressed in Eq. (6) and (7) will yield the output EM wave frequency, such output cannot be directly used to generate the color the output frequency represents; to properly show the corresponding output color inside a display, the output shall again be rendered in a color space [12] and because the visualization is going to occur inside a computing unit with an RGB display, the color space used, will be sRGB color space. Therefore, we shall proceed by derivation of the rendered version of the previous transformation in the form:

$$\mathbf{T}(f) \equiv T_R(f)\hat{\mathbf{R}} + T_G(f)\hat{\mathbf{G}} + T_B(f)\hat{\mathbf{B}} \tag{8}$$

Noting that hatted vectors are respective base color vectors of the sRGB space, and $T_R(f), T_G(f)$ and $T_B(f)$ are respective output brightness values needed to produce the monochromatic color the output EM wave frequency of the previous transformation represents when acted upon sound frequency *f*.

To obtain $\mathbf{T}(f)$, based on the output values of the previous transformation $T(f)$, we shall

[12] A color space is a vector space, in which a set of discrete or continuous colors can be represented by addition of a finite number of base color vectors of corresponding scalar coefficients, therefore, every color inside a color space is represented by a vector of base color coefficients.

assume, there exists at least one other transformation, which we will call the rendering function, and define as:

$$\boldsymbol{\sigma}(\nu) \equiv \sigma_R(\nu)\hat{\mathbf{R}} + \sigma_G(\nu)\hat{\mathbf{G}} + \sigma_B(\nu)\hat{\mathbf{B}} \tag{9}$$

which takes as input, EM wave frequency $\nu$ of a monochromatic color, and outputs the sRGB brightness values needed to represent that same color inside an RGB display. Stating that assumption, the exact definition of $\mathbf{T}(f)$, will be:

$$\begin{aligned}\mathbf{T}(f) \equiv \boldsymbol{\sigma}(T(f)) = \sigma_R(T(f))\hat{\mathbf{R}} \\ + \sigma_G(T(f))\hat{\mathbf{G}} \\ + \sigma_B(T(f))\hat{\mathbf{B}}\end{aligned} \tag{10}$$

Therefore, our task was reduced to obtaining $\boldsymbol{\sigma}(\nu)$. Because such a task relates to how we shall reproduce a certain color in the eye, we will start from the human eye spectral tristimulus function.

*1) Human Spectral Tristimulus Function*

Humans perceive colors, trichromatically. Meaning, that every perceived color will be decomposed into three activation values for three primary contributions to the perception of three distinct color-like pigments. The reason for expressing the three receptors as perceiving three color-like pigments and not colors themselves is the fact that the data obtained from human tristimulus sensitivity functions [45], which is shown in Fig. **2**, it can be inferred that none of the visible colors inside the visible spectrum are the result of activation in only one single type of cone cell. This inference can be made from the simple observation that there is no color at which only one type of cone cell is active [39], [46][13]. The only case in which the actual pigment associated with one type of cone cells (the L-cone) could be detected by the eye was at high-intensity infrared shining to the eye at an experiment mentioned in [39]. Also, the L-cone is the only type of cone cell for which the pigment can be seen by the naked eye, as there is nowhere on the visible spectrum that the M-cone or the S-cone are solemnly activated. Therefore, the individual color of the cone cells cannot be represented inside an external device. That is the reason the name of the cone cells is changed to L, M, and S-cones, instead of red, green, and blue cones.

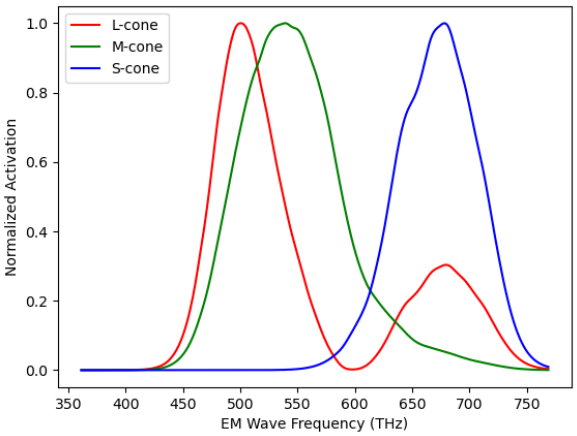


Fig. **2** Normalized Activation of Cone Cells in Photopic Vision concerning D65 White Point

As plotted in Fig. **2**, the tristimulus sensitivity functions are assumed to yield the three activations of each type of cone cell in terms of visible EM wave frequency or wavelength[14]. If we define a numerical visual stimulus function, based on the data plotted in Fig. **2**, in the form:

$$\mathbf{S}(\nu) \equiv a_L(\nu)\hat{\mathbf{L}} + a_M(\nu)\hat{\mathbf{M}} + a_S(\nu)\hat{\mathbf{S}} \tag{11}$$

Where $a_L(\nu)$, $a_M(\nu)$ and $a_S(\nu)$ are normalized activation values of L, M, and S-cones respectively. Also, the hatted vectors are defined as base activation unit vectors, for respective cone cells[15].

*2) Obtaining The Display Matrix*

To obtain from the human tristimulus function $\mathbf{S}(\nu)$, the desired rendering function $\boldsymbol{\sigma}(\nu)$, we shall develop the matrix transformation by which we could transfer the vector of a certain color, from the activation space to the sRGB space; such task is done by treating the sRGB

[13] In order for the color seen at that imaginary point to be assumed as the color of the cone cell which is solemnly activated at that color.

[14] The original data from CIE determined the activation values with respect to wavelength; but since we have mapped sound frequencies to EM wave frequencies, we plotted the data with respect to frequency.

[15] Note that, $\mathbf{S}(\nu)$ shall not be confused with $\hat{\mathbf{s}}$.

base vectors as normalized color vectors of the three primary colors of the screen inside the tristimulus activation space, assuming $\nu_R$, $\nu_G$ and $\nu_B$ as their EM wave frequencies respectively. By such assumption, we have:

$$\hat{\mathbf{R}} = \frac{\mathbf{S}(\nu_R)}{|\mathbf{S}(\nu_R)|} = \frac{a_L(\nu_R)\hat{\mathbf{L}} + a_M(\nu_R)\hat{\mathbf{M}} + a_S(\nu_R)\hat{\mathbf{S}}}{\sqrt{a_L^2(\nu_R) + a_M^2(\nu_R) + a_S^2(\nu_R)}} \quad (12)$$

$$\hat{\mathbf{G}} = \frac{\mathbf{S}(\nu_G)}{|\mathbf{S}(\nu_G)|} = \frac{a_L(\nu_G)\hat{\mathbf{L}} + a_M(\nu_G)\hat{\mathbf{M}} + a_S(\nu_G)\hat{\mathbf{S}}}{\sqrt{a_L^2(\nu_G) + a_M^2(\nu_G) + a_S^2(\nu_G)}} \quad (13)$$

$$\hat{\mathbf{B}} = \frac{\mathbf{S}(\nu_B)}{|\mathbf{S}(\nu_B)|} = \frac{a_L(\nu_B)\hat{\mathbf{L}} + a_M(\nu_B)\hat{\mathbf{M}} + a_S(\nu_B)\hat{\mathbf{S}}}{\sqrt{a_L^2(\nu_B) + a_M^2(\nu_B) + a_S^2(\nu_B)}} \quad (14)$$

Substituting the expressions in Eq. (12), (13) and (14), into the definition of the rendering function and rearranging the terms, we will get:

$$\frac{\begin{pmatrix} a_L(\nu_R) & a_L(\nu_G) & a_L(\nu_B) \\ a_M(\nu_R) & a_M(\nu_G) & a_M(\nu_B) \\ a_S(\nu_R) & a_S(\nu_G) & a_S(\nu_B) \end{pmatrix}}{\sqrt[3]{|\mathbf{S}(\nu_R)||\mathbf{S}(\nu_G)||\mathbf{S}(\nu_B)|}}\boldsymbol{\sigma}(\nu) = \mathbf{S}(\nu) \quad (15)$$

Now, defining M to be:

$$M \equiv \frac{\begin{pmatrix} a_L(\nu_R) & a_L(\nu_G) & a_L(\nu_B) \\ a_M(\nu_R) & a_M(\nu_G) & a_M(\nu_B) \\ a_S(\nu_R) & a_S(\nu_G) & a_S(\nu_B) \end{pmatrix}}{\sqrt[3]{|\mathbf{S}(\nu_R)||\mathbf{S}(\nu_G)||\mathbf{S}(\nu_B)|}} \quad (16)$$

The rendering function will be[16]:

$$\boldsymbol{\sigma}(\nu) \equiv M^{-1}\mathbf{S}(\nu) \quad (17)$$

*3) Correction for Invalid RGB Values*

The definition provided for $\boldsymbol{\sigma}(\nu)$, works for satisfying cases of color representations. However, it fails to yield proper sRGB values for a significant number of cases. To acquire proper values in all its domains, an error correction algorithm shall map every color outside the color gamut of sRGB color space, to a nearest point inside the color gamut of sRGB. This algorithm shall be implemented inside the source code of the computing unit. However, we are going to briefly introduce the algorithm. For every output of the rendering function, the sRGB values are converted to CIE xy-coordinates; then the algorithm checks whether the coordinate point the color had been transformed into, lies inside sRGB boundaries. If the point was outside the sRGB color gamut (in which case the output sRGB values cannot be displayed), as in Fig. **3**, the coordinates of the intersection point of the line drawn from the point to the white point and the closest sRGB boundary will be converted to sRGB and displayed instead of the original point.

Conversions and computations are carried out in [47].

[16] Some additional scaling is needed for the final rendering function to yield 8-bit RGB values in the code implementation.

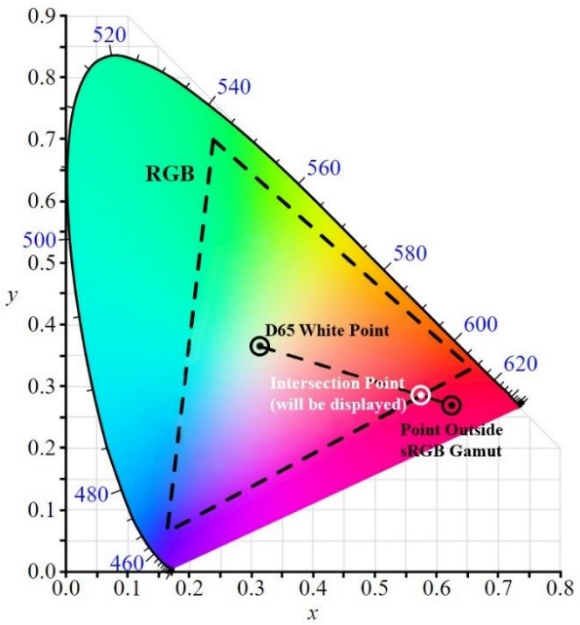


Fig. **3** Human Color Gamut and sRGB Color Gamut; The intersection point is going to be used instead of the original point when the point is detected to be outside the sRGB color gamut.

Applying this algorithm concludes the sRGB numerical rendering function, although, for better results, an iterative smoothing will also be carried. The rendering is shown in Fig. **4**.

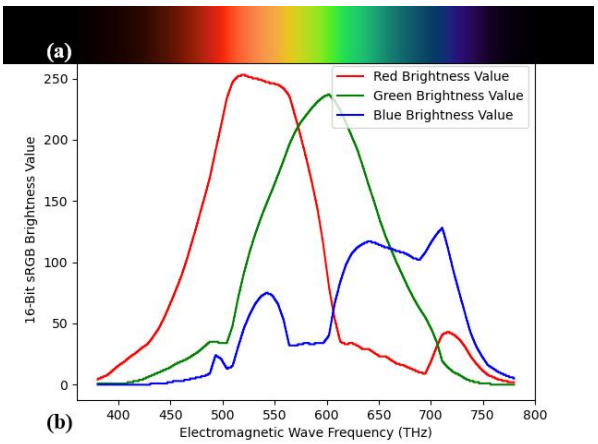


Fig. **4** The visible spectrum (a) and brightness values (b) generated by the obtained sRGB rendering function vs. EM wave Frequency for every color

## C. *Applying the Transformation to an Actual Sound Clip*

So far, the method as to the transformation and correlation of sound of one single definite frequency to light of a single monochromatic color has been discussed. However, the correlation of real-world soundtracks is not as simple. First, we consider continuous sound recording and then we cover the digital sound recording procedure in a successive section.

*1) Continuous (Analog) Sound Tracks*

Even sounds and voices recorded from ordinary phenomena, usually consist of multiple frequencies with different amplitudes. In that case, the above-resulted transformation shall act upon each different frequency of the track as stated below:

$$\mathbf{v}_{\text{color}}(t)=\int_{f_i}^{f_f}\frac{a(f,t)\mathbf{T}(f)}{A_{\max}}df \tag{18}$$

Where $\mathbf{v}_{\text{color}}(t)$ is the result of applying the transformation on every constituent frequency inside the sound clip at every moment and is therefore the translation of the sound clip to a color frame at time $t$, $f_i$ and $f_f$ are the beginning and end of the input frequency domain (which in this case is the audible range), and $A_{\max}$ is the maximum amplitude of the recorded sound clip[17]. For the above matter, our task will be reduced to finding the constituent amplitudes $a(f,t)$ of every frequency $f$; the matter is achieved, by applying Fourier Transformation on the recorded sound clip, as below:

$$A(f)=\int_{-\infty}^{\infty}\bar{A}(t)e^{-2\pi ift}dt \tag{19}$$

Where $A(f)$ is the amplitude of each frequency $f$, $\bar{A}(t)$ is the normalized recorded pressure difference at each time $t$. The limits of the integral reduce to the start and end of the sound clip, in the process of integration. While the above expression only gives the sum of all amplitudes over all times, we want to take the amplitude of every frequency $f$ at each different time $t$, that is:

[17] For a live recording of sound, a constant reference shall be considered instead.

$$\int_{-\infty}^{\infty} \bar{A}(t')\, e^{-2\pi i f t'}\, dt' = \int_{-\infty}^{\infty} a(f,t')\, dt'$$
$$\rightarrow a(f,t) = \int_{t-\varepsilon}^{t+\varepsilon} \bar{A}(t')\, e^{-2\pi i f t'}\, dt' \quad (20)$$

*2) Finite Sample Rate (Digital) Sound Tracks*

In practice, however, the sound cannot be recorded continuously, and there only is, a finite time series of samples, with a definite sampling rate, of the recorded sound; in this case, the above equations transform into discrete sums, also, the color vector, formerly at every moment, shall now be computed at a definite frame rate, which by standard conventions, will be taken to be 24 frames per second. Now, in the case of finite sample rate sound clips, Eq. (20) becomes:

$$a_i = \sum_{j=1}^{N} A_j e^{-2\pi i f_i t_j} \quad (21)$$

Where in Eq. (21), $N$ is defined to be:

$$N \equiv \frac{R_{\text{Sound Sampling}}}{R_{\text{Frame}}} \quad (22)$$

Where the numerator is the sound sampling rate (in Hertz), and the denominator is the frame rate (in fps, which is equivalent to Hertz). Also, because of the discreteness possessed by the current case, the frequency spectrum in Eq. (18) and (19) will reduce to a set of allowed discrete frequencies, with their value being:

$$f_i \equiv i \frac{R_{\text{Sound Sampling}}}{N} = i R_{\text{Frame}}$$
$$i = 1, 2, 3, \cdots, 833 \quad (23)$$

The reason for the upper boundary is defined for $i$ is to restrict the computations only to audible frequencies. And Therefore, the integral for obtaining the color frame at each moment, in Eq. (18) changes to a summation and we will have:

$$\mathbf{v}_{\text{frame}} = \frac{\sum_{i=1}^{833} a_i \mathbf{T}(f_i)}{A_{\max}} \quad (24)$$

Where here $\mathbf{v}_{\text{frame}}$ is the color vector of one frame of the generated output[18].

## III. Conclusion

Using the cascaded rendered transformation function which is in the form of Eq. (8), and applying the Fast Fourier Transform (FFT) Algorithm [48], [49] successively on each one over twenty forth of a second of the sound clip to find $a_i$ defined in Eq. (21), and then substituting the obtained values in Eq. (24), we can generate a proper, consistent translation of any recorded or real-time sound clip to a visual output; Because of the consistency of the procedure, sound texture, which is the change inside the amplitude of a sequence of tones, is also translated as a pattern inside the output time spectrum as shown in Fig. **5**.

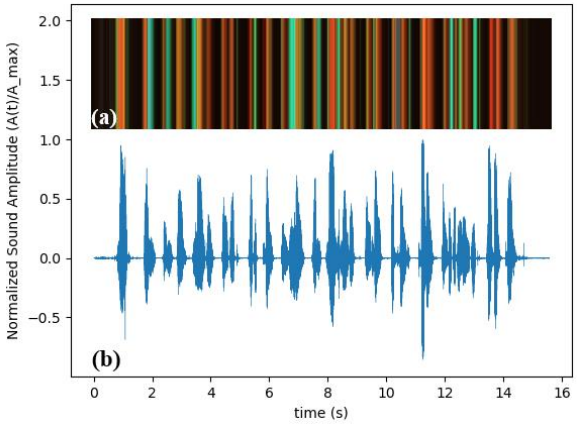


Fig. **5** Time spectrum visual translation (a) of the voice of the first author (b) stating: "Hi, this is a sample input which we can see is translated into different color constituents over time". As apparent, different tones and vocals have distinct colors

Because the formulated translation practically enables perceiving sound through the sense of sight, not only does it provide the Auditory Impaired, the ability to infer and learn vocal structure, and grammar, but also enables them

[18] Some additional scaling will be needed in the source code of the computing unit in order for the result of the summation to fit inside sRGB values range.

to detect the presence and the details of other sounds in general (the sound of cars approaching, things dropping as in Fig. **6**, and other indicatory sounds) being the only method to enable this level of sound deduction.

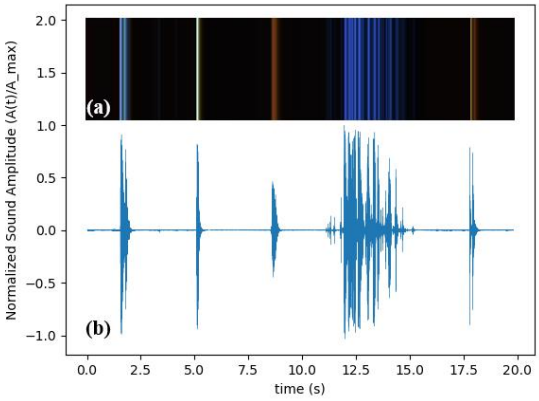


Fig. **6** Time spectrum visual representation (a) of some sounds (b); in order of occurrence sound from dropping of keys, falling of a book, saying 'hey' to call someone, shaking of keys, and putting a glass on a small plate; microphone was fixed at normal height of the ear of a person when sitting, colors are notably different for each, enabling deductions possible

Because the presented algorithm, is a way to translate and visualize any set of mechanical waves of any frequency range and duration, the other important application for such an algorithm is visualizing seismic waves inside the visible spectrum; by applying the discussed translation on a dataset recorded from a seismographer, the cause of every seismic movement can be inferred as each cause generates a distinct set of seismic waves which correspond to a distinct color representation for each different cause of seismic vibrations. This algorithm also presents a proper, consistent, and convenient way to visualize the data obtained from seismographers which are placed in various locations. The data can then be visualized on the map of the area and can then be used to process the propagation of earthquakes or other geological phenomena.

The other application of such a device is that it can reproduce a certain type of condition known as Synesthesia, the type in which the person having the condition, associates colors to sound. Although the association different people experience may differ in the exact sound-to-color correspondence—which may not even be consistent enough to be considered a correspondence —the presented algorithm can reproduce the same feeling and also can be modified to replicate the association that a certain person reports as having experienced.

Overall, not only can the translation witnessed in Fig. **5** and Fig. **6** aid the Auditory Impaired to understand sounds and vocal languages, or graph any acoustic data of any range by considering the frequency range of data under question, but it is also hoped to open up a window of new possibilities for exploration and research on the physics and the science of human perception, and respective translation between different senses in a precise, quantitative manner.

## APPENDIX

### A. *Obtaining The Parameters of The Logarithmic Transformations*

As discussed, the frequency transformation function was found by the statement of the **second mapping criterion** to be in the specific form:

$$y(f) = k \ln(f - f_0) + c \tag{25}$$

Our general problem will be to obtain the values of the 3 parameters $k$, $f_0$ and $c$, in terms of the coordinates of three points:

$$(f_1, y_1), (f_2, y_2), (f_3, y_3)$$

But constructing the three equations with three parameters of the function as the unknowns will result in a non-linear system of equations therefore making the direct solving of the equations an elaborate mathematical problem, even in the numerical solution cases. So, here is explained instead, another method to tackle the problem, which will result in a far more efficient numerical calculation and also yields a direct solution to two of the three parameters and a numerical, but arbitrarily exact solution to the third.

First, we consider the inverse of the function in the form:

$$Y = as^{x} + b \tag{26}$$

Which we will call from now on, 'the inverse function'. The parameters of this function are related to the original parameters in the following way:

$$\begin{aligned} &Y \equiv f \\ &x \equiv y \\ &a = e^{\frac{-c}{k}} \rightarrow c = -\log_s(a) \\ &b = f_0 \\ &s = e^{\frac{1}{k}} \rightarrow k = \frac{1}{\ln(s)} \end{aligned} \tag{27}$$

with the coordinate of the points initially considered, getting flipped to account for the inversion of the function and the new points considered will be:

$$\begin{aligned} &(x_1 \equiv y_1, Y_1 \equiv f_1) \\ &(x_2 \equiv y_2, Y_2 \equiv f_2) \\ &(x_3 \equiv y_3, Y_3 \equiv f_3) \end{aligned} \tag{28}$$

The three points chosen such that:

$$\begin{aligned} x_1 < x_3 < x_2 \\ y_1 < y_3 < y_2 \end{aligned}$$

Now, if we define,

$$X = s^{x} \tag{29}$$

as the new input, our inverse function in the Eq. (26) becomes:

$$Y = aX + b \tag{30}$$

Which is the definition of a line, the parameters of which can be pinpointed to exact values by considering two of the three points of Eq. (28); so for *a* and *b* we will have:

$$\begin{cases} a = \dfrac{\Delta Y_{21}}{\Delta X_{21}} \\ b = \dfrac{X_2 Y_1 - X_1 Y_2}{\Delta X_{21}} \end{cases} \tag{31}$$

Where $\Delta A_{ij}$ is defined to be[19]:

$$\Delta A_{ij} \equiv A_i - A_j \tag{32}$$

Where *A* can be any of the above variables (e.g. *x*, *X*, *Y*, etc.). Because of the change of variables considered in Eq. (29), *a* and *b* will both depend on the parameters of Eq. (26); however, both parameters are tuned by Eq. (31) in such a way that:

$$\begin{cases} as^{x_1} + b = Y_1 \\ as^{x_2} + b = Y_2 \end{cases} \quad \forall s \in \mathrm{R}^{+} - \{0,1\} \tag{33}$$

As mentioned in Eq. (33), both parameters are set in such a way that the inverse function will contain the first and the second points of (28) for all positive values of *s* except for one and zero; this means we can tune the value of *s* in order for the inverse function to also contain the third point without losing the two other points.

For the inverse function to contain the third point $(x_3, Y_3)$, the distance of the output of the function on $X_3 = s^{x_3}$ from the y-coordinate of the point shall be zero in other words:

$$|Y_3 - as^{x_3} + b| = 0 \tag{34}$$

But as said before, considering the variable change of Eq. (29) for *X*, *a*, and *b* are themselves in terms of *s*; by substituting respective change of variables inside Eq. (31) and substituting *a* and *b* inside (34) from (31) we will have:

[19] This will be the conventional notation wherever we are faced with incremental differences of values with various indices; which often happens in case of the computations of the parameters of interpolation functions.

$$Y_3 - \frac{\Delta Y_{21} s^{x_3} + s^{x_2} Y_1 - s^{x_1} Y_2}{s^{x_2} - s^{x_1}} = 0 \tag{35}$$

Which after an amount of simplification yields:

$$s^{x_3} \Delta Y_{21} - s^{x_2} \Delta Y_{31} + s^{x_1} \Delta Y_{32} = 0 \tag{36}$$

Which is a polynomial equation of degree $x_2$ on[20] $s$. Equation (36) is of course a problem solvable only by numerical methods as the values of powers of $s$ can be any real number. Attempting to solve Eq. (36) by Newton's Method will yield three answers, two of which (zero and one) are the apparent solutions to the equation and also obsolete in the sense that they are forbidden base values of exponentials, therefore they are outside the range of possible values of $s$.

To remove the obsolete solution $s = 0$ from Eq. (36), we can divide both sides by $s^{x_1}$ to obtain:

$$s^{\Delta x_{31}} \Delta Y_{21} - s^{\Delta x_{21}} \Delta Y_{31} + \Delta Y_{32} = 0 \tag{37}$$

Which will yield a polynomial of degree $\Delta x_{21}$. Aside from removing zero out of solutions, such polynomial has the advantage that its powers are usually far smaller than the one in (36); this fact and the fact that this polynomial is a better-behaving curve in the range the solutions exist, will mean reaching the desired solution would need far less iterations, resulting in Eq. (37) being a far better and more efficient choice for numeric computations[21]. As is apparent from Eq. (36) and (37), the problem of solving a system of equations was reduced to one root-finding problem for only one of the parameters and the precision of all three parameters can be controlled to match any arbitrary amount by the number of iterations considered.

By obtaining the value of $s$, $a$ and $b$ will also be found by substituting the obtained value of $s$ inside Equations (31) and (29); and finally the parameters of Eq. (25) can also be found using the relations of (27).

As is apparent from our narrative, the parameter $s$ was the parameter that tuned the curvature of our function, to the amount needed for the function to account for the third point in between the two initial points; and as we know from relations of (27):

$$s^x = e^{\frac{x}{k}} \tag{38}$$

and by taking the limit of $s$ to one—when $a$ and $b$ are evaluated from (31)—we will see that:

$$\lim_{s \to 1} s^x = \lim_{k \to \infty} e^{\frac{x}{k}} \approx 1 + \frac{x}{k} \tag{39}$$

and the Eq. (26), when $a$ and $b$ are substituted from (31) becomes:

$$Y = \frac{\Delta Y_{21}}{1 + \frac{x_2}{k} - (1 + \frac{x_1}{k})} (1 + \frac{x}{k}) + \frac{(1 + \frac{x_2}{k}) Y_1 - (1 + \frac{x_1}{k}) Y_2}{(1 + \frac{x_2}{k}) - (1 + \frac{x_1}{k})} \tag{40}$$

Which after some amount of simplification becomes:

$$y = \frac{\Delta Y_{21}}{\Delta x_{21}} x + \frac{x_2 Y_1 - x_1 Y_2}{\Delta x_{21}} \tag{41}$$

Which is the definition of a line passing through the first and second points defined in (28). This case will correspond to the absence of curvature in the inverse function; therefore, we can infer, that the parameter $s$ indicates how *curved* is the inverse function and also our main transformation function. By further examination of Eq. (38), we can see that $s = 1$, corresponds to no curvature and $s = e$ will

[20] As is apparent from the constraints applied on the points after the definitions of new points in (28);

[21] It shall be noted that this will only be true when $x_1$ and $x_2$ are of the same sign, otherwise (36) is the better choice; in our case (37) is preferred.

result in a curvature amount of one exponential unit; therefore we define:

$$C \equiv \ln(s) = \frac{1}{k} \tag{42}$$

As the transformation's 'Curvature Constant'. This constant is the exact indicator of how much exactly an exponential or a logarithm is curved away from the equivalent line passing through the endpoints of the interval under investigation; and for the case of transformation from average hearing to average sight, Curvature Constant will be:

$$C_{\mathrm{HS}} \approx \frac{1}{132.640964097\mathrm{THz}} \approx 7.53914906158\mathrm{fs} \tag{43}$$

As it is apparent, the Curvature of the transformation from Hearing to Sight is very small, but the tiniest change inside its value will vastly change output color mapping[22]; for this also, the achievement of its precise value is crucial to the validity of the transformation. The Curvature Constant declared in Eq. (43) is a fundamental constant of human perception[23] and will be of great importance to the current and future work in the field of sense translation.

## ACKNOWLEDGMENT

Here, we take the chance to deeply thank the professors at Kharazmi University Faramarz Kanjouri, Saeed Tavassoli, Ali Vahedi, Mohammad Soltanian, and Farzan Momeni who provided us, with the required guidance. We also thank Amir Hossein Moradi for their valuable helpings. Also, the full development of the whole project could not be possible without the help of S. Nima M. Mousavi, both on the algorithm and the proper way as to explain it.

## REFERENCES

**[1]** World Health Organization, "Deafness and Hearing Loss," Accessed: May 02, 2024. https://www.who.int/news-room/fact-sheets/detail/deafness-and-hearing-loss

**[2]** B. O. Olusanya, A. C. Davis, and H. J. Hoffman, "Hearing loss grades and the international classification of functioning, disability and health," World Health Organization, vol. 97, pp 725–728, 2019.

**[3]** Informed Health, "Can noise damage your hearing?" Institute for Quality and Efficiency in Health Care. Accessed: Feb. 07, 2025. https://www.informedhealth.org/can-noise-damage-your-hearing.html

**[4]** G. Stevens, S. Flaxman, E. Brunskill, M. Mascarenhas, C. D. Mathers, and M. Finucane, "Global and regional hearing impairment prevalence: an analysis of 42 studies in 29 countries," Acad. Stevens, S Flaxman, E Brunskill, M Mascarenhas, CD Mathers, M FinucaneThe Eur. J. Public Heal. 2013•academic.oup.com, vol. 23, pp. 146–152, 2013.

**[5]** E. Holmes and T. D. Griffiths, "'Normal' hearing thresholds and fundamental auditory grouping processes predict difficulties with speech-in-noise perception," Sci. Rep. vol. 9, pp. 16771, 2019.

**[6]** S. Anastasiadou and Y. Al Khalili, "Hearing Loss," StatPearls Publishing, vol. 22, pp. 1–7, 2023. https://www.ncbi.nlm.nih.gov/books/NBK542323/

**[7]** C. Löfvenberg *et al.*, "Prevalence of severe-to-Profound hearing loss in the adult Swedish population and comparison with cochlear implantation rate," *Acta Otolaryngol.*, vol. 142, no. 5, pp. 410–414, 2022.

**[8]** W. E. Brownell and B. R. Alford, "HOW THE EAR WORKS - NATURE'S SOLUTIONS FOR LISTENING," Volta Rev. vol. 99, pp. 9, 1997, 2025. [Online]. Available: https://pmc.ncbi.nlm.nih.gov/articles/PMC2888317/

[22] To express briefly, the reason as to the constant exhibiting dimension, is that it is referring to a delay in perception of the ear relative to the eye, a detailed investigation for the validity of this claim is needed, and will be done.

[23] The exact value of the constant depends on the exact values of parameters of Hearing and Sight of the individual; however, the value declared in Eq. (43) was found by taking the conventional range of audible acoustic waves and visible spectrum which was declared in the main body text.

**[9]** Y. C. Tseng, S. H. Y. Liu, B. S. Gau, T. C. Liu, N. T. Chang, and M. F. Lou, "Lived experiences and illness perceptions of older adults with age-related hearing loss before the use of hearing aids: An interpretative phenomenological study," Geriatr. Nurs. (Minneap). vol. 61, pp. 231–239, 2025.

**[10]** N. C. Camgoz, S. Hadfield, O. Koller, H. Ney, and R. Bowden, "Neural Sign Language Translation," Proc. IEEE Comput. Soc. Conf. Comput. Vis. Pattern Recognit. pp. 7784–7793, 2018.

**[11]** C. Löfvenberg, S. Turunen-Taheri, P. I. Carlsson, and Å. Skagerstrand, "Rehabilitation of Severe-to-Profound Hearing Loss in Adults in Sweden," Audiol. Res. 2022, Vol. 12, Pages 433-444, vol. 12, pp. 433–444, 2022.

**[12]** A. Ringdahl and A. Grimby, "Severe-profound hearing impairment and health-related quality of life among post-lingual deafened Swedish adults," Scand. Audiol. vol. 29, pp. 266–275, 2000.

**[13]** M. A. Ferguson, P. T. Kitterick, L. Y. Chong, M. Edmondson-Jones, F. Barker, and D. J. Hoare, "Hearing aids for mild to moderate hearing loss in adults," Cochrane Database Syst. Rev. vol. 2017, pp. CD012023, 2017.

**[14]** L. Turton et al., "Guidelines for best practice in the audiological management of adults with severe and profound hearing loss," Seminars in Hearing, vol. 41, pp. 141–245, 2020.

**[15]** W. C. Stokoe, "Sign Language Structure," Annu. Rev. Anthropol., vol. 9, no. 1, pp. 365–390, 1980.

**[16]** L. Turton and P. Smith, "Prevalence & characteristics of severe and profound hearing loss in adults in a UK National Health Service clinic," Int. J. Audiol. vol. 52, no. 2, pp. 92–97, 2013.

**[17]** W. Li, Z. Zhao, Z. Lu, W. Ruan, M. Yang, and D. Wang, "The prevalence and global burden of hearing loss in 204 countries and territories, 1990–2019," Environ. Sci. Pollut. Res. vol. 29, pp. 12009–12016, 2022.

**[18]** G. J. Im *et al.*, "Prevalence of severe-profound hearing loss in South Korea: a nationwide population-based study to analyse a 10-year trend (2006–2015)," Sci. Reports 2018 81, vol. 8, pp. 1–9, Jul. 2018.

**[19]** National Institute on Deafness and Other Communication Disorders, "What Is Otosclerosis? Symptoms & Diagnosis." Accessed:, 2025. [Online]. Available: https://www.nidcd.nih.gov/health/otosclerosis

**[20]** National Health Service UK, "Cholesteatoma." Accessed: Feb. 07, 2025. [Online]. Available: https://www.nhs.uk/conditions/cholesteatoma/

**[21]** Tehran Ear Clinic, "The Cost of Cochlear Implants, Do the insurance companies cover the fees?" Accessed: 2024. [Online]. Available: https://tehranearclinic.com/blog/cochlear-implant-cost

**[22]** TriHealth, "Surgical Treatment for Hearing Loss." Accessed: 2024. [Online]. Available: https://www.trihealth.com/services/ear-nose-and-throat/ent-treatments-and-services/surgical-treatment-for-hearing-loss

**[23]** Forbes Health and Duke Department of Head and Neck Surgery & Communication Sciences, "How Much Do Cochlear Implants Cost?" Accessed: 2024. [Online]. Available: https://headnecksurgery.duke.edu/news/forbes-health-how-much-do-cochlear-implants-cost

**[24]** Cochlear Implant Brain and Behavior Lab, "What does the world sound like through a cochlear implant?" Accessed: May 04, 2024. [Online]. Available: https://cochlearimplant.lab.uconn.edu/cochlear-implant-information/sounds/

**[25]** A. Ciorba *et al.* "Rehabilitation of Severe to Profound Sensorineural Hearing Loss in Adults: Audiological Outcomes," *Ear, Nose Throat J.*, vol. 100, pp. 215S-219S, Jun. 2021.

**[26]** C. Lee, "Sound to light converter and its method," KR20050089440A, 2004 Accessed: 2024. [Online]. Available: https://patents.google.com/patent/KR20050089440A/en?oq=KR20050089440

**[27]** F. G. Zeng, S. Rebscher, W. Harrison, X. Sun, and H. Feng, "Cochlear Implants: System Design, Integration, and Evaluation," *IEEE Rev. Biomed. Eng.* vol. 1, pp. 115–142, 2008.

**[28]** E. W. Johnson, "Hearing Aids And Otosclerosis," Otolaryngol. Clin. North Am., vol. 26, pp. 491–502, 1993.

**[29]** C. Valli, C. L. Washington, and D. C. Gallaudet, Linguistics of American Sign Language: An Introduction (3rd Ed.), vol. 1. 2024. [Online]. Available: https://books.google.com/books?hl=en&lr=&id=mfS3GlTLAUMC&oi=fnd&pg=PP13&dq=sign+language&ots=QuNlND-

bBu&sig=mtjMWqhiz-UcPQYy87QvUwcW1fs#v=onepage&q=sign language&f=false

**[30]** E. Domagała-Zyśk and A. Podlewska, "Strategies of oral communication of deaf and hard-of-hearing (D/HH) non-native English users," *Eur. J. Spec. Needs Educ.*, vol. 34, no. 2, pp. 156–171, 2019.

**[31]** O. Koller, J. Forster, and H. Ney, "Continuous sign language recognition: Towards large vocabulary statistical recognition systems handling multiple signers," Comput. Vis. Image Underst. vol. 141, pp. 108–125, 2015.

**[32]** W. C. Hayes, "Sound to light visual vocalization system," US3572919A, 1968 Accessed:, 2024. [Online]. Available: https://patents.google.com/patent/US3572919A/en?oq=US3572919+(A)

**[33]** M. Kurihara and J. Fujimori, "Sound to light converter and sound field visualizing system," US20120097012A1, 2012 Accessed: May 19, 2024.

**[34]** H. Lim, M. Imran, and J. Y. Jeon, "A new approach for acoustic visualization using directional impulse response in room acoustics," Build. Environ. vol. 98, pp. 150–157, 2016,

**[35]** A. Blok, "Sound-to-light graphics system," WO1994022128A1, 1994 Accessed: May 19, 2024. [Online]. Available: https://patents.google.com/patent/WO1994022128A1/en?oq=WO9422128

**[36]** L. Ok-kyung, "Speaker generating a light corresponding to a sound source," KR20050062950A, 2003 Accessed: 2024. [Online]. Available: https://patents.google.com/patent/KR20050062950A/en?oq=KR20050062950

**[37]** K. Gil-ho, "Method for transforming sound to color and a light emitting speaker employing the sound to color transformation function," KR20080021201A, 2006 Accessed: 2024. [Online]. Available: https://patents.google.com/patent/KR20080021201A/en?oq=KR20080021201+(A)

**[38]** K. Gil-ho, "Apparatus for emiting light using led according to sound pitch, sound volume or tone color," KR20050034772A, 2003 Accessed: 2024. [Online]. Available: https://patents.google.com/patent/KR20050034772A/en?oq=KR20050034772+(A)

**[39]** D. H. Sliney, "What is light? The visible spectrum and beyond," Eye, vol. 30, pp. 222, 2016.

**[40]** Bruno A. Olshausen, "logs-and-music (Psych 129 - Sensory Processes)." Accessed: 2024. [Online]. Available: http://www.rctn.org/bruno/psc129/handouts/logs-and-music/logs-and-music.html

**[41]** F. Viénot, D. MacLeod, and J. D. Mollon, "CIE 170-2:2015 Fundamental Chromaticity Diagram with Physiological Axes – Part 2: Spectral Luminous Efficiency Functions and Chromaticity Diagrams," Color Res. Appl. vol. 41, pp. 216–216, 2016.

**[42]** D. Purves, G. J. Augustine, D. Fitzpatrick, and et al., Neuroscience - The Audible Spectrum. Sinauer Associates, 2001. Accessed: May 24, 2024. [Online]. Available: https://www.ncbi.nlm.nih.gov/books/NBK10924/

**[43]** T. J. Bruno and P. D. N. Svoronos, "CRC handbook of fundamental spectroscopic correlation charts," CRC Handb. Fundam. Spectrosc. Correl. Charts, pp. 1–226, 2005.

**[44]** Amplifion, "What is the range of human hearing? | Amplifon UK." Accessed: May 24, 2024. [Online]. Available: https://www.amplifon.com/uk/audiology-magazine/human-hearing-range

**[45]** International Commission on Illumination, "CIE cone-fundamental-based spectral tristimulus values for 2 degree field size | CIE." Accessed: 2024. [Online]. Available: https://cie.co.at/datatable/cie-cone-fundamental-based-spectral-tristimulus-values-2-degree-field-size

**[46]** Y. Ohno et al. "The Basis of Physical Photometry, 3rd Edition, CIE 018:2019," 2019.

**[47]** M. Anderson, R. Motta, S. Chandrasekar, and M. Stokes, "Proposal for a standard default color space for the Internet - sRGB," in Final Program and Proceedings - IS and T/SID Color Imaging Conference, 1996, pp. 238–246. Accessed: 2024. [Online]. Available: https://www.color.org/sRGB.xalter

**[48]** J. W. Cooley and J. W. Tukey, "An Algorithm for the Machine Calculation of Complex Fourier Series," Math. Comput. vol. 19, pp. 297, 1965.

**[49]** L. I. Bluestein, "A Linear Filtering Approach to the Computation of Discrete Fourier Transform," IEEE Trans. Audio Electroacoust. vol. 18, pp. 451–455, 1970.

IJBBE International Journal of Biophotonics & Biomedical Engineering Vol. 4, No. 2, Fall - Winter, 2024

Research Article

# Bio-Photonic Sensor Using Structurally Chiral Mediums as a Basal Cancer Cell Detection

N. Ghorani*, a, A.Madania, S. Roshan Entezarb

*a Department of Laser and Optical Engineering, University of Bonab, Bonab, Iran*
*b Department of Physics, Tabriz University, Tabriz, Iran*

*Corresponding author, Email: Nadia.ghorani@ubonab.ac.ir

DOI: 10.71498/ijbbe.2024.1192716

**ABSTRACT**

Received: Dec. 12, 2024, Revised: Feb. 11, 2025, Accepted: Feb. 23, 2025, Available Online: Mar. 18, 2025

*In this article, a high-accuracy novel optical biosensor consisting of a structurally chiral medium (SCM) with $4\bar{2}m$ point group symmetry and a silver metallic defect layer under the Sarid configuration as a theoretical and computational study has been investigated. We used incident light with p polarization and used the 4 × 4 transfer matrix method for absorption spectrum calculations. Surface plasmon polaritons (SPP) modes at the interface between a metallic layer and SCM have also been investigated. One of the advantages of using the SCM in this configuration is that it allows us to have several plasmonic and waveguide modes. We have also determined the difference between plasmonic modes and waveguide modes. This configuration creates an open assay interface for real-time detection of the interaction with extremely high sensitivity. The resonance angles observed in the absorption spectrum are very sensitive to changes in the fluid placed on top of the sensor and this sensor has a very high-quality factor that distinguishes it from other sensors. The effect of the tilt angle of the SCM has also been investigated. These combinations make the proposed designed sensor unique for performing label-free bioassays in the detection of cancer cells. The basis of this research is to detect cancer cells, which the designed sensor can detect with high sensitivity factors.*

**KEYWORD**

*Structurally chiral medium, Surface plasmon polariton, p polarized, Transfer matrix method, Plasmonic mode.*

## I. INTRODUCTION

In recent decades, structurally chiral materials (SCMs) have significant attention due to their unique properties and potential applications in various fields [1]. An SCM is characterized as a non-homogeneous and anisotropic material with a relative permittivity dyadic that varies helicoidally along a predetermined direction. Examples of SCMs include chiral elastomers, cholesteric liquid crystals, and sculptured thin films, which exhibit the circular Bragg phenomenon (CBP). The CBP leads to the near-total reflection of co-handed circularly

polarized plane waves at specific spectral regimes while allowing significant transmission of cross-handed waves [2_4].

The interaction between surface plasmons and photons at the interface of a metal and a dielectric material gives rise to surface quasiparticles termed surface plasmon polaritons (SPPs) [5]. In the coupling of photons and SPPs in practical configurations like the Kretschmann and Otto setups, the phenomenon of total internal reflection is employed [6]. When the interface of a metal and a periodically non-homogeneous dielectric material is considered, the propagation and excitation of SPP waves can be enhanced. SCMs serve as effective mediums for observing surface multi-plasmonic phenomena, leading to applications in multianalyte chemical sensors [7]. SPP waves often suffer from short propagation lengths due to metal damping losses. To address this limitation, the Sarid configuration has been proposed, where a metal thin film is positioned between two dielectric materials atop a high-index prism, forming a Three-layer composite capable of achieving propagation lengths on the order of micrometers via suitable structural parameters. SPP waves can be studied through two primary methods: the canonical boundary value problem, which is fundamentally theoretical, and the prism-coupled configuration, which combines both experimental and theoretical approaches. Research indicates that results obtained from both methods align closely [8,9].

Cancer of any organ manifests itself in the changes and malfunctions in the organ's function. Basal carcinoma is a common type of skin cancer that affects parts of the skin due to a lot of exposure to sunlight. Over time, UV rays can damage the DNA of skin cells, and Basal cells play a role in the process of creating new skin cells. When the DNA of these cells is damaged, the mutation increases the rate of reproduction, and cancer cells accumulate in that area [10,11].

Optical biosensors, for example, SCMs, photonic crystals, and surface plasmon resonance (SPR) have shown considerable versatility and application potential in recent years. SPR sensors detect changes in the refractive index of the medium above a metal surface following analyte interaction with surface-bound ligands, which in turn indicates plasmonic surface modes' behavior. Optical biosensors convert biological interactions, including those in blood samples, into measurable optical signals, providing single-step detection, repeatability, and ease of use, thus enabling rapid and precise measurements compared to traditional diagnostic methods. Among various types of biosensors such as electrical, piezoelectric, electrochemical, mechanical, magnetic, acoustic, and optical into an observable and evaluable format [12_14].

In this work, we have developed a biosensor based on a central metal defect within a dielectric structure configured as an SCM under the Sarid configuration. We analyze the optical absorption for p-polarized plane waves as a function of incident light angles in MATLAB software to extract multiple SPP peaks from the resulting absorption spectra that demonstrate a heightened sensitivity to variations in biological samples. The Absorption of linear polarized light in this context is computed using the 4×4 Transfer Matrix Method, laying the groundwork for advanced biosensing applications.

## II. METHOD

The schematic description of the proposed optical biosensor is shown in Fig. 1 in which the excitation of SPPs at the interface of an SCM and a thin metallic layer has been employed under the Sarid configuration. The structure is composed of a prism with the dielectric constant of $\varepsilon_1$, a thin layer of Silver with the thickness of $t_m$ and dielectric constant of $\varepsilon_m$, and a layer of SCM with the thickness of $t_{SCM}$ and dielectric constant of $\varepsilon_{SCM}$. The area above the second SCM is filled by the fluid biomaterial. It is assumed that this structure is irradiated by a light beam in the form of a plane wave with linear polarization from the prism at

an angle $\theta$ to the x-axis. In structurally chiral mediums, the tilt angle refers to the deviation or tilting of molecules from a reference axis (usually vertical or a specific optical axis in cholesteric liquid crystal such as SCM). This angle is crucial in chiral environments, as it influences the optical properties such as light polarization, optical rotation, and light scattering. The tilt angle determines how molecules are oriented within the structure, which impacts the material's chiral properties and the way it interacts with light, including phenomena like circular dichroism and birefringence. This angle plays a significant role in controlling the optical behavior of the medium.

The pitch refers to the distance over which the molecular or structural arrangement repeats itself in a helical or spiral pattern. It represents the length required for one full rotation of the molecular alignment around an axis. The pitch plays a key role in determining the optical properties of the material, such as the wavelength of light it reflects, its color, and its overall interaction with polarized light. Changes in the pitch can significantly affect the material's optical characteristics, including its ability to rotate light and the formation of specific optical textures [15_17].

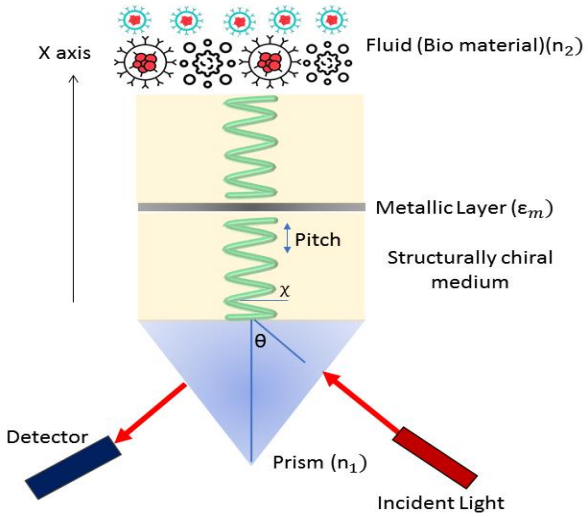


Fig. **1** The schematic description of the proposed optical biosensor.

The direction of rotation and heterogeneity of the studied structure is along the x-axis and the electromagnetic wave enters the structure at the angle $\theta$ [18].

We have used the matrix form of Maxwell's equations in a non-magnetic environment with 4 electric and magnetic field elements $\psi(x)=\left(e_y(x),e_z(x),h_y(x),h_z(x)\right)$ for the propagation of the wave [16]:

$$\frac{d\psi(x)}{dx}=ik_0A(x)\psi_0(x) \qquad (1)$$

In Eq. 1, $k_0$ is the wave number in the free space and $A(x)$ is $4\times4$ the matrix in the form of [15,18]:

$$A(x)=\begin{bmatrix} 0 & 0 & 0 & 1 \\ 0 & 0 & -1 & 0 \\ \frac{\varepsilon_{zx}(x)\varepsilon_{xy}(x)}{\varepsilon_{xx}(x)}-\varepsilon_{zy}(x) & \frac{\varepsilon_{zx}(x)\varepsilon_{xz}(x)}{\varepsilon_{xx}(x)}-\varepsilon_{zz}(x) & 0 & 0 \\ \varepsilon_{yy}(x)-\frac{\varepsilon_{yx}(x)\varepsilon_{xy}(x)}{\varepsilon_{xx}(x)} & \varepsilon_{yz}(x)-\frac{\varepsilon_{yx}(x)\varepsilon_{xz}(x)}{\varepsilon_{xx}(x)} & 0 & 0 \end{bmatrix}+$$
$$\begin{bmatrix} 0 & 0 & 0 & 1 \\ 0 & 0 & -1 & 0 \\ \frac{\varepsilon_{zx}(x)\varepsilon_{xy}(x)}{\varepsilon_{xx}(x)} & \frac{\varepsilon_{zx}(x)\varepsilon_{xz}(x)}{\varepsilon_{xx}(x)} & 0 & 0 \\ -\frac{\varepsilon_{yx}(x)\varepsilon_{xy}(x)}{\varepsilon_{xx}(x)} & -\frac{\varepsilon_{yx}(x)\varepsilon_{xz}(x)}{\varepsilon_{xx}(x)} & 0 & 0 \end{bmatrix} \qquad (2)$$

The dielectric tensor of an anisotropic structure in the principle coordinate system is shown in Eq. 3,

$$\varepsilon=\begin{pmatrix} \varepsilon_1 & 0 & 0 \\ 0 & \varepsilon_1 & 0 \\ 0 & 0 & \varepsilon_3 \end{pmatrix} \qquad (3)$$

where the axis 3 is the distinguished axis of the SCM. To calculate the SCM dielectric tensor elements, $\varepsilon_{i,j}(x)\,(i,j=x,y,z)$ in Eq. 2, we apply the tilt and rotation matrices of $T(\chi)$ and $R(x)$ to the dielectric tensor of Eq. 3 and obtain $\varepsilon_{SCM}(x)=R(x)T(\chi)\varepsilon T^{-1}(\chi)R^{-1}(x)$ where

$$T(\chi)=\begin{pmatrix}\cos\chi & 0 & \sin\chi\\ 0 & 1 & 0\\ -\sin\chi & 0 & \cos\chi\end{pmatrix}, \quad (4)$$

and

$$R(x)=\begin{pmatrix}1 & 0 & 0\\ 0 & \cos(qx) & -\sin(qx)\\ 1 & \sin(qx) & \cos(qx)\end{pmatrix}, \quad (5)$$

with $q=\frac{2\pi}{p}$.

The rotation matrix represents a spiral motion that is performed at a constant speed and also includes the pitch of the structure and displays structural chirality [19,20].

For the propagation of the wave inside the structure, the general solution of Eq. 1 can be written as follows:

$$\psi(L)=M\psi(0)=exp[\,ik_0\int_0^L A(x)\,dx\,]\psi(0). \quad (6)$$

M is a transfer matrix in Eq. 6 that connects the wave vector ψ from the left side of the layer to the right side. We used the same method to obtain the transfer matrix of the metal layer by substituting the dielectric tensor of the chiral medium with the dielectric permittivity of the metal, $\varepsilon_m$. Then, we used the method presented in reference [18] to obtain the mentioned transfer matrix M for the plane-wave illumination. We also used the boundary conditions to obtain the reflection and transmission coefficients of the structure as [20]:

$$\begin{bmatrix}t_s\\ t_p\\ r_s\\ r_p\end{bmatrix}=\begin{bmatrix}t_{ss} & t_{sp}\\ t_{ps} & t_{pp}\\ r_{ss} & r_{sp}\\ r_{ps} & r_{pp}\end{bmatrix}\begin{pmatrix}a_s\\ a_p\end{pmatrix}. \quad (7)$$

The coefficients of reflections and transmissions and the amplitudes of the incident plane waves have been indicated as $(r_s,r_p),(t_s,t_p)$ and $(a_s,a_p)$, respectively in Eq. 7. To obtain the optical absorption, we use the following relationship:

$$A_{i=s,p}=1-(\sum_{j=s,p}|r_{ij}|^2+|t_{ij}|^2) \quad (8)$$

The curves obtained by plotting the optical absorption as a function of the incident angle will represent some sharp peaks which are the positions of the incident angles in which the incident photon energy is transferred to the surface plasmon polaritons.

## III. RESULTS

we consider the prism-coupled method in the Sarid configuration shown schematically in Fig. 1. In the optical modeling, we consider two thin layers of SCM with the point group symmetry $\bar{4}2m$ and the dielectric constants $\varepsilon_1=2.7$ , $\varepsilon_3=3.2$, the tilt angle $\chi=45°$, and length $L=2P$ ( or $(L=4P)$ ) and the first layer of SMC is located on a prism, where $P=595\,nm$ the pitch of the structure. A thin layer of Silver with the thickness of $t_m=50nm$ and dielectric constant of the metallic layer $\varepsilon_m$ = -17.81+0.676i in the working wavelength (632.8 nm of He-Ne laser) is considered between the two SCM layers. First, we assume a normal and healthy biological sample named Basal cell covers the environment above the second SCM layer where the refractive index is $n=1.360$. Also, the dielectric coefficient of the prism is $n_1=1.515$ in the mentioned wavelength.

The results depicted in Fig. 2 highlight the optical absorption characteristics of the structure as a function of the incident angle for two different thicknesses of the SCM layer, denoted (L=2P) and (L=4P). The Results were conducted using p-polarized light to evaluate the performance of normal Basal cells. The absorption spectra reveal several peaks that vary depending on the incident angle and in angles of 65.8°, 68.7° and 86.2°. Notably, one particular peak, marked with an arrow, shows minimal shift—almost negligible—in the excitation angle with an increase in the SCM layer thickness (L). This behavior suggests that this specific peak in 86.2° is associated with the excitation of Surface Plasmon Polaritons (SPPs), which are sensitive to the layer's

thickness but not significantly affected in this instance. In contrast, other identified absorption peaks exhibit a more pronounced shift in the excitation angle as (L) increases. These peaks are indicative of waveguide modes in angles of 65.8° and 68.7°, which respond differently to the thickness of the SCM layer compared to SPPs. Furthermore, when the optical absorption was assessed using s-polarized light, the results showed in Fig. 2 that the absorption levels in the system were negligible across all incident angles, leading to the disappearance of the absorption peaks. This finding implies that the structure is unsuitable for biosensing applications when operating under s-polarized light conditions. As a result, this analysis establishes that a p-polarized wave is essential for effectively utilizing this structure as a biosensor, which will be the focus of the subsequent sections of the paper.

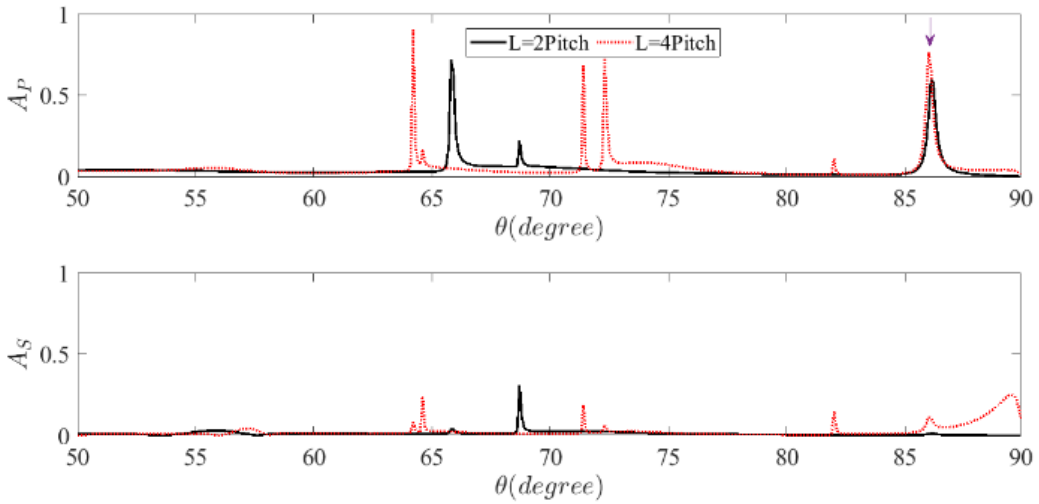


Fig. **2** The optical absorption of the structure as a function of the incident angle for two thicknesses of the SCM layer, $L = 2P$ and $L = 4P$ . the results for the cases of normal Basal cells, using p-polarized waves. And the same results for the case of s-polarized waves.

To illustrate the surface plasmon polariton (SPP) modes, we have presented the electric field profiles of SPP mode within the structure, as depicted in Fig. 3. Specifically, showcase the field profiles for SPP mode at a certain incidence angle related to the case of the Basal cell. Both SPP and waveguide modes demonstrate a propagative behavior within the SCM layer, exhibiting evident localization of the electric field at the interface between the SCM and the biological sample. This phenomenon indicates a significant penetration of the evanescent wave into the sample, which is critical for sensing applications. Also, for the SPP modes, the electric field is significantly localized at the interface between the metal layer and the SCM layer. This distinct localization at different interfaces ultimately highlights the unique propagation characteristics of SPPs and waveguide modes, emphasizing their relevance in applications such as biosensing and optical devices.

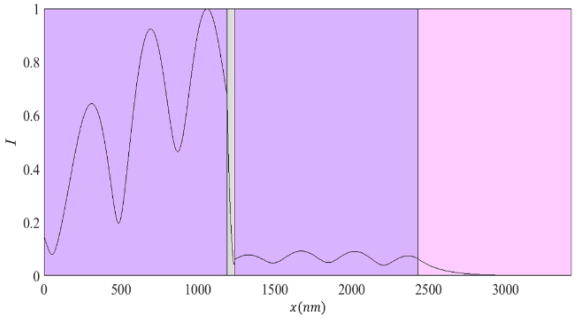


Fig. **3** The field profiles of the SPP mode correspond to the incidence angle of 86.2°.

Figure 4 shows the graph of optical absorption as a function of the incident light angle for

different thicknesses of the metal layer. According to this figure, when we consider the thickness of the metal layer to be zero, no absorption peak has been seen, and this indicates that SPPs can be excited in the vicinity of a metal and a dielectric. There is no absorption peak in the 85 nm thickness of the metal layer and it can be argued that if the thickness of the metal layer is greater than the penetration depth of the metal before the incident light reaches the interface between the metal and the SCM layer, it is absorbed or reflected and cannot transfer its energy to the SPPs and cause their excitation. On the other hand, if the thickness of the metal layer is less than its penetration depth, a greater percentage of incident light passes through the metal medium and does not have enough time to couple with surface plasmons. Therefore, thicknesses close to the penetration depth of the metal also have significant absorption. According to Figure 4, it can be seen that the peaks in the absorption spectrum are excited for the 50 nm thickness of the metal layer. It can be said that the presence of the metal layer is responsible for the formation of absorption peaks, each of which shows plasmonic or waveguide modes.

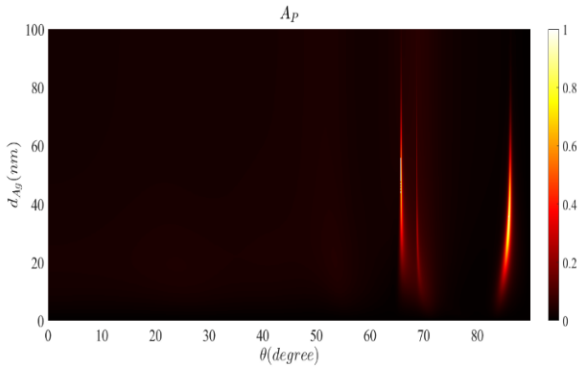


Fig.**4** Optical absorption diagram for different thicknesses of the metal layer.

In this part, by examining the effect of different tilt angles of the SCM layer, we have examined the optical absorption diagram according to the angle for the designed structure. By applying different tilt angles, it can be seen that the peaks in the optical absorption graph are shifted to higher angles and the spp are excited at higher angles. The closer the tilt angle is to the vertical line, the SCM layer becomes similar to an isotropic medium, in other words, this layer has larger optical constants and the number of modes will be less. And this matter can be understood that a plasmonic and waveguide mode will appear at the junction of the metal layer and an isotropic dielectric. However, the presence of the SCM layer of specified parameters allows us to obtain several modes. The number of these modes varies by changing the specifications of the SCM and the metal layer. In summary, this proposed structure can be used as an optical sensor with the ability to create more than one mode to measure multiple analytes simultaneously in fluid matter.

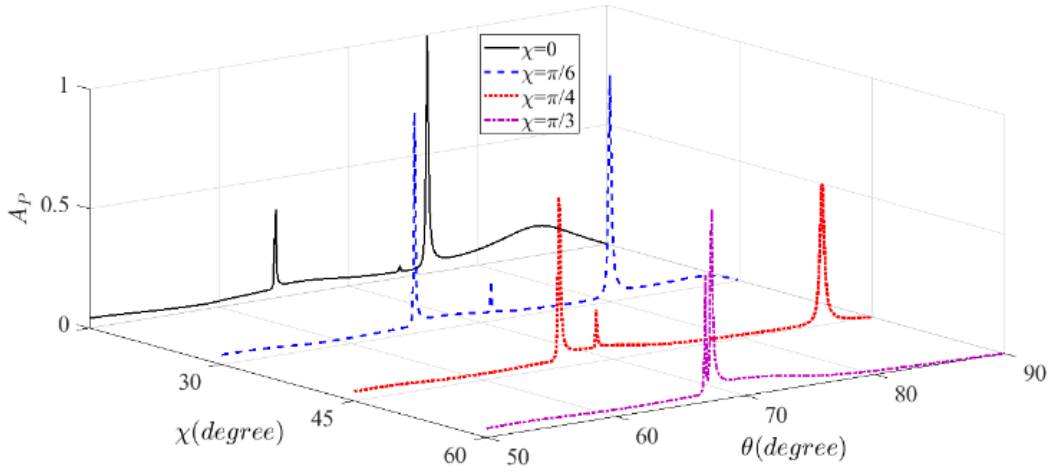


Fig.**5** Optical absorption diagram for different tilt angles of SCM layer.

Fig.**5** illustrates the effect of the tilt angle (χ) of the SCM layer on the optical absorption spectrum. As the tilt angle increases, the resonance peaks shift toward higher incident angles, indicating that the coupling conditions for plasmonic and waveguide modes are altered. At smaller tilt angles, the structure behaves more like an anisotropic medium, supporting multiple guided modes. However, at larger tilt angles, the system approaches an isotropic limit, leading to fewer observable resonance peaks. This effect demonstrates that adjusting the tilt angle allows for fine-tuning of the sensor's response, optimizing sensitivity for specific refractive index variations in the biological medium.

The sensitivity (S) of the designed biosensor can be expressed as the ratio of the change in resonance angle to the change in refractive index [12], for example,

$$\boldsymbol{S = \frac{\Delta\theta}{\Delta n}} \quad (9)$$

The figure of merit (FOM) determines the accuracy and correctness of the data obtained from the sensor

and is calculated according to the following relationship [12]:

$$\boldsymbol{FOM = \frac{S}{FWHM}} \quad (10)$$

The peak in the absorption diagram for two healthy and defective samples has been reported according to Table No. 1. This table reports the performance of the designed sensor by changing the tilt angle of the SCM layer. By examining different tilt angles, which causes changes in the light angle and, as a result, changes in the sensing parameters.

Based on Table 1, When the defective cell is replaced by the healthy cell, the changes in the refractive index bring with it changes in the absorption modes, such as the position in terms of angle, and also the reduction of the width of these modes. As the tilt angle increases, we see a gradual decrease and then an increase in FWHM. As a result, the quality factor of the sensor has a significant figure. The sensitivity of the sensor is the lowest at zero and 60° tilt angle, but with the change of the refractive index, it can detect the smallest changes of the refractive index at the tilt angles of 30° and 45°. As we expected, with the change in the refractive index of the biological material, the angle shifted, which is reported in Figure 6. One of the advantages of the presence of the SCM layer in such a sensor is that it reduces FWHM and shows the high quality of the sensor. This sensor can be used to detect the progress of diseases, which is done by comparing healthy and defective cells. By measuring the resonance angle for an unknown sample and the obtained value, it is impossible to predict the progress of

the disease, and the closer the angle changes to zero, the less progress we will have in that disease.

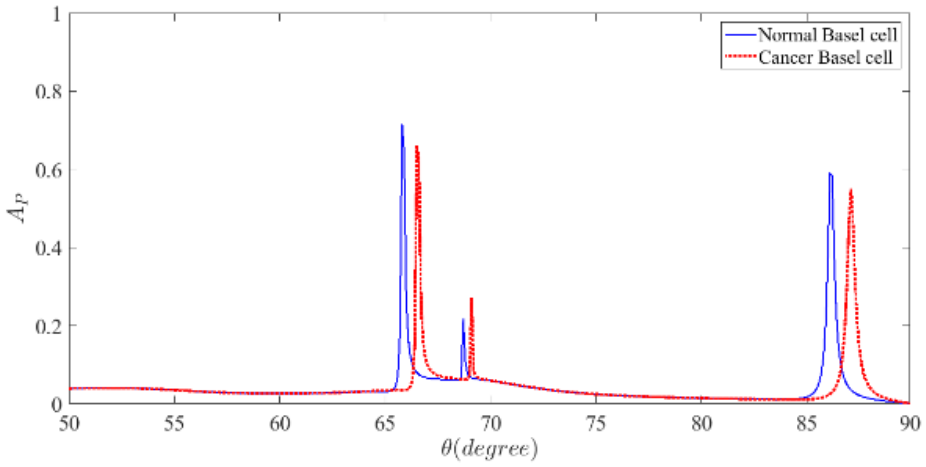


Fig.**6** The absorption spectrum of the designed biosensor for healthy and cancerous samples of Basal cells.

In this section, a comparative analysis of the sensitivity and FOM of biosensors designed in recent years related to cancer is presented in Table 2. Therefore, the proposed SCM sensor can offer better performance potential due to its higher FOM compared to other sensors. By placing layers of dielectric materials, the performance of this sensor can be increased.

TABLE**1**. SENSOR PARAMETERS FOR DIFFERENT TILT ANGLE

| *Cell* | | *Sensor Parameters* | $\chi = 0°$ | $\chi = 30°$ | $\chi = 45°$ | $\chi = 60°$ |
|---|---|---|---|---|---|---|
| *Basal* | | $\Delta\theta$ *(degree)* | *0.63* | *1.15* | *1.22* | *0.6* |
| *Normal cell* | *Cancer Cell* | *FWHM (degree)* | *0.2* | *0.1* | *0.2* | *0.15* |
| *1.36* | *1.38* | $S\ (\frac{degree°}{RIU})$ | *31.5* | *57.5* | *61* | *30* |
| | | *FOM* $(\frac{1}{RIU})$ | *157.5* | *575* | *305* | *200* |

TABLE**2**. COMPARISON OF THE SCM BIOSENSOR AND PREVIOUSLY REPORTED BIOSENSORS FOR CANCER DETECTION.

| *Ref.* | *Structure* | *Sensitivity* | *FOM* $(\frac{1}{RIU})$ |
|---|---|---|---|
| *[21]* | *two-dimensional photonic crystal (PC)* | *15085(nm/RIU)* | *159.54* |
| *[22]* | *N-FK51A/Ag/AION/BlueP* | *416.85(degree/RIU)* | *155.94* |
| *[23]* | *BK7/Ag/CNT/Pt/Fe2O3* | *330.571(degree/RIU)* | *29.91* |
| *[24]* | *BK7/TiO2/Au/graphene* | *292.86(degree/RIU)* | *48.02* |
| *[25]* | *Ag/TiSi2/BP* | *218.6(degree/RIU)* | *45.26* |
| *Our Work* | *Prism/SCM/Al/SCM* | *61(degree/RIU)* | *575* |

## IV. Conclusion

The propagation of multiple SPP waves in SCMs with a central metal defect was studied theoretically in Sarid configuration by using the transfer matrix method-based biosensor structure. The multiple SPP modes were extracted from optical absorption spectra for different structural parameters. The results showed that some branches of SPP waves had discontinuities due to their conversion to other absorption peaks such as waveguide modes or combined into other SPP modes. The key feature of this sensor is the existence of a plasmonic waveguide mode, which makes the sensor structure very sensitive to changes in the refractive index of the sensor's upper environment. The results of the optical absorption graphs as a function of the incident light angle with p polarization at the wavelength of 632.8 nm showed that more than one surface mode is emitted in the common phase.

Plasmonic modes are selected from waveguide modes by changing the thickness of the SCM layer. As the tilt angle increases, the peaks shift to higher incident light angles. The results of this work are used in biosensors and investigation of various chemical species and biomolecules that are absorbed on the surface of the SCM layer. By checking the sensor parameters for Basal cancer samples, it was checked by this sensor. The results have shown that this sensor has a high FOM quality factor with the effect of different tilt angles of the SCM environment.

## References


**[1]** S. E. Swiontek, D. P. Pulsifer, and A. Lakhtakia, "Optical sensing of analytes in aqueous solutions with a multiple surface-plasmon-polariton-wave platform," Scientific Reports, vol. 3, no. 1, Mar. 2013.

**[2]** A. Lakhtakia, M. W. McCall, J. A. Sherwin, Q. H. Wu, and I. J. Hodgkinson, "Sculptured-thin-film spectral holes for optical sensing of fluids," Optics Communications, vol. 194, no. 1–3, pp. 33–46, Jul. 2001.

**[3]** P. D. McAtee and A. Lakhtakia, "Theory of artificial-neural-network-based simultaneous optical sensing of two analytes using sculptured thin films," Journal of Nanophotonics, vol. 15, no. 03, Sep. 2021.

**[4]** S. Swiontek, D. Pulsifer, and A. Lakhtakia, "Optical sensing of analytes via surface multiplasmonics," SPIE Newsroom, Jul. 2013.

**[5]** R. B. M. Schasfoort, "History and Physics of Surface Plasmon Resonance," Handbook of Surface Plasmon Resonance, pp. 27–59, May 2017.

**[6]** S. Pal, N. Pal, Y. K. Prajapati, and J. P. Saini, "Performance Evaluation of SPR Biosensor using Metamaterial over Conventional SPR and Graphene based SPR Biosensor," 2018 5th International Conference on Signal Processing and Integrated Networks (SPIN), Feb. 2018.

**[7]** S. Swami, F. Kayenat, and S. Wajid, "SPR biosensing: Cancer diagnosis and biomarkers quantification," Microchemical Journal, vol. 197, p. 109792, Feb. 2024.

**[8]** F. Babaei and S. A. Seyyedi, "Excitation of Surface Plasmon-Polariton Wave at Both Interfaces of a Silver Thin Film in Two-Layer Kretschmann Geometry," Plasmonics, vol. 16, no. 6, pp. 2139–2146, Jun. 2021.

**[9]** S. H. Hosseininezhad and F. Babaei, "Excitation of Multiple Surface Plasmon-Polaritons by a Metal Layer Inserted in an Equichiral Sculptured Thin Film," Plasmonics, vol. 13, no. 6, pp. 1867–1879, Feb. 2018.

**[10]** M. R. Hasan et al., "Recent development in electrochemical biosensors for cancer biomarkers detection," Biosensors and Bioelectronics: X, vol. 8, p. 100075, Sep. 2021.

**[11]** L. Fania et al., "Basal Cell Carcinoma: From Pathophysiology to Novel Therapeutic Approaches," Biomedicines, vol. 8, no. 11, p. 449, Oct. 2020.

**[12]** N. Ghorani, A. Madani, and S. R. Entezar, "Real-time biosensor application of structurally chiral medium for detection and sensing of plasma in human blood," Physica Scripta, vol. 98, no. 5, p. 055518, Apr. 2023.

**[13]** F. Bayat, S. Ahmadi-Kandjani, and H. Tajalli, "Designing Real-Time Biosensors and Chemical Sensors Based on Defective 1-D Photonic Crystals," IEEE Photonics

Technology Letters, vol. 28, no. 17, pp. 1843–1846, Sep. 2016.

**[14]** H. Pashaei Adl, F. Bayat, N. Ghorani, S. Ahmadi-Kandjani, and H. Tajalli, "A Defective 1-D Photonic Crystal-Based Chemical Sensor in Total Internal Reflection Geometry," IEEE Sensors Journal, vol. 17, no. 13, pp. 4046–4051, Jul. 2017.

**[15]** M. Franco-Ortiz, A. Corella-Madueño, R. A. Rosas-Burgos, J. A. Reyes, and C. G. Avendaño, "Electrically tuned optical reflection band for an artificial helicoidal structure," Journal of Modern Optics, vol. 65, no. 17, pp. 1994–2005, Jun. 2018.

**[16]** C. G. Avendaño and D. Martínez, "Tunable omni-directional mirror based on one-dimensional photonic structure using twisted nematic liquid crystal: the anchoring effects," Applied Optics, vol. 53, no. 21, pp. 4683, Jul. 2014.

**[17]** J. A. Reyes and A. Lakhtakia, "Electrically controlled optical bandgap in a structurally chiral material," Optics Communications, vol. 259, no. 1, pp. 164–173, Mar. 2006.

**[18]** C. G. Avendaño, I. Molina, and J. A. Reyes, "Anchoring effects on the electrically controlled optical band gap in twisted photonic liquid crystals," Liquid Crystals, vol. 40, no. 2, pp. 172–184, Oct. 2012.

**[19]** I. Abdulhalim, "Analytic propagation matrix method for anisotropic magneto-optic layered media," Journal of Optics A: Pure and Applied Optics, vol. 2, no. 6, pp. 557–564, Oct. 2000.

**[20]** M. Faryad and A. Lakhtakia, "The circular Bragg phenomenon," Advances in Optics and Photonics, vol. 6, no. 2, p. 225, Jun. 2014.

**[21]** H. Miyan, R. Agrahari, S. K. Gowre, M. Mahto, and P. K. Jain, "Computational Study of a Compact and High Sensitive Photonic Crystal for Cancer Cells Detection," IEEE Sensors Journal, vol. 22, no. 4, pp. 3298–3305, Feb. 2022.

**[22]** S. A. Rafi et al., "Optical Based Surface Plasmon Resonance Sensor for the Detection of the Various Kind of Cancerous Cell," Cell Biochemistry and Biophysics, pp.1-27, Sep. 2024.

**[23]** P. Nagarajan, S. Manoharadas, V. Dhasarathan, and S. Rajeshkannan, "Cancer Detection Using Multi-layered Kretschmann Configuration–based Refractive Index Sensor," Plasmonics, pp.1-12, Jun. 2024.

**[24]** S. Mostufa, T. B. A. Akib, Md. M. Rana, and Md. R. Islam, "Highly Sensitive TiO2/Au/Graphene Layer-Based Surface Plasmon Resonance Biosensor for Cancer Detection," Biosensors, vol. 12, no. 8, pp. 603, Aug. 2022.

**[25]** B. Karki, A. Uniyal, A. Pal, and V. Srivast, "Advances in surface plasmon resonance–based biosensor technologies for Cancer Cell detection," International Journal of Optics, no. 1, pp. 1476254, Mar. 2022.

IJBBE International Journal of Biophotonics & Biomedical Engineering Vol. 4, No. 2, Fall - Winter, 2024

Research Article

# Study on the Photocatalytic Activity of Graphene Oxide in Removal of Xylene Solution

**P. Gharbani[1,2,*] and A. Mehrizad[2,3]**

*1Department of Chemistry, Ahar Branch, Islamic Azad University, Ahar, Iran*
*2 Industrial Nanotechnology Research Center, Tabriz Branch, Islamic Azad University, Tabriz, Iran*
*3Department of Chemistry, Tabriz Branch, Islamic Azad University, Tabriz, Iran*

***Corresponding author, Email: parvingharbani@yahoo.com**
**parvin.gharbani@iau.ac.ir**

**DOI: 10.71498/ijbbe.2024.1196386**

**ABSTRACT**

Received: Jan. 13, 2025, Revised: Feb. 4, 2025, Accepted: Feb. 18, 2025, Available Online: Mar. 18, 2025

*Exposure to xylene can occur through inhalation, ingestion, or contact with the eyes or skin, and can have adverse effects on human health. In this study, graphene oxide was utilized for the photocatalytic removal of xylene from aqueous solutions. The impact of various factors, such as irradiation time, initial pH, and adsorbent dosage, on the removal of xylene was investigated. The findings indicated that the equilibrium of the photocatalytic removal process was reached in 50 minutes, and then decreased. Additionally, the maximum removal of xylene was observed at a pH of 6. It was found that increasing Graphene oxide dosage is due to a decrease in Xylene removal. Notably, the results showed that 0.01g of graphene oxide could eliminate 78.87% of xylene at an initial concentration of 500 mg/L and a pH of 6 under UV irradiation.*

**KEYWORDS**

*Xylene; Photocatalyst; Graphene oxide; UV irradiation*

## I. INTRODUCTION

The advancement of civilization and the industrialization of societies leads to water pollution, which is considered a serious threat to living organisms. The oil, gas, and petrochemical industries play a crucial role in serving humanity today. Given the vast scale and high volume of the oil industry, wastewater from these industries poses one of the most significant global challenges, particularly in oil-rich countries like Iran. Xylene (Fig. 1), a dangerous and persistent aromatic hydrocarbon commonly found in the effluents of chemical and refinery industries, has a high potential to contaminate surface and groundwater. It can seep into the environment through leaking storage tanks and petroleum products, such as gasoline and diesel fuel, posing harm to humans, animals, and others. Xylene is suspected to cause central nervous system disorders and is classified as a Group E carcinogen. As a result, the maximum allowable level of xylene contamination in

drinking water has been set at around 10,000µg/L. Due to its detrimental health effects; xylene is considered a high-risk compound for living organisms' health. Therefore, the removal of xylene from surface and underground water sources is essential.

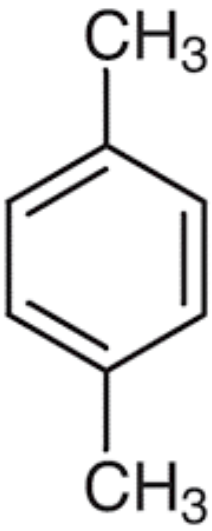


Fig. 1. The structure of Xylene.

Numerous physical methods (such as filtration, adsorption, coagulation, and sedimentation) and chemical techniques (such as biological methods and advanced oxidation processes) have been utilized to eliminate pollutants [9]. Advanced oxidation processes entail the use of chemical agents like hydrogen peroxide, ozone, transition metals, and metal oxides. Moreover, an energy source such as ultraviolet or visible light radiation, electric current, gamma rays, and ultrasonics is necessary. These processes are founded on the generation of free radicals, particularly hydroxyl radicals, which transform pollutants into biologically degradable and less harmful compounds [10,11]. Frequently, advanced oxidation processes incorporate ozone coupled with hydrogen peroxide and ultraviolet (UV) radiation [12,13]. Graphene is a two-dimensional carbon allotrope, with graphene oxide serving as its principal derivative. The graphene oxide comprises oxygenated functional groups like hydroxyl, epoxy, carbonyl, and carboxyl on sp3 carbon atoms, visible on layered graphene sheets, exhibiting properties distinct from those of pristine graphene [14,15]. One intriguing characteristic of photocatalytic materials is their photoluminescence capability. With graphene oxide, instead of the usual fluorescence deriving from band edge transitions, there exists the possibility of local exciton recombination in electronic states displaying different configurations[16]. This distinct attribute facilitates rapid electron transfer, diminished recombination, and improved light scattering, ultimately enhancing the catalyst's efficiency[17]. It is crucial to acknowledge that graphene oxide operates as a P-type semiconductor[18]. Consequently, when exposed to irradiation, holes gravitate towards the graphene oxide layer, while electrons are propelled towards the surface, generating a cathodic photocurrent[19]. These electrons are subsequently seized by water particles adhered to the electrode surface, leading to the generation of hydrogen post-reaction[20]. The outcomes observed under ultraviolet light are closely tied to the conduct of oxygen groups and their fluctuations in content. Particularly, the optical band gap of graphene oxide is approximately 3.06 electron volts[21]. In this study, we aim to explore the photocatalytic degradation of xylene under UV light using graphene oxide. Additionally, we seek to evaluate the impact of pH, adsorbent dosage, xylene concentration, and contact time on the process.

## II. PHOTOCATALYTIC EXPERIMENTS

All experiments were conducted inside a box housing a 300 W halogen lamp serving as a UV light source within a crystallizer placed on a magnetic stirrer. The xylene solution, prepared with the desired concentrations, underwent adsorption measurement using a UV-Vis spectrophotometer. Graphene oxide was introduced into the solution and stirred, followed by a series of photocatalytic processes where samples were extracted every 5 minutes. Subsequently, the samples were filtered, and their absorbance at 282 nm was analyzed using a UV-Vis spectrophotometer (UV mini-1240 Shimadzu). The study investigated the impact of pH parameters, irradiation time, graphene oxide dosage, and xylene concentration. The percentage of xylene removal was then calculated using the equation [20].

$$\%\text{Removal}=\frac{C0-Ct}{C0}*100 \quad (1)$$

Here, C0 and Ct are the Xylene concentrations before and after photocatalytic removal, respectively.

## III. RESULTS AND DISCUSSION

The photocatalytic process depends on key parameters including irradiation time, the amount of photocatalyst, and the pH of the solution.

### A. *Effect of irradiation time*

To study the effect of irradiation time, a solution of 500 mg/L of xylene was prepared and 0.01 g of graphene oxide was added to it. The solution was then stirred for 50 minutes using a magnetic stirrer under UV irradiation. Sampling was conducted at various time intervals to assess xylene removal, with results displayed in Fig. 1. The data indicates that an increase in irradiation time up to 30 minutes resulted in enhanced xylene removal, after which the removal rate plateaued. This is attributed to the increased interaction between xylene and graphene oxide with longer irradiation time, leading to improved xylene removal efficiency. As a result, all subsequent experiments were performed at a constant time of 30 minutes.

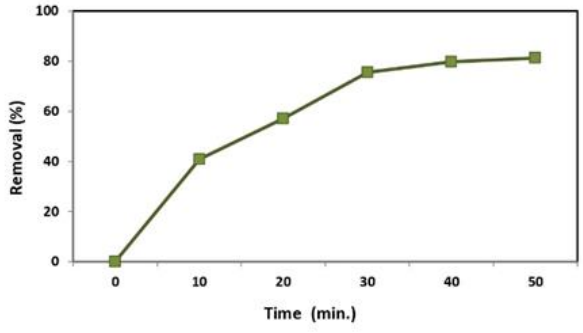


Fig 1. The effect of irradiation time

pH=6.8, [GO]0=0.01 g/100mL

### B. *Dosage of Graphene Oxide*

To investigate the impact of graphene oxide dosage on the photocatalytic removal of xylene, varying amounts of graphene oxide were examined. Fig. 2 illustrates that as the dosage of graphene oxide is increased from 0.01 to 0.05 g/100mL, the percentage of xylene removal decreases. This decline can be attributed to the reduction in light penetration as the concentration of particles becomes too high, leading to aggregation and a decrease in available surface area for light absorption, thereby hindering photocatalytic degradation [22]. Furthermore, an increase in the photocatalyst concentration results in heightened turbidity of the solution and non-uniform distribution of light intensity, consequently leading to a decrease in removal percentage with increasing photocatalyst concentration.

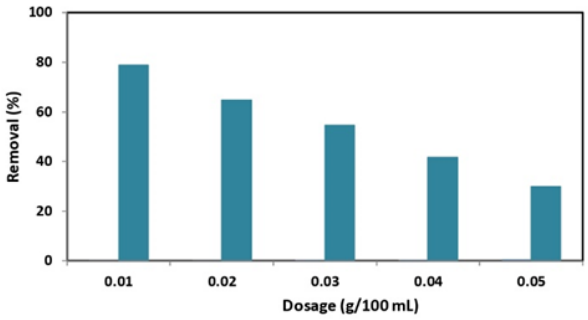


Fig. 2. Dosage of graphene oxide

Irridiation time= 50 min.; pH=6.8

### C. *Effect of pH*

The pH of a solution is a critical factor in the photocatalytic process as it greatly influences the adsorption of pollutants on the photocatalyst's surface [23]. As shown in Fig. 3, xylene degradation is maximized at pH 6. The zeta potential of graphene oxide is approximately 6.2. Notably, graphene oxide exhibits a positive surface charge at pH below 6.2, a negative surface charge at pH above 6.2, and no surface charge at pH 6.2. At a pH of 6.2, both graphene oxide and xylene are uncharged, leading to optimal xylene removal.

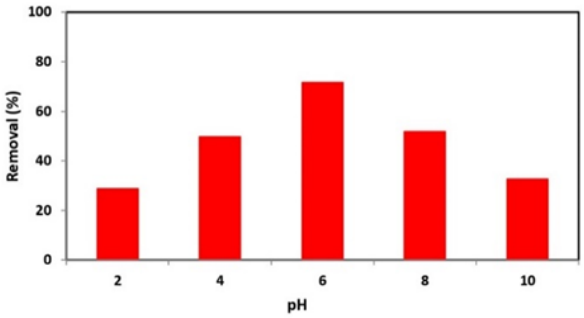


Fig 3. Effect of pH

Irridiation time= 50 min.; [GO]0=0.01 g/100mL

## IV. CONCLUSION

In this research, the xylene compound as a hazardous material was removed from aqueous solutions using graphene oxide photocatalytic under UV light. The effect of some key parameters affecting photocatalytic degradation such as irradiation time, pH, and photocatalyst dosage on xylene removal was studied. The results confirmed that xylene removal decreases with increasing adsorbent dosages and increases with increasing irradiation time. Maximum removal of xylene was also observed at a pH of about 6.

## REFERENCES

**[1]** X. Chen, W. Zhu, S. Feng, and J. Chen, "Photodegradation of xylene isomers: Kinetics, mechanism, secondary pollutant formation potential, and health risk evaluation. Journal of Environmental Sciences, Vol.136, pp.658-669.

**[2]** B. Bina, M.M. Amin, A. Rashidi, and H. Pourzamani, "Water and wastewater treatment from BTEX by carbon nanotubes and Nano-Fe," Water resources, Vol. 41, pp. 719-727, 2014.

**[3]** K.T. Chuang, S Cheng, and S. Tong, "Removal and destruction of benzene, toluene, and xylene from wastewater by air stripping and catalytic oxidation," Industrial & engineering chemistry research, Vol.31, pp.2466-2472, 1992.

**[4]** S.H. Kim, J.H. Park, J. H. and C.Y. Lee, "Surface-functionalized mesoporous silica nanoparticles as sorbents for BTEX," Journal of Porous Materials, Vol.20, pp. 1087-1093, 2013.

**[5]** R. Hosseinzadeh, R. Tahmasebi, K. Farhadi, A.A. Moosavi-Movahedi, A. Jouyban, and J. Badraghi, J. "Novel cationic surfactant ion pair-based solid-phase microextraction fiber for nano-level analysis of BTEX," Colloids and Surfaces B: Biointerfaces, Vol.84, pp. 13-17, 2011.

**[6]** H. Shim, E. Shin, and S.T. Yang. "A continuous fibrous-bed bioreactor for BTEX biodegradation by a co-culture of Pseudomonas putida and Pseudomonas fluorescens," Advances in Environmental Research, Vol. 7, pp. 203-216, 2002.

**[7]** A.K. Mathur, C.B. Majumder, S. Chatterjee, "Combined removal of BTEX in air stream by using a mixture of sugar cane bagasse, compost, and GAC as biofilter media," Journal of Hazardous Materials, Vol.148, pp.64-74, 2024.

**[8]** J. M. M.de Mello, H. de Lima Brandão, A. A. U. de Souza, and S. M. D. A. G. Ulson, "Biodegradation of BTEX compounds in a biofilm reactor—modeling and simulation," Journal of Petroleum Science and Engineering, Vol.70, pp. 131-139, 2010.

**[9]** Y. ayawardhana, S.R. Gunatilake, Mahatantila, K. M.P. Ginige, and M. Vithanage, "Sorptive Removal of Toluene and M-Xylene by Municipal Solid Waste Biochar: Simultaneous Municipal Solid Waste Management and Remediation of Volatile Organic Compounds," Journal of Environmental Management, Vol. 238, pp.323–330, 2019.

**[10]** Z. Cheng, J. Wang, D. Chen, J. Yu, S. Zhang, S. Wang, and Y. Dai, "Insights into Efficient Removal of Gaseous p-Xylene Using Cerium-Doped ZnO Nanoparticles through Photocatalytic Ox+idation," Catalysis Science & Technology, Vol.11, pp. 612–623, 2021.

**[11]** Z.L. Ye, Q.Y. Han, Y.F. Jiang, S.D. Zhang, L. Shu, and RX. Zhang, "Synergetic Effect Between Plasma and UV for Toluene Conversion in Integrated Combined Plasma Photolysis Reactor with KrCl/KrBr/XeCl/Xe2 Excilamp," Canadian Journal of Chemical Engineering, Vol. 93, pp. 1168–1175, 2015.

**[12]** H.M. Lin, S.J. Tzeng, P.J. Hsiau, and W.L. Tsai, "Electrode effects on gas sensing properties of nano crystalline zinc oxide," Nanostructured Materials, Vol. 10, pp.465-477, 1998.

**[13]** M.S. Tokumoto and C.V. Santilli, "Preparation of ZnO nano partides and colon structural study of the molecular precursor," Journal of Sol-Gel

Science and Technology, Vol. 2003, pp.547-551, 2017.

**[14]** A. Adán-Más and D. Wei, "Photoelectrochemical Properties of Graphene and Its Derivatives," Nanomaterials, Review, Vol. 3, pp.325-356, 2013.

**[15]** A. Esmaeili and M.H. Entezari, "Facile and fast synthesis of graphene oxide nanosheets via bath ultrasonic Irradiation," Journal of Colloid and Interface Scienc, Vol. 432, pp. 19-25,2014.

**[16]** H. Khan, "Graphene-based semiconductor oxide photocatalysts for photocatalytic hydrogen (H2) production, a review," International Journal of Hydrogen Energy. Vol.84, pp. 356-371, 2024.

**[17]** E. Fathi, F. Derakhshanfard, P. Gharbani and Z. Ghazi Tabatabaei, "Facile synthesis of MgO/C3N4 nanocomposite for removal of reactive orange 16 under visible light," Journal of Inorganic and Organometallic Polymers and Materials, Vol 30, pp.2234-2240, 2020.

**[18]** T. A. P. Mendonça, A. S. Giroto, J. T. Chambi, S. L. Cuffini, N. C. S. Vieira, and M. Gonçalves, "Efficient photocatalyst based on activated carbon/graphene oxide/TiO2 synthesized under acidic conditions for environmental remediation," Journal of Photochemistry and Photobiology A: Chemistry,Vol. 462, pp.116244, 2025.

**[19]** M. Bashiri and M. A. Hosseini-Sarvari, "comprehensive investigation into the synthesis, characterization, and photocatalytic performance of modified graphene oxide via imino bond with ferrocene as a novel photocatalyst for thioamide synthesis," Catalysis Science & Technology, Vol.14, pp.4655-4673, 2024.

**[20]** M. Urmimala, K. S. Subrahmanyam, K. Gopalakrishnan, N. Kumar, R. Kumar and A. Govindaraj, "Potential of nanocarbons and related substances as adsorbents and chemical storage materials for $H_2$, $CO_2$ and other gases," Indian Journal of Chemistry, Section A: Inorganic, Physical, Theoretical and Analytical Chemistry, Vol. 51, pp. 15-31, 2012.

**[21]** F. Xiaofeng, W.T. Zheng, and J. L. Kuo, "Adsorption and Diffusion of Li on Pristine and Defective Graphene," American Chemical Society, Vol 50, pp. 345-765. 2012.

**[22]** M.R. Sohrabi, M. Moghri, H.R. Fard Masoumi, S. Amiri and N. Moosavi, "Optimization of Reactive Blue 21 removal by Nanoscale Zero-Valent Iron using response surface methodology," Arabian journal of chemistry, Vol. 9.4, pp. 518-525, 2016.

**[23]** B.H. Fard, R.R. Khojasteh, and P. Gharbani, "Preparation and characterization of visible-light sensitive nano Ag/Ag 3 VO 4/AgVO 3 modified by graphene oxide for photodegradation of reactive orange 16 dye," Journal of Inorganic and Organometallic Polymers and Materials, Vol.28, pp.1149-1157. 2018.

**THIS PAGE IS INTENTIONALLY LEFT BLANK.**